Electronic Structures of Metallic Transition Metal Dichalcogenides Studied by Angle-Resolved Photoemission Spectroscopy



Yiwei Li

Jesus College

University of Oxford

A thesis submitted for the degree of

Doctor of Philosophy

Trinity 2019

Electronic Structures of Metallic Transition Metal Dichalcogenides Studied by Angle-Resolved Photoemission Spectroscopy

Yiwei Li, Jesus College, Oxford

Thesis submitted in fulfilment of the requirements for the degree of Doctor of Philosophy at the University of Oxford. Trinity, 2019

Abstract:

In this thesis, we describe the study on the electronic structures of three selected metallic transition metal dichalcogenides (TMDs) using angle-resolved photoemission spectroscopy (ARPES) as follow:

1. *2H-$TaSe_2$* is a quasi-two-dimensional TMD hosting a 3×3 commensurate charge-density-wave (CDW) at low temperature. Using high-resolution ARPES, we have mapped out the reconstructed electronic structure in the CDW phase. The observation of the fine structure near Brillouin zone (BZ) centre supplements the picture of Fermi surface folding. In addition to the anisotropic CDW band gaps that energetically stabilize the system at the Fermi level in the first-order lock-in transition, we found band reconstruction at high binding energy, which can be well explained by the hybridization between main bands (MBs) and folded bands (FBs). In contrast to the perfectly nested quasi-one-dimensional system, triple-nesting-vector-induced CDW FBs increase the degeneracy of the band crossing and thus further enlarge the magnitude of band gap at certain momentum-energy positions. The visualization and modelling of CDW gaps in momentum-energy space reconciles the long-lasting controversy on the gap magnitude and suggests an electron-phonon coupling mediated Peierls physics in the system.

2. *1T-$PtSe_2$* has recently been proposed to host type-II Dirac fermions. They are Lorentz-violating quasiparticles marked by a strongly tilted conic dispersion along a certain momentum direction and therefore have no analogues in the standard model. Using high-resolution ARPES, we systematically study the electronic structure of *1T-$PtSe_2$* in the full three-dimensional Brillouin zone. As predicted, a pair of type-II Dirac crossings is experimentally confirmed along the k_z axis. Interestingly, we have observed conic surface states around time-reversal-invariant momenta $\bar{\Gamma}$ and $\bar{M}$. The signatures of nontrivial topology are confirmed by the first-principle calculation,

which shows an intricate parity inversion of bulk states. Our discoveries not only contribute to a better understanding of topological band structure in *1T-$PtSe_2$* but also help further explore the exotic properties, as well as potential application, of group X TMDs.

3. *2M-WS_2* has recently been reported to exhibit the highest superconducting transition temperature T_c of 8.8 *K* among all pristine TMDs. Furthermore, first-principle calculation indicates a nontrivial band structure with a single surface Dirac cone at $\bar{\Gamma}$. The coexistence of topological surface state and superconducting phase make it a promising topological superconductor candidate. Using micro-ARPES and high-resolution ARPES, we can distinguish the *2M* phase from the trivial semiconducting *2H* phase. The ARPES measured electronic structure is in general consistent with the *ab initio* calculation and shows some signatures of the topological surface states. However, to acquire stronger evidence for topological superconducting phase, high-resolution ARPES measurement on high-quality pure *2M*-phase samples is required in the future.

Acknowledgement

The past four years as a DPhil student in Condensed Matter Physics, University of Oxford have been an amazing and unforgettable journey in my life. From a freshman getting used to the new place abroad and struggling in the research to the final stage of wrapping up my thesis, I gradually fall in love with the life in Oxford. As this is the very first time for me being in a part of a leading scientific research group, I find everything exciting and have learned to fit in the life as an experimental physicist. I realize that good research in our field always require close collaboration from a large group of people including colleagues in our group carrying out successful ARPES experiment, sample growers and theorists. Therefore, I would like to take this opportunity to express my sincere gratitude to all those who are with me in this long journey. Without their support and help, I would not accomplish the work presented in the thesis.

First, I feel truly lucky to become a DPhil student under the supervision of Prof. Yulin Chen. I really appreciate that he always keeps a high standard of our research, encourages and supports me throughout my entire DPhil course in Oxford. Even though he is super busy, he regularly spent time discussing with me which has always been inspiring. I would like to thank him for providing this platform to realize my ideas and carry out my research.

I want to thank my colleagues of Chen's group in Oxford including Cheng Chen, Han Peng, Ding Pei, Sandy Ekahana, Niels Schröeter and Chaofan Zhang. Cheng Chen is experienced in ARPES experiment in synchrotrons and always willing to offer help and help me to improve my experiment skills. I would like to attribute my improvement in Matlab coding to the help of Han Peng. I cannot be more thankful for the friendship among us and fruitful discussion in the collaboration.

I am also grateful for working with all the members in Chen's group around the world. Dr. Juan Jiang, a former postdoc researcher at Advanced Light Source, helped me with the experiment in my first project on 2H-$TaSe_2$ and she has always been a good friend to talk with. I would like to thank senior members, especially Prof. Zhongkai Liu, Prof. Lexian Yang, Dr. Haifeng Yang, Dr. Meixiao Wang for their help and insightful advice on my research project. I also want to thank all the graduate students: Xiang Xu, Shen Lei, Yujie Chen, Shucui Sun and Lu Kang from Tsinghua University, Chengwei Wang, Tao Deng, Jing

Zhang and Huijun Zheng from Shanghai Tech University for their help and accompany during the sleepless night during the beamtime.

I feel grateful to collaborate with amazing scientists outside Chen's group. Scientists at I05 beamline, Diamond Light Source including Cephise Cacho, Pavel Dudin, Timur Kim and Sungwon Jung are always supportive during our beamtime. It is impossible to produce so many high impact works from one of the most advanced ARPES facility without their effort. I also want to thank the scientists at Spectromicroscopy, Elettra synchrotron including Alexey Barinov, Viktor Kandyba and Alessio Giampietri for their generous help. I appreciate the collaboration with Dr. Dharmalingam Prabhakaran of Oxford, Claudia Felser group in Max Planck Institute, Dresden, Germany and Fuqiang Huang group in State Key Laboratory of High Performance Ceramics and Superfine Microstructure, Shanghai for providing high-quality samples; Yunyouyou Xia from Gang Li group in Shanghai Tech University, Chaoxing Liu from Pennsylvania State University, Dongqin Zhang from Haijun Zhang group from Nanjing University for the first-principle calculation.

Outside the academic life, I am lucky to have a bunch of friends in Oxford, such as Cheng Chen, Han Peng, Ding Pei, Jiahao Chen, Tian Zhang, Shilei Zhang, Penglin Cai, Heng Shen and Chelsea Xia. I cannot be more thankful to have some old friends who I keep in touch occasionally. I know Chang Yu, Yu Yan, Ming Yu, Zhenli Jiang for more than ten years. It is always fun to chat with them about music, movies and TV dramas I like. Liyuan Zheng, Wei Fu, Qingwen Wang, Jiasheng Zhang and Menglu Chen are my friends back in the undergraduate study in University of Science and Technology of China. All the friendship makes me less lonely along the journey and I will cherish it forever.

Most importantly, I cannot finish my DPhil course without the unconditional love and great support from my parents, Wan Li and Qing Lu. They always believe in me and make me the person who I am now.

I want to acknowledge the financial support from China Scholarship Council – University of Oxford Scholarship.

Finally, I would also like to thank Prof. Thorsten Hesjedal and Prof. Ming Yi for being the examiners of my thesis.

Publication List

1. **Yiwei Li**, Yunyouyou Xia, Sandy Adhitia Ekahana, Nitesh Jumar, Juan Jiang, Lexian Yang, Cheng Chen, Chaoxing Liu, Binghai Yan, Claudia Felser, Gang Li, Zhongkai Liu, Yulin Chen
   "Topological origin of the type-II Dirac fermions in $PtSe_2$"
   Physical Review Materials, 1, 074204 (2017)

2. **Y. W. Li**, J. Jiang, H. F. Yang, D. Prabhakaran, Z. K. Liu, L. X. Yang, Y. L. Chen
   "Folded superstructure and degeneracy-enhanced band gap in a weak-coupling CDW system"
   Physical Review B, 97, 115118 (2018)

3. Cheng Chen, Meixiao Wang, Jinxiong Wu, Huixia Fu, Haifeng Yang, Zhen Tian, Teng Tu, Han Peng, Yan Sun, Xiang Xu, Juan Jiang, Niels B. M. Schröter, **Yiwei Li**, Ding Pei, Shuai Liu, Sandy A. Ekahana, Hongtao Yuan, Jiamin Xue, Gang Li, Jinfeng Jia, Zhongkai Liu, Binghai Yan, Hailing Peng and Yulin Chen
   "Electronic Structures and Unusually Robust Bandgap in an Ultrahigh Mobility Layered Oxide Semiconductor, Bi_2O_2Se"
   Science Advances, 4, eaat8355 (2018)

4. D. F. Liu, A. J. Liang, E. K. Liu, Q. N. Xu, **Y. W. Li**, C. Chen, D. Pei, W. J. Shi, S. K. Mo, P. Dudin, T. Kim, C. Cacho, G. Li, Y. Sun, L. X. Yang, Z. K. Liu, S. Parkin, C. Felser, Y. L. Chen
   "Magnetic Weyl Semimetal Phase in a Kagomé Crystal"
   To be published in Science, eaav2873

5. X. Xu, S. L. Zhang, Z. R. Duan, Y. J. Chen, L. Kang, A. J. Liang, C. Chen, **Y. W. Li**, Y. Xu, P. Malinowski, J.-H. Chu, X. D. Xu, G. Li, Y. F. Guo, Z. K. Liu, L. X. Yang, Y. L. Chen
   "Spectroscopic Evidence for Local Magnetism in a van der Waals Ferromagnet Fe_3GeTe_2"
   Under Review of Physical Review Letters

6. Y. J. Chen, L. X. Xu, J. H. Li, **Y. W. Li**, H. Y. Wang, C. F. Zhang, H. Li, Y. Wu, A. J. Liang, C. Chen, S. W. Jung, C. Cacho, Y. H. Mao, S. Liu, M. X. Wang, Y. F. Guo, Y. Xu, Z. K. Liu, L. X. Yang, Y. L. Chen
   "Topological Electronic Structure and Its Temperature Evolution in Antiferromagnetic Topological Insulator $MnBi_2Te_4$"
   Under Review of Physical Review X

Abbreviations

ARPES	Angle-Resolved Photoemission Spectroscopy
BDP	Bulk Dirac Point
BS	Bulk State
BZ	Brillouin Zone
CB	Conduction Band
CDW	Charge Density Wave
CVD	Chemical Vapour Deposition
DLS	Diamond Light Source
DP	Dirac Point
DSM	Dirac Semimetal
EDC	Energy Distribution Curve
FB	Folded Band
FS	Fermi Surface
FZP	Fresnel Zone Plate
IS	Inversion Symmetry
Linac	Linear Accelerator
MB	Main Band
MDC	Momentum Distribution Curve
MIP	Maximum Intensity Projection
PES	Photoemission Spectroscopy
QSH	Quantum Spin Hall
SDP	Surface Dirac Point
SO	Schwarzschild Objective
SOC	Spin-Orbital Coupling
SS	Surface State
STM	Scanning Tunnelling Microscopy
TB	Tight Binding
TDSM	Topological Dirac Semimetal
TI	Topological Insulator
TMD	Transition Metal Dichalcogenide
TRIM	Time Reversal Invariant Momentum
TRS	Time Reversal Symmetry
TSC	Topological Superconductor
TSM	Topological Semimetal
TSS	Topological Surface State
TWSM	Topological Weyl Semimetal
VB	Valence Band
WP	Weyl Point

Contents

Chapter 1. Introduction to Angle-Resolved Photoemission Spectroscopy 1
1.1 General Principles of Photoemission Process 2
1.1.1 Experiment geometry 2
1.1.2 Momentum and Energy Conservation of Photoemission Process 4
1.1.3 Interpretation of ARPES Intensity 7
1.2 Data Analysis Techniques 13
1.2.1 Angle to parallel momentum conversion 13
1.2.2 Photon energy to perpendicular momentum conversion 16
1.2.3 Data visualization techniques 21
1.2.4 Maximum intensity projection and 3D visualization 24
1.3 Facilities: synchrotron-based ARPES 28
1.3.1 I05 branch at DLS 28
1.3.2 Spectromicroscopy branch at Elettra 31
References 33

Chapter 2. Overview of Transition Metal Dichalcogenides 37
2.1 Crystal Structure 38
2.1.1 *2H* structure 40
2.1.2 *1T* structure 41
2.1.3 *2M* structure 43
2.2 Electronic Structure 44
2.2.1 ***d***-orbit filling of the transition metal element 44
2.2.2 Coordination environment of the transition metal 47
2.2.3 Spin-orbit coupling 48
2.3 Exotic Properties 50
2.3.1 Charge density waves and superconductivity 50
2.3.2 Nontrivial topological band structure 52
2.3.3 Other interesting properties as 2D materials 54
References 56

Chapter 3. ARPES Study on the CDW System *2H-TaSe*$_2$ 66
3.1 Overview of CDW in *2H-TaSe*$_2$ 68
3.2 Band Structure of the High-temperature Phase 70

3.2.1 In-plane band structure 70
3.2.2 Out-of-plane band structure 72
3.3 Fine Structure of Folded Bands in the Low-temperature CDW phase 75
3.3.1 Band structure reconstruction in CDW phase 75
3.3.2 CDW folded bands (FBs) and new translational symmetry 77
3.4 Distribution of the Magnitude of CDW Gaps in the Momentum-Energy Space 80
3.4.1 Distribution of the location of CDW gaps in the momentum space 80
3.4.2 Nesting degeneracy enhanced CDW gaps 82
3.5 Electronic Susceptibility 85
3.6 General Model of CDW in 2H-TMDs:
Electron-phonon Coupling mediated FS Nesting 87
Method 91
References 92

Chapter 4. ARPES Study on the Type-II Dirac Semimetal *1T-PtSe*$_2$ 97
4.1 Crystal Structure and Symmetry 98
4.2 Band Structure in the 3D BZ 100
4.2.1 Determination of the high-symmetry points along k_z 100
4.2.2 General band structure 101
4.2.3 Detailed band structure near E_F 104
4.2.4 Distinguish surface and bulk states 106
4.3 Type-II Dirac Cone 108
4.3.1 Visualization of the four-dimensional type-II Dirac cone 108
4.3.2 Anisotropy of type-II bulk Dirac cone in *1T-PtSe*$_2$ 111
4.4 Topological Surface States 112
4.4.1 Topological Surface State at $\bar{\Gamma}$ 112
4.4.2 Topological Surface State at $\bar{M}$ 114
4.5 Interpretation of Topological Band Structure 115
4.5.1 Interpretation of the type-II bulk Dirac point 116
4.5.2 Interpretation of the TSSs and band inversions 116
Method 118
References 119

Chapter 5. ARPES Study on the Mixture Phases of *WS*$_2$ 124
5.1 Spatially Resolved *2H/2M* phases 125
5.1.1 Core level 125

5.1.2 Fermi surface and symmetry of *2M/2H* phases 127
5.1.3 Domain alignment of *2M* and *2H* phases 129
5.2 Band Structure of *2M*-WS_2 131
5.2.1 *Ab initio* calculation 131
5.2.2 Fermi surface 132
5.2.3 Band dispersion 133
5.3 Signatures of Topological Band Structure 135
5.3.1 Potassium dosing 135
5.3.2 Zoomed-in FS mapping near $\bar{\Gamma}$ 136
5.3.3 Signature of the topological surface state at $\bar{\Gamma}$ 138
5.4 Discussion and Conclusion 139
Method 140
References 142

Chapter 6. Summary and Future Works 145
6.1 Summary 145
6.2 Future works 146
6.2.1 Artificial 2D twistronics and gating-devices 146
6.2.2 Phase-separated materials 148
References 150

Appendix
A. Nonsymmorphic Symmetry Protected Dirac Nodal Lines in Space Group *P63/mmc* 152
A.1 Spinless case 152
A.2 The effect of spin-orbit coupling 154
B. Fermi Surface Folding in *2H*-$TaSe_2$ 156
C. k_z-effect in *2H*-$TaSe_2$ 159
D. Validity of Maximum Intensity Projection 161
E. Orbital Resolved Bulk Band Structure of *1T*-$PtSe_2$ 163
References of Appendix 164

List of Figures and Tables

Fig. 1.1 Evolution of PES experiment **4**

Fig. 1.2 Diagram showing the conservation of energy and momentum in the photoemission process **6**

Fig. 1.3 Schematic illustration of the one-step model and three-step model **8**

Fig. 1.4 Spectra of ARPES. **11**

Fig. 1.5 In situ cleavage method and the universal curve of the electron mean free path **12**

Fig. 1.6 Geometry and coordinate systems of ARPES measurement **14**

Fig. 1.7 Determination of first Γ using two photon energies **15**

Fig. 1.8 Determination of the first Γ under fixed photon energy **16**

Fig. 1.9 Schematics of the photoemission process within the three-step nearly-free-electron final state model **17**

Fig. 1.10 Photon-energy-dependent measurement of *1T-*$PtSe_2$ **19**

Fig. 1.11 Inner potential of copper V_0 as a function of the electron energy E **21**

Fig. 1.12 Comparison of three data enhancement methods **24**

Fig. 1.13 Schematic illustration of the principle of maximum intensity (MIP) for gap detection **26**

Fig. 1.14 MIP method on *2H-*$TaSe_2$ data **27**

Fig. 1.15 3D visualization of ARPES data on the band structure near M point of *2H-*$TaSe_2$ in the low-temperature phase from different perspectives **28**

Fig. 1.16 Diamond Light Source (DLS), Harwell campus, UK **29**

Fig. 1.17 Sketch of the optical system of Beamline I05 at DLS **30**

Fig. 1.18 Elettra synchrotron, Trieste, Italy **31**

Fig. 1.19 Sketch of the optical system of Beamline Spectromicroscopy **32**

Fig. 2.1 *H* and *T* structure of TMDs **38**

Fig. 2.2 *T'* structure of TMDs **39**

Fig. 2.3 Bulk TMD crystal structure based on different stacking geometry **40**

Fig. 2.4 Non-symmorphic symmetry of *2H-*MX_2 ..... **41**

Fig. 2.5 Symmetry operation elements of *1T-*MX_2 ..... **42**

Fig. 2.6 Characteristic results of STM and Raman measurement on the *2M-*WS_2 single crystal **43**

Fig. 2.7 Electronic structure dependence on the *d*-orbit filling of transition metal atoms **46**

Fig. 2.8 Electronic structure dependence on the coordination environment of the transition metal **48**

Fig. 2.9 Electronic structure dependence on the strength of SOC 49
Table 2.1 Summary of CDW and superconducting states in selected TMDs 52
Table 2.2 Summary of TMDs with topologically nontrivial band structures 54

Fig. 3.1 Superlattice formation and FS reconstruction in the CDW phase transition ... 69
Fig. 3.2 ARPES measured and Tight-binding (TB) reconstructed band structure in the normal phase 71
Fig. 3.3 Non-symmorphic symmetry protected band degeneracy 73
Fig. 3.4 k_z-dependent ARPES measurement from $\Gamma - M$ to $A - L$ 74
Fig. 3.5 Band structure reconstruction in 3×3 CDW phase 76
Fig. 3.6 Weak FBs features with new periodicity on top of MBs 78
Fig. 3.7. Pure folded features at $\bar{\Gamma}$ 79
Fig. 3.8 Maximum intensity projection (MIP) and CDW gap candidates 81
Fig. 3.9 Band dispersion along CDW gap candidates 83
Fig. 3.10 Bare electronic susceptibility of *2H-$TaSe_2$* 86
Fig. 3.11 Schematics of 1D and 2D Peierls CDW model 89

Fig. 4.1 Crystal structure and Brillouin zone (BZ) of *1T-$PtSe_2$* 99
Fig. 4.2 k_z-dependent measurement via continuously changing photon energy of *1T-$PtSe_2$* 101
Fig. 4.3 General electronic band structure of *1T-$PtSe_2$* 103
Fig. 4.4 Detailed band structure near E_F of *1T-$PtSe_2$* 105
Fig. 4.5 Bulk and surface states in *1T-$PtSe_2$* 107
Fig. 4.6 Type-II Dirac cone in *1T-$PtSe_2$* 109
Fig. 4.7 3D visualization of type-II Dirac cone 111
Fig. 4.8 Anisotropy of type-II bulk Dirac cone in *1T-$PtSe_2$* 112
Fig. 4.9 TSSs at $\bar{\Gamma}$ 113
Fig. 4.10 TSS at $\bar{M}$ 115
Fig. 4.11 Schematic of bulk band hybridizations and inversion along k_z 117

Fig. 5.1 Spatially resolved *2H/2M* phases 127
Fig. 5.2 Fermi surface and symmetry of *2H/2M* phases 128
Fig. 5.3 Domain alignment of *2H* and *2M* phases 130
Fig. 5.4 *Ab initio* calculated electronic structure of *2M-WS_2* 132
Fig. 5.5 Fermi surface of *2M-WS_2* near $\bar{\Gamma}$ 133
Fig. 5.6 Band dispersion of *2M-WS_2* 134
Fig. 5.7 Potassium dosing of *2M-WS_2* 136

Fig. 5.8 Zoomed-in FS mapping near $\bar{\Gamma}$ 137
Fig. 5.9 Signature of the topological surface state $\bar{\Gamma}$ 138

Fig. 6.1 Artificial twistronics and gating-devices 147
Fig. 6.2 Chiral domain configuration in *2H-*$Fe_{1/3}TaS_2$*, 2H-*$Fe_{1/4}TaS_2$ and $Ca_{2.55}Sr_{0.45}Ti_2O_7$ 149

Fig. B1 3×3 Fermi surface (FS) folding 157
Fig. B2 Comparison between experimental FS contours and tight-binding model based on FS folding at different binding energies from E_F to $E_F - 0.3$ eV 158
Fig. C k_z-dependent electronic structure 160
Fig. D. Consistent gap size measured by conventional method and MIP 162
Fig. E *Ab initio* calculation of bulk band structure of *1T-*$PtSe_2$ 163

Chapter 1

Introduction to Angle-Resolved Photoemission Spectroscopy

Electronic band structure of crystalline materials describes the electron distribution in the momentum-energy space. In the field of condensed matter physics, band theory, as one of the most fundamental models, has been successfully applied to explain physical properties of solids, such as electrical transport and light-matter interaction. It also provides a foundation of understanding solid-state devices including all kinds of electronics. Band structure, beyond a theoretical model, can be directly detected by angle-resolved photoemission spectroscopy (ARPES).

The definition and experimental measurement form unseparated integrity for any physical quantities. It works the same for the electronic structure of crystalline systems. In this chapter, we will give a brief introduction to ARPES and explain how it can visualize the band structure. The chapter contains three sections. In the first section, the general principles of the photoemission process are introduced; in the second section, the data analysis techniques that will be further used in the thesis are presented; and in the last section, two synchrotron-based ARPES beamlines at Diamond Light Source (DLS) and Elettra are introduced. All the ARPES data presented in the thesis are collected using these two facilities.

1.1 General Principles of Photoemission Process

1.1.1 Experiment geometry

The photoemission process, also referred as the photoelectric effect, was first experimentally discovered by Hertz [1]. He revealed that electrons of a metallic material can be emitted when it is shined on by light over a certain energy threshold. The mathematical description was then introduced by Einstein [2] in 1905 for which he was later awarded the Nobel Prize in 1921 by invoking the quantum nature of light, the photon.

Since then, photoemission spectroscopy (PES) has been extensively used as a powerful experimental technique in the study of the electronic structure of condensed matter systems. The experimental technique has been advanced, and the geometry has been changed over the last hundred years as shown in Fig. 1.1. Schematics of early PES is illustrated in Fig. 1.1(a). The surface of the sample is illuminated by monochromatized light and the maximum kinetic energy of the photoelectron was measured by the retarding voltage which is just large enough to entirely suppress the outgoing electron. From this experiment, one can (1) determine the ratio of Planck's constant to the electronic charge, $\hbar/\mathrm{e}$; and (2) measure the work function difference between the anode and the cathode material. The basic equation as shown in Fig. 1.1(a)(i) describes this experiment is:

$$eU = E_{kin,max} = h\nu - \Delta\phi, \tag{1.1}$$

where U is the retarding voltage, $E_{kin,max}$ is the maximum kinetic energy of photoelectrons, $h\nu$ is the photon energy, and $\Delta\phi$ is the work function of the system.

A modern PES experiment geometry is illustrated in Fig. 1.1(b). The retarding voltage is replaced by an energy analyzer which can record the energy distribution of photoelectron in a certain direction. In principle, the angle distribution of the emitted electron can be also

measured if either the sample stage or the analyser has the rotation freedom. This is restrained by the relative low efficiency from (1) low brilliance of light source which results in a low count of photoelectrons, and (2) the point detector of the analyser which make the scanning of angle space time-consuming. However, one can acquire the core-level spectrum of the sample, such as the one shown in Fig 1.1(b)(ii) measured on $1T - PtSe_2$.

With the advance of high brilliance light sources, such as synchrotrons and lasers, and the application of energy analyzers with an entrance slit which accepts the outgoing electron in an angle range window, angle-resolved photoemission spectroscopy (ARPES) can detect both the energy and the angular distribution of photoelectrons. The definition of the photoemission angle direction (θ, ϕ) varies in different facilities. We adopt the convention used in Diamond Light Source (DLS) I05 branch in this thesis. As shown in Fig. 1.1(c), one takes a 'snapshot' at each polar angle θ with the acceptance angle window ϕ along the slit, called 'cut' in the ARPES experiment, and then by combining all the cuts, one gets the 3D intensity 'map' $I(E_{kin}, \theta, \phi; h\nu)$. In section 1.2, we will elaborate on how to calculate the band structure $E(\boldsymbol{k})$ from ARPES intensity $I(E_{kin}, \theta, \phi; h\nu)$.

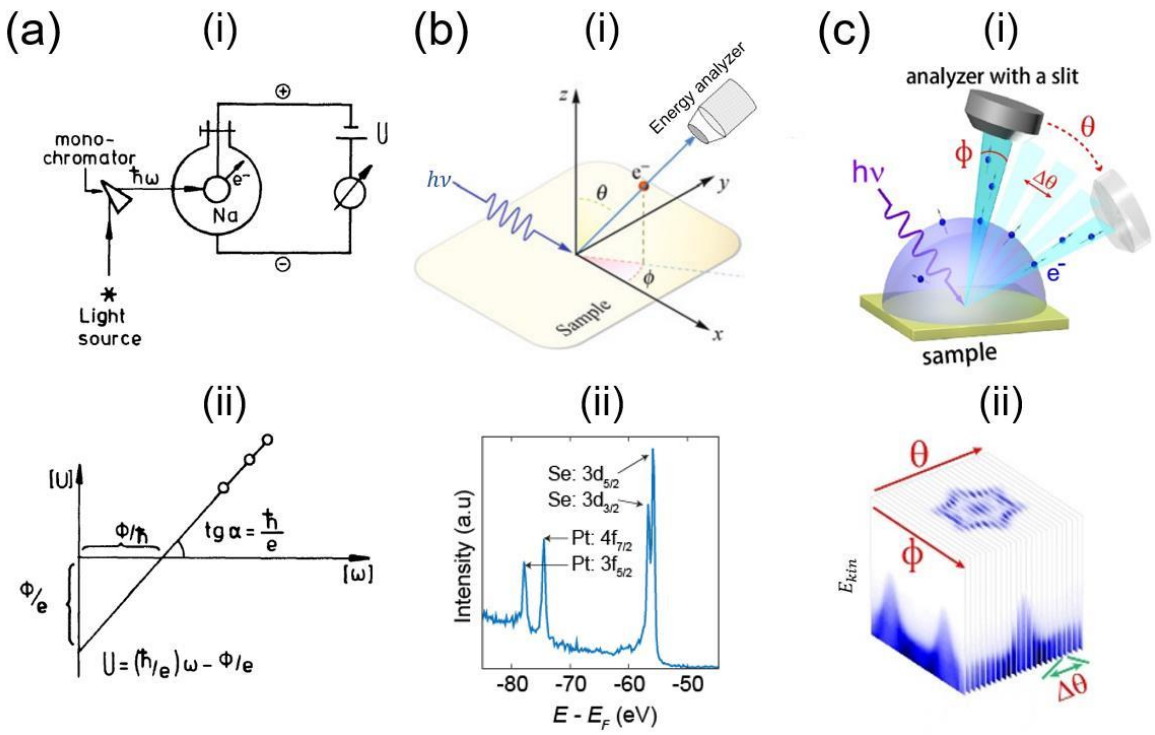


Fig. 1.1 Evolution of PES experiments. (a) Setup of early PES experiment (i) and its typical result (ii). (b) Schematic of modern PES experiment with a point energy analyser (i) and its typical core-level spectrum (ii). (c) Schematic of modern ARPES measurement with an energy analyser with a slit (i) and its typical mapping measurement (ii). (a) is reproduced from Ref. [3]. (b) is adapted from Ref. [4]. (c) is adapted from Ref. [5].

1.1.2 Momentum and Energy Conservation of Photoemission Process

It is the conservation law of momentum and energy that justify the idea that, in a photoemission experiment, by measuring the momentum and energy of the free photoelectron we can deduce the crystal momentum and binding energy before it is excited. In this section, some approximations are applied which simplify the complicated microscopic picture of photoemission process: (1) the band structure describing the electron inside the crystal is “single electron states” which assumes that the electron travels in a static periodic potential in the solid; (2) the incident photon only interact with one certain single

electron state and excite to the final free electron state. The first approximation excludes the many-body interactions and regards them as a part of the periodic crystal potential. In the second approximation, it is assumed that the "environment", the periodic potential, remains unchanged after the photoemission. This is an oversimplified picture, and more elaborated interpretation is introduced in section 1.1.3.

Based on the aforementioned approximations, Fig. 1.2 shows the conservation law that connects the energy and momentum of the photoelectron with those of the electron before the photoemission. During the photoemission, since the initial single electron state is excited to the final state after complete absorption of the photon energy, the energy conservation is described as

$$E_f = E_i + h\nu. \tag{1.2}$$

$E_{f,i}$ denotes the energy of the final/initial state. Here, they are referred to the same energy reference. However, since the final state is a free electron state in the vacuum, the natural reference then is the static free electron energy in the vacuum so that the final state energy is the kinetic energy. For the initial state, the Fermi level is commonly used as the reference which indicate the highest energy level for the occupied state in the zero temperature. Thus, we rewrite Eq. (1.2) as

$$E_{kin} = h\nu - \phi - |E_b|. \tag{1.3}$$

E_{kin} is the kinetic energy of the photoelectron, $E_b = E_F - E_i$ is the binding energy, ϕ is the work function for the whole photoemission setup.

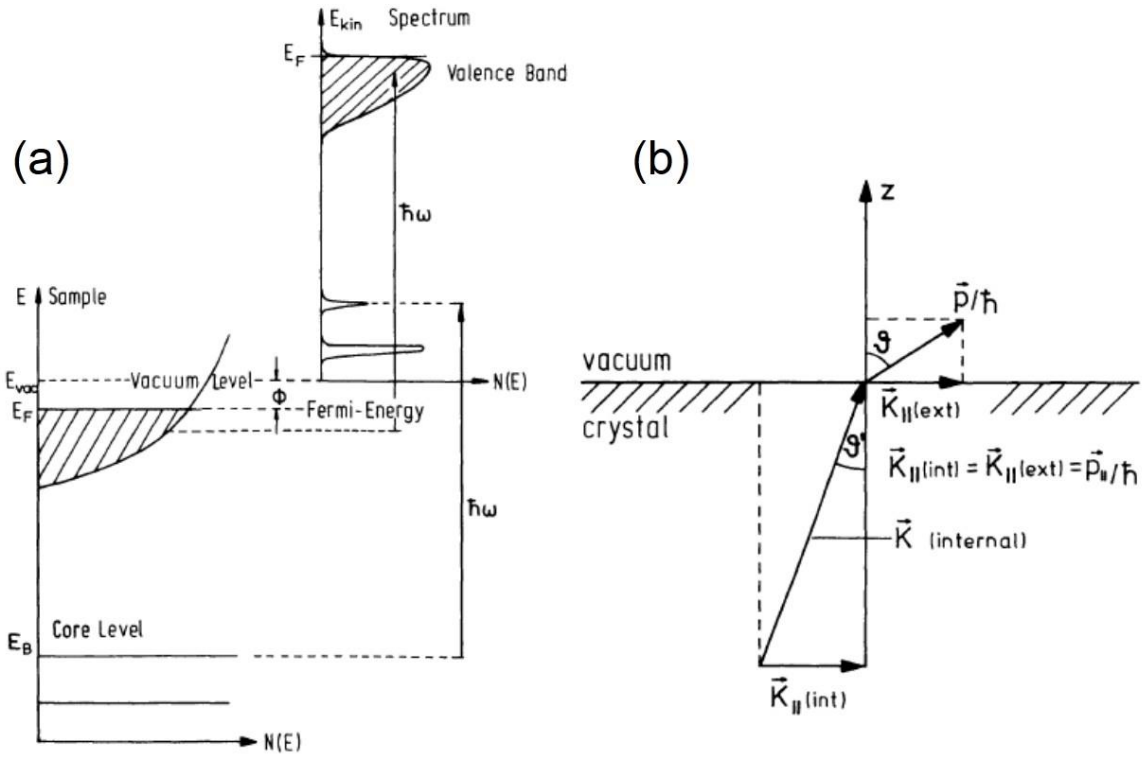


Fig. 1.2 Diagram showing the conservation of energy (a) **and momentum** (b) **in the photoemission process.** This figure is adapted from Ref. [3].

Figure 1.2(b) shows the relation of momenta at the interface between the crystal and vacuum. Momentum conservation is a direct consequence of space translation symmetry. In the crystal, the continuous translation symmetry is replaced by discrete lattice symmetry, thus the momentum is replaced by the crystal momentum [3]. For the photoemission process, the (discrete) translation symmetry is preserved along the parallel direction to the crystal/vacuum interface, however, it is broken along the perpendicular direction. Therefore, the momentum is only conserved along the parallel direction

$$K_{\parallel}^{f} = k_{\parallel}^{i} + G_{\parallel},$$
$$K_{\perp}^{f} \neq k_{\perp}^{i} + G_{\perp}. \tag{1.4}$$

K denotes the real momentum of the electron and k denotes the crystal momentum of the electron inside the solid, whereas *i* and *f* denotes the initial and final states. *G* is an arbitrary reciprocal vector of the lattice. This is a direct consequence of the discrete translation symmetry of the crystal in contrast to the continuous symmetry in the vacuum. Please note here, we neglect the photon momenta because they are relatively small compared to that of a photoelectron in the photon energy range below 200 eV.

In summary, using this simplified picture of photoemission, we demonstrate the idea that the momentum and energy information of the photoelectron ($\boldsymbol{K}, E_{kin}$) can be traced back to single electron state in the periodic crystal potential ($k_{\parallel}, E_b$). The interpretation of ARPES intensity based on a more elaborated process including many-body interaction is presented in section 1.1.3 and the conversion from the raw ARPES data to the momentum-energy space is further demonstrated in section 1.2.1 and section 1.2.2.

1.1.3 Interpretation of ARPES Intensity

It is believed that photoemission is an immediate process in which the photon-electron interaction excites the initial Bloch wave electron to a final state whose wave function propagates freely in the semi-infinite vacuum but decays away from the crystal-vacuum interface into the solid. In this "one step" picture, both the initial and the final state wave function should be described in the context of crystal and vacuum each occupying half of the space. There should be no more structures for the excitation. However, a more widely used way to interpret ARPES intensity is the so-called "three-step" model. It consists of (1) photoexcitation of a Bloch wave electron in an infinite crystal, (2) the excited electron travels to the surface and (3) its transmission through the interface into the vacuum. The comparison between one-step and three-step model is illustrated in Fig. 1.3.

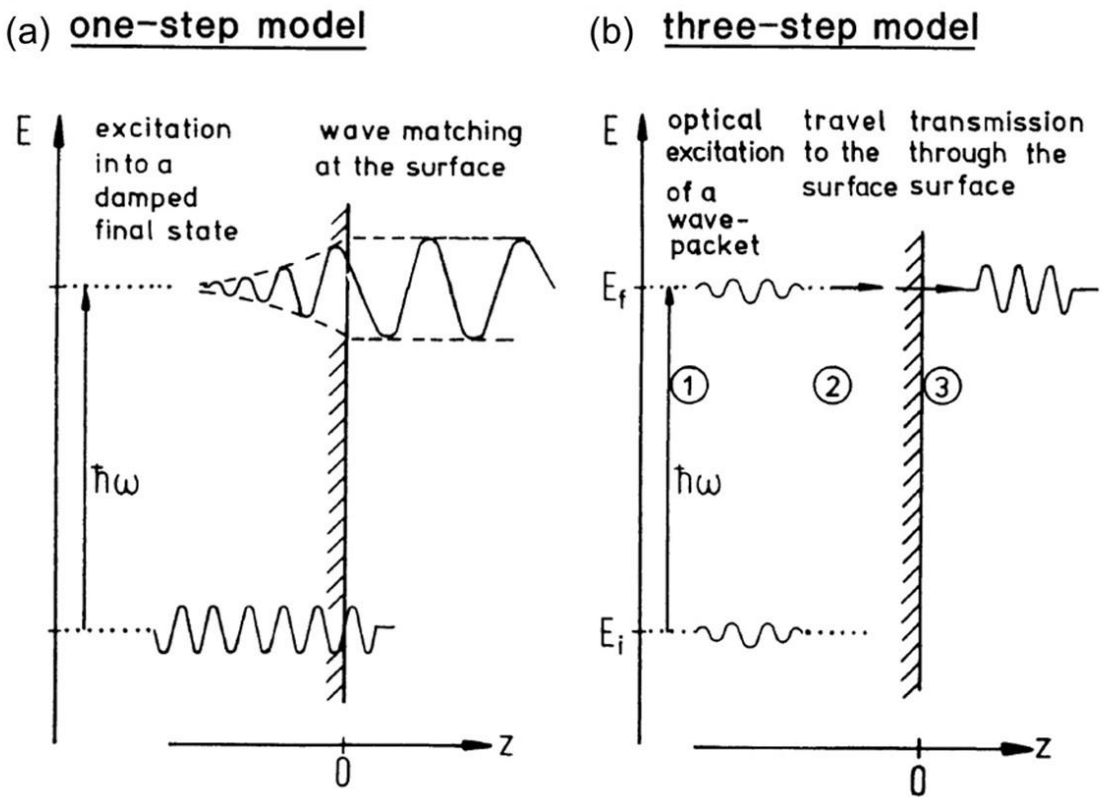


Fig. 1.3 Schematic illustration of the one-step model (a) **and three-step model** (b). The figure is adapted from Ref. [3].

The three-step model is valid if we choose the initial state wave packet whose space extension *D* along *z* (surface normal) is substantially larger than the crystal periodicity *c* (~1 nm) while substantially smaller than the photon penetration depth α^{-1} (~1 μm for $h\nu$~100 eV). The condition of $D \gg c$ ensures that the initial and final state in the first step can be described by a bulk Bloch wave, whereas $D \ll \alpha^{-1}$ shows that the excited state (the final state of the first step), on average, is far away from the surface. Therefore, the three-step model can be regarded as a reasonable approximation of the more realistic one-step picture.

In the first step, we take the many-body interaction into account. The transition probability between N electron initial state Ψ_i^N and final state Ψ_f^N is calculated by Fermi's Golden Rule,

$$w \propto \frac{2\pi}{\hbar}\left|\left\langle \Psi_f^N \middle| H_{int} \middle| \Psi_i^N \right\rangle\right|^2 \delta(E_f^N - E_i^N - h\nu), \tag{1.5}$$

The electron-photon interaction Hamiltonian is

$$H_{int} = \frac{e}{mc}\boldsymbol{A}\cdot\boldsymbol{p}, \tag{1.6}$$

where $\boldsymbol{A}$ is the vector potential of the photon field and $\boldsymbol{p}$ is the momentum operator.

Since N is an extremely large number (~10^{23}) for the real system, some approximations must be applied to simplify the calculation. One of the commonly used approximations is the one-electron view of the initial and final state. Then we can rewrite them as a product of the single electron wave function of the electron that has been excited (or to be excited) and the wave function for the remaining $N-1$ electrons:

$$\begin{aligned}
\Psi_\mathrm{f}^N &= C\phi_{f,k}\Psi_{f.k}^{N-1},\\
\Psi_i^N &= C\phi_{i,k}\Psi_{i,k}^{N-1},\\
E_f^N &= E_{kin} + E_{f,k}^{N-1},\\
E_i^N &= -|E_b| + E_{i.k}^{N-1},
\end{aligned} \tag{1.7}$$

where C is the fermionic antisymmetric operator, ϕ is the wave function of the photoelectron, $\Psi^{\mathrm{N}-1}$ is the wave function of the $N-1$ remaining electron system. Then we can rewrite the transition probability in Eq. (1.5) as

$$\left\langle \Psi_f^N \middle| H_{int} \middle| \Psi_i^N \right\rangle = \left\langle \phi_{f,k} \middle| H_{int} \middle| \phi_{i,k} \right\rangle \left\langle \Psi_{f,k}^{N-1} \middle| \Psi_{i,k}^{N-1} \right\rangle. \tag{1.8}$$

Now the right-hand part of Eq. (1.8) consists of a one-electron matrix element and a $(N-1)$-electron overlap integral. If the studied system is weakly coupled, one can assume that

the remaining $N-1$ electron cannot "feel" the photoemission process, also called the frozen-orbital approximation, meaning that $\langle \Psi_{f,k}^{N-1} | \Psi_{i,k}^{N-1} \rangle = 1$. Under this assumption, only the one-electron matrix element can play a part which describe the same picture as we have introduced in section 1.1.2. Therefore, in a weak-coupling system, ARPES intensity renders exactly the band structure of the system as shown in Fig. 1.4(b)

$$I(\boldsymbol{k}, E_{kin}) \propto \delta(E_{kin} + |E_b| - h\nu - \phi)\delta(\boldsymbol{k_i} + \boldsymbol{G} - \boldsymbol{k}_f). \tag{1.9}$$

Please note that here we only account for the first step of the three-step model, thus the crystal momentum of the electron is conserved. This interpretation of ARPES intensity under the frozen orbital approximation, however, is not affected when the probabilities of the second and third steps are applied.

However, for a more general situation including many-body interactions, this approximation is invalid. For the remaining $N-1$ electron system, we assume the photoemission excites them to a state which can be expanded to a series of eigen wave functions $\Psi_{f,k,s}^{N-1}$ with energy E_s^{N-1}. Then the $(N-1)$-electron overlap integral can be written as

$$\langle \Psi_{f,k}^{N-1} | \Psi_{i,k}^{N-1} \rangle = \sum_s \langle \Psi_{f,k,s}^{N-1} | \Psi_{i,k}^{N-1} \rangle. \tag{1.10}$$

The ARPES intensity now has the form:

$$I \propto \sum_{f,i,k} M_{f,i,k} \times \sum_s \left| \langle \Psi_{f,k}^{N-1} | \Psi_{i,k}^{N-1} \rangle \right|^2 \times \delta\left(E_{f,E_k} + E_s^{N-1} - E_i - h\nu\right), \tag{1.11}$$

with the one-electron matrix element

$$M_{f,i,k} = \left| \langle \phi_{f,k} | H_{int} | \phi_{i,k} \rangle \right|^2, \tag{1.12}$$

and spectral function

$$A = \sum_s \left| \langle \Psi_{f,k}^{N-1} | \Psi_{i,k}^{N-1} \rangle \right|^2. \tag{1.13}$$

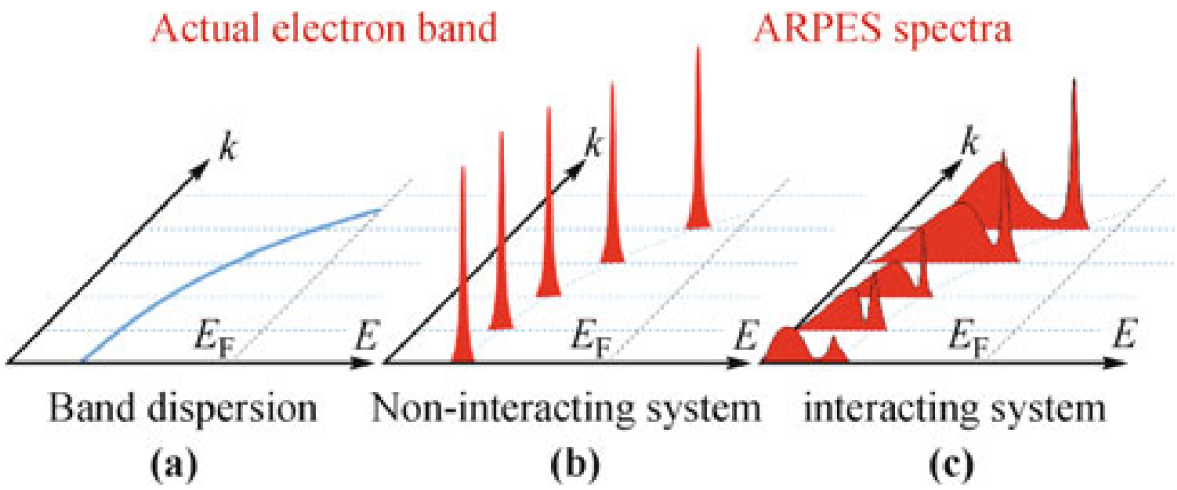


Fig. 1.4 Spectra of ARPES. (a) True dispersion of an electronic band. (b) Momentum-resolved ARPES spectra from a non-interacting electron system. (c) Momentum-resolved ARPES spectra from an interacting electron system. This figure is adapted from Ref. [4].

This reflects the main feature of ARPES of a strong-correlated system which shows the main peak, the band structure part, accompanied by satellite peaks containing the information of the excited photo-hole system, namely the remaining $(N-1)$-electron assembly. A typical illustration of the ARPES intensity plot on a strong-correlated system is shown in Fig. 1.4(c).

We have shown above that the main features of final ARPES intensity $I(\boldsymbol{k}, E_{kin})$ originate from the first step, the photoexcitation process, of the three-step model. In the following second and third steps, the number of outgoing photoelectrons is further reduced. The total count of photoelectrons then is a product of the number of initial photoexcitation electrons, the probability of reaching the surface in the second step and the probability of transmission through the surface in the third step.

On the way of traveling towards the crystal surface, the photoelectrons may get scattered by electron-electron and electron-lattice interaction. Thus, the photoelectrons closer to the

surface are more likely to reach the surface. This makes ARPES a surface-sensitive technique and requires a fresh sample surface by cleavage, as shown in Fig. 1.5(a), in a ultra-high vacuum (other sample preparation method includes *in-situ* grown films, single crystal polished, sputtered and annealed). The surface sensitivity of ARPES is dictated by electron mean free path, which is the average distance traveled before being scattered. Since the mean free path of the electron depends on its kinetic energy, as shown in Fig. 1.5(b), we can choose a favorable photon energy range to detect bulk or surface electrons. In the photon energy range that we use in the synchrotron-based ARPES (10~200 eV), the electron mean free path is about 1~2 nm, only covering a very few unit cells ($c \approx 0.5$ nm). Therefore, in this photon energy range, both bulk and surface states can be detected, making synchrotron-based ARPES a powerful tool for the study of quantum materials.

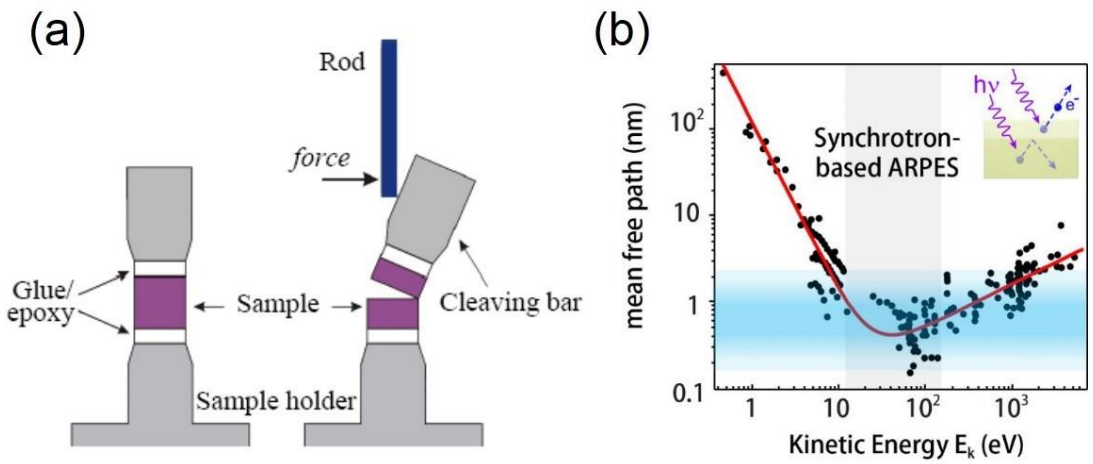


Fig. 1.5 *In situ* cleavage method and the universal curve of the electron mean free path. (a) Single crystal sample preparation in an ARPES experiment. The crystalline sample is mounted on the sample holder by conductive glue/epoxy. A cleaving bar is attached to the top surface of the crystal. Before the measurement, the bar is knocked off in the ultra-high vacuum then the fresh surface is exposed. (b) The "universal curve" for surface sensitivity in photoemission. Mean free path versus kinetic energy of photoelectron is measured by various materials. (a) is reproduced from Ref. [6]. (b) is reproduced from Ref. [5].

In the third step, only a fraction of photoelectrons can go through the energy barrier, the so-called work function, at the surface while others are bounced back. For those outgoing electrons, the parallel momentum is conserved, however, since the kinetic energy is lost through the energy barrier, the perpendicular momentum is not conserved. To determine the perpendicular momentum (k_z) is not a trivial process and the method will be elaborated in section 1.2.2.

1.2 Data Analysis Techniques

1.2.1 Angle to parallel momentum conversion

As shown in Fig. 1.6(a), by measuring the kinetic energy and direction of the emitted photoelectron, we can deduce its momentum in the sample stage coordinate system:

$$\begin{aligned} k &= \frac{\sqrt{2m_e E_{kin}}}{\hbar}, \\ k_x^{stage} &= k\cos\phi\sin\theta, \\ k_y^{stage} &= k\sin\phi, \\ k_z^{stage} &= k\cos\phi\cos\theta. \end{aligned} \tag{1.14}$$

Here, we define $(\theta, \phi) = (0,0)$ to be the normal direction of the sample stage. We notice that, for small $\theta \ll 1$ and $\phi \ll 1$, $k_x \propto \theta$, $k_y \propto \phi$. Thus, from the raw data $I(E_{kin}, \theta, \phi)$, we can already see the major features and symmetry of the band structure $E(k_x, k_y)$.

However, in a real experiment, the situation of the cleavage surface of the crystalline sample can be complicated. Usually, the sample surface is not perfectly parallel to the

sample stage, as shown in Fig. 1.6(b). Thus, the momentum in the sample coordinate system must be converted from the sample stage coordinate system by a rotation matrix:

$$\boldsymbol{k}_{sample} = \mathbf{R}(\theta_\Gamma, \phi_\Gamma; \Omega)\boldsymbol{k}_{stage}. \tag{1.15}$$

$\mathbf{R}(\theta_\Gamma, \phi_\Gamma; \Omega)$ is the rotation matrix for the conversion between two coordinate systems. $(\theta_\Gamma, \phi_\Gamma)$ defines the normal direction of the sample surface in the stage coordinate system, while Ω denotes the in-plane rotation angle of the sample (azimuth).

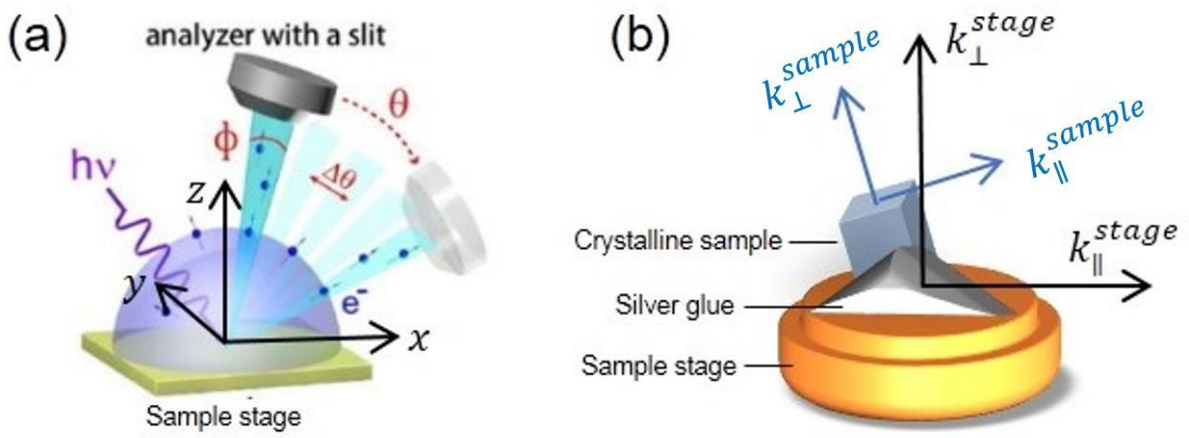


Fig. 1.6 Geometry and coordinate systems of ARPES measurement. (a) The ARPES experiment geometry. (b) The coordinate systems of the sample stage and sample. (a) is reproduced from Ref. [5].

The determination of the first Γ position $(\theta_\Gamma, \phi_\Gamma)$ is not trivial. In the rest of this section, we will present two commonly used methods. The first method is suitable for experiments with tuneable photon energy while the second is applied when only fixed photon energy is available.

From the conversion presented above, one can notice that there is a fixed point from the angle-space to the momentum-space. The emitted electron with zero parallel momentum would be always in the direction perpendicular to the surface normal, which is $(\theta_\Gamma, \phi_\Gamma)$, no

matter what photon energy is applied. In comparison, for an arbitrary photoelectron with certain nonzero parallel momentum, higher photon energy would result in larger momentum thus smaller emitted angle about the surface normal. Therefore, by changing the photon energy, the observed Fermi surface (FS) is zoomed-in in the low photon energy range and zoomed-out in the high photon energy range while keep the centre at the $(\theta_\Gamma, \phi_\Gamma)$.

Figure 1.7 shows a typical measurement using a synchrotron light source. The $OsTe_2$ single crystal after cleavage clearly has a complicated surface which is not parallel to the sample stage. By Fermi surface mapping at two different photon energies (85 eV and 150 eV), we can identify the fixed point as the first Γ at $(\theta_\Gamma, \phi_\Gamma) = (-9.6, 0.4)$.

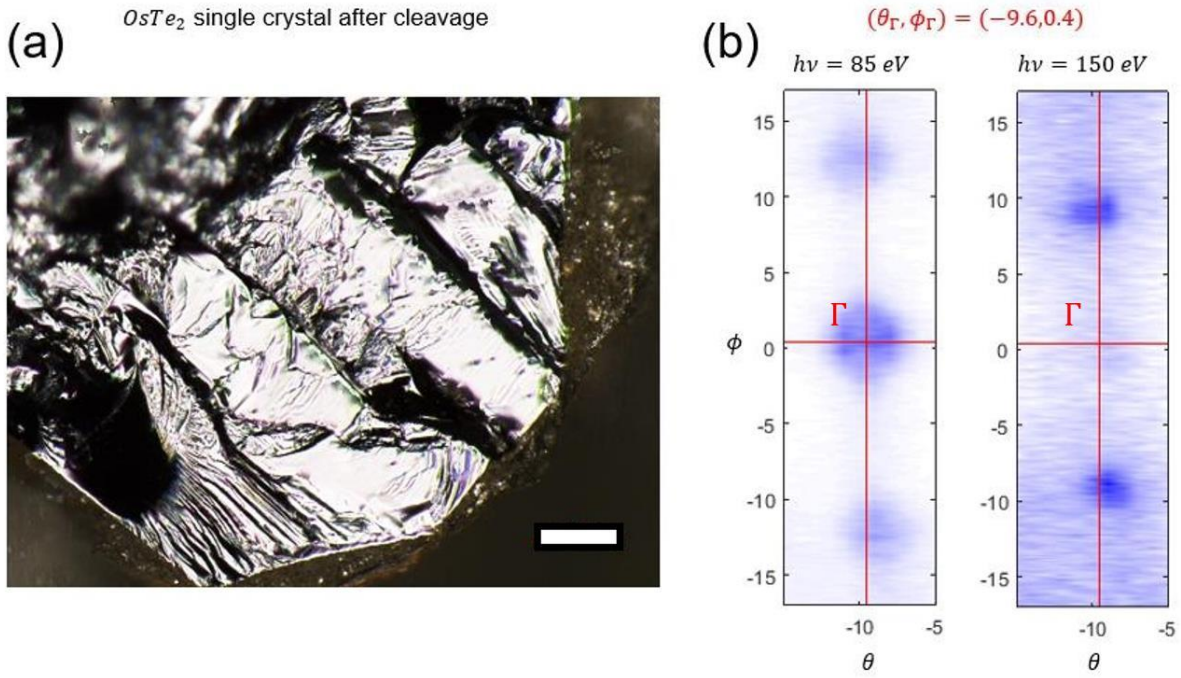


Fig. 1.7 Determination of first Γ using two photon energies. (a) Optical image of $OsTe_2$ single crystal after cleavage. Scale bar is 100 μm. (b) By Fermi surface mapping using two photon energies at 85 eV and 150 eV, we can identify the fixed point as the first Γ at $(\theta_\Gamma, \phi_\Gamma) = (-9.6, 0.4)$.

However, in some cases, photons with tuneable energy are not available. Fortunately, with prior knowledge of lattice constant and symmetry of the crystalline sample, we can still determine the position of first Γ. In most cases, the FS features around Γ have the highest symmetry. Thus, from the FS mapping, we should be able to narrow down the candidate list of first Γ based on the knowledge of both symmetry and *ab initio* calculation. It is obvious that, among those first Γ candidates, only the real one after the momentum conversion can match the periodicity indicated by the crystal lattice constant. Figure 1.8 presents an example of *1T-PtSe*$_2$ validating the method mentioned above.

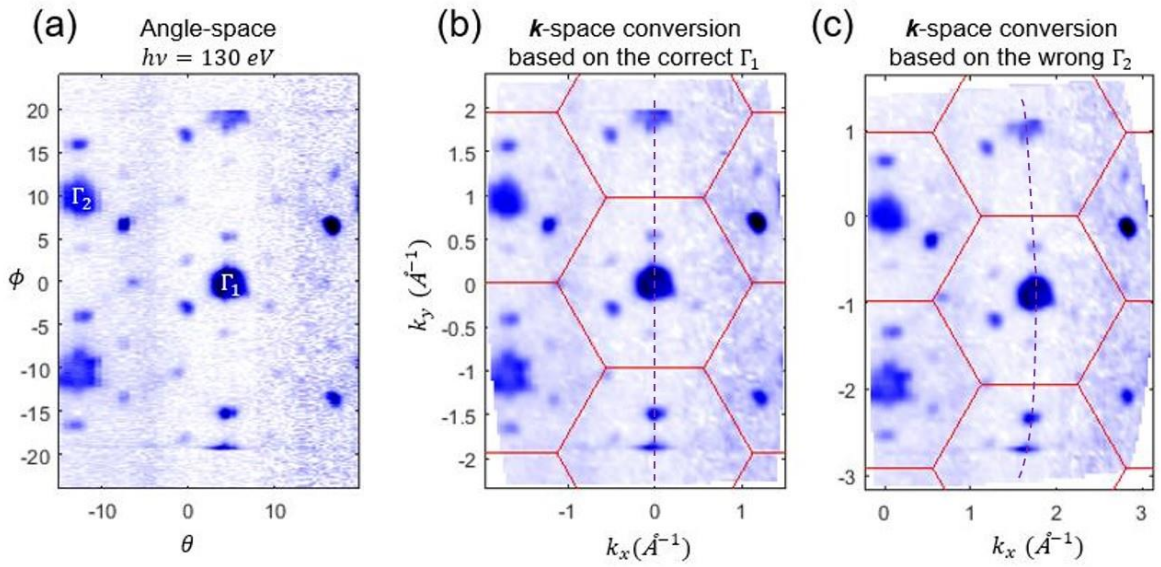


Fig. 1.8 Determination of the first Γ under fixed photon energy. (a) Raw data of FS mapping of *1T-PtSe*$_2$ under photon energy of 130 eV in angle space. (b) Momentum-space conversion based on the correct first Γ at Γ_1 which perfectly matches the Brillouin zone (BZ). (c) Momentum-space conversion based on the wrong first Γ at Γ_2 which shows clear distortion away from the first Γ, as shown by the purple dashed mirror axis.

1.2.2 Photon energy to perpendicular momentum conversion

As we have stated in section 1.1.2 and section 1.1.3, the perpendicular momentum is not conserved in the photoemission process due to the breaking of (discrete) translational symmetry at the interface between the crystal and the vacuum. From the perspective of the three-step model shown in Fig. 1.3(b), step one and two happen inside the crystal bulk while from step two to step three, the photoelectron travels through the crystal surface. Therefore, the crystal momentum is conserved in step one and step two but only the parallel momentum is conserved from step two to step three. To acquire information of perpendicular crystal momentum, one needs to make a connection between the crystal momentum in step two and the momentum of the free electrons in step three under appropriate approximations.

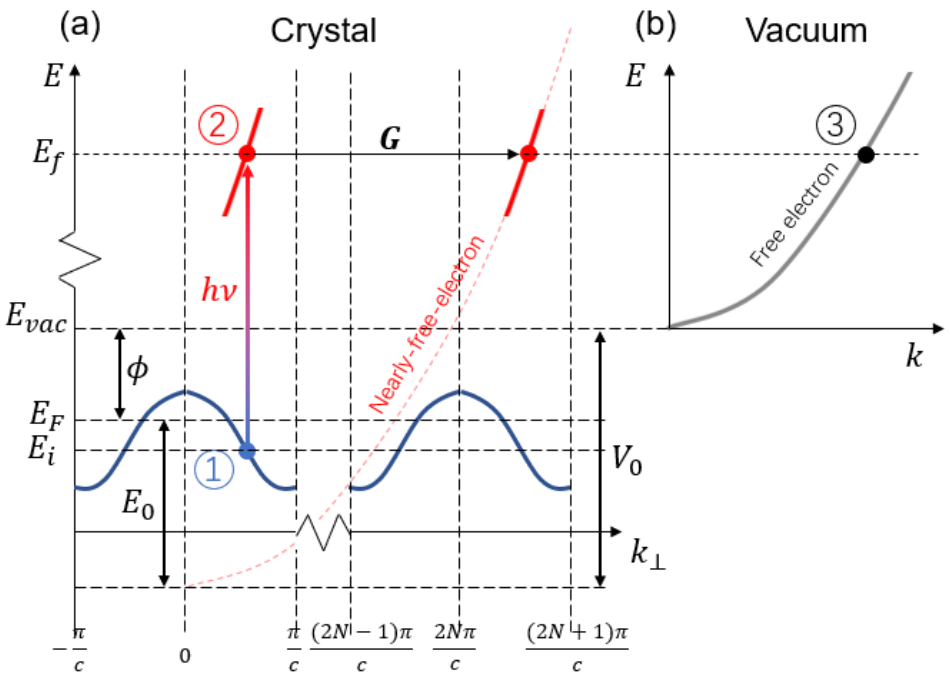


Fig. 1.9 Schematics of the photoemission process within the three-step nearly-free-electron final state model: (a) direct optical transition in the crystal (the reciprocal lattice vector ***G*** supplies the required momentum). The final state can be well fitted by the nearly-free-electron formula. (b) Free-electron final state in the vacuum.

As shown in Fig. 1.9, one commonly used approximation is that one can assume a nearly-free-electron description for the final bulk Bloch state in step two. In this model, the assumption describes the interaction between the electrons and the ion cores using a weak perturbing potential. Although any fine structure of the interaction has been excluded, the validity of this model can be justified in the following reasons: (1) since the state in step two is in the high-energy unoccupied conduction band (CB), and due to the Pauli exclusion principle, they can only feel a weak lattice potential at relatively large distance from the ion core. (2) The interaction is further diminished by the shielding effect from other core electrons. Therefore, in most cases, these unoccupied CB can be well fitted using the nearly-free-electron formula.

The energy dispersion for the final state in the crystal (step two) can be written as

$$E_f^{(2)} = \frac{\hbar^2 \boldsymbol{k}_{crystal}^2}{2m} - E_0 = \frac{\hbar^2 (k_\parallel^2 + k_\perp^2)}{2m} - E_0. \tag{1.16}$$

Equation (1.16) is written using E_F as the energy reference in which m is the electron effective mass and $(-E_0)$ is the crystal field potential that the electron feels. Using the free electron energy in the vacuum as the reference, the energy dispersion for the final state in the vacuum (step three) can be written as

$$E_f^{(3)} = E_{kin} = \frac{\hbar^2 \boldsymbol{k}_{vacuum}^2}{2m}. \tag{1.17}$$

Using the same energy reference and with the help of the conservation law of energy and parallel momentum, we have

$$\begin{aligned} \frac{\hbar^2 (k_\parallel^2 + k_\perp^2)}{2m} - V_0 &= E_{kin}, \\ k_\parallel &= k_{vacuum} \sin\theta. \end{aligned} \tag{1.18}$$

Here $V_0 = E_0 + \phi$ is the inner potential, which corresponds to the energy difference between the vacuum level and the fitted nearly-free-electron dispersion bottom, and θ is

photoelectron emission angle about the surface normal. If V_0 is given, one can obtain the value of the perpendicular momentum by measuring the energy and emitted direction of the photoelectron as

$$k_\perp = \frac{\sqrt{2m(E_{kin}\cos^2\theta + V_0)}}{\hbar}. \tag{1.19}$$

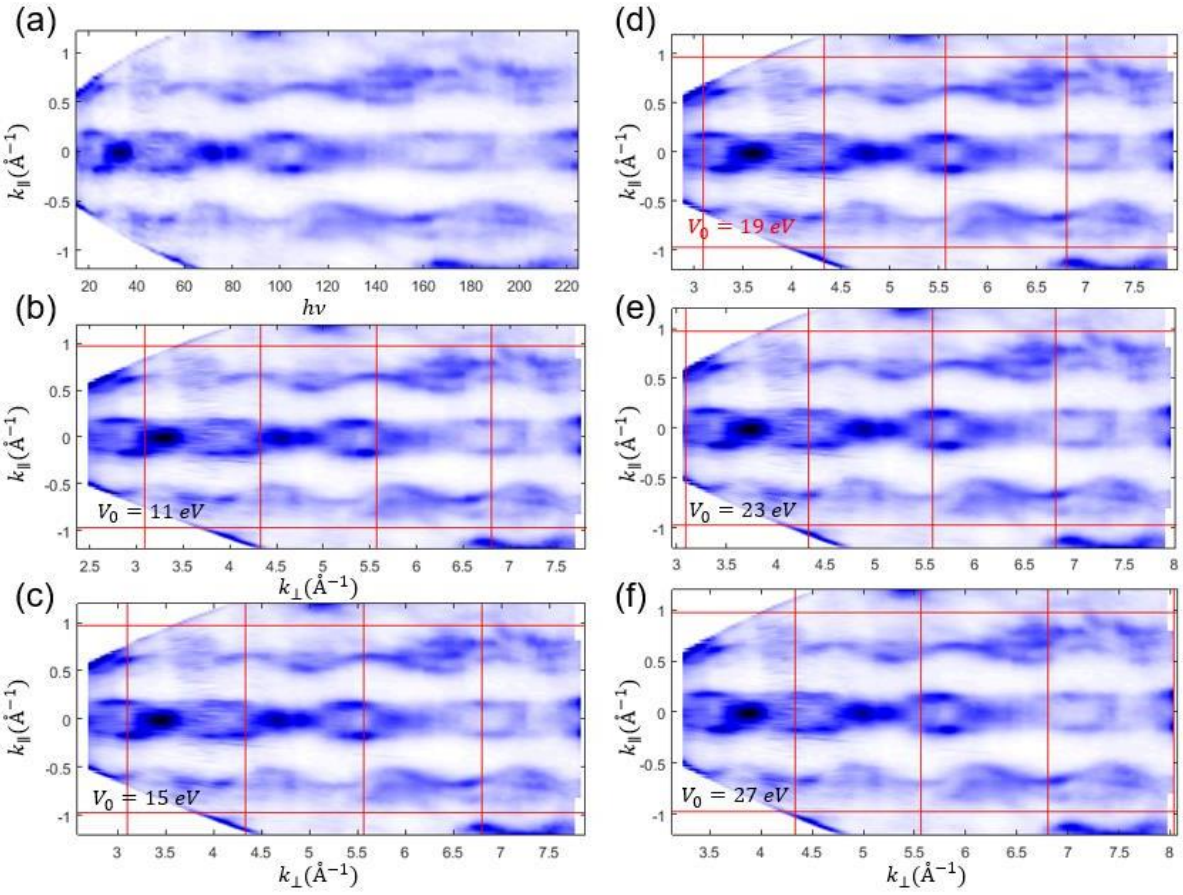


Fig. 1.10 Photon-energy-dependent measurement of *1T-PtSe*$_2$. (a) Photon energy dependent energy contours at $E = E_F - 3.05$ eV. (b-f) Photon energy to k_z conversion using different values of inner potential as $V_0 = 11$ eV (b), 15 eV (c), 19 eV (d), 23 eV (e) and 27 eV (f). The red lines indicate the BZ boundary. The optimal inner potential $V_0 = 19$ eV has the best match with the k_z periodicity.

Consider the simple case of photoelectron emitted perpendicular to the sample surface with the kinetic energy of $E_{kin} = h\nu - \phi$, that is originally from the electron state with the energy at the Fermi level and zero parallel momentum. Thus, by changing the photon energy and measuring the photoemission intensity of $I = I(E_{kin} = h\nu - \phi, \theta = 0)$, one can scan the electron states with varying perpendicular momentum as $\phi = \phi(k_\perp = \frac{\sqrt{2m(E_{kin}+V_0)}}{\hbar}; E_i = E_F, k_\parallel = 0)$.

This observation provides an experimental approach to the determination of the value of V_0. One can infer V_0 from the periodicity of the electronic structure $E(k_\perp)$. As shown in Fig. 1.10, the equal energy contour from the photon-energy-dependent measurement after the momentum conversion can match the k_z periodicity only when the correct V_0 [Fig. 1.10(d)] is applied.

One may notice that, as shown in Fig. 1.10, although $V_0 = 19$ eV has the best overall agreement, there exists some mismatch at low photon energy. By tuning the inner potential, it shows that smaller V_0 works better for high photon energy range [Figs. 1.10(b) and (c)] whereas larger V_0 fits low photon energy range better [Figs. 1.10(e) and (f)]. This is due to the inaccurate assumption that V_0 is a constant independent of energy and momentum. Although the nearly-free-electron model is a sufficiently good approximation of final state in the crystal bulk, we have reasons to believe that for different final states with varying momentum and energy, the fitted nearly-free-electron parameter E_0 varies. In a general picture, final states with higher energy are further away from the core ions, thus "feel" weaker perturbing potential. The inner potential therefore generally decreases with the kinetic energy of photoelectrons. Theoretical and experimental studies on the determination of inner potential have been reported in Ref. [7], and the result of copper is presented in Fig. 1.11, which is consistent with the general idea mentioned above.

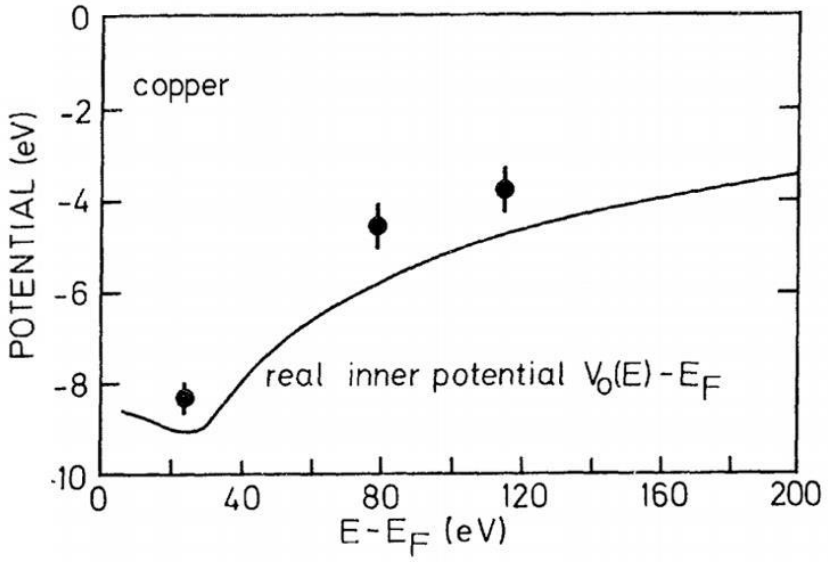


Fig. 1.11 Inner potential of copper V_0 as a function of the electron energy E. $V_0(E)$ is theoretical [8, 9] and three V_0 values are determined from the subthreshold effect. This figure is adapted form Ref. [7]. Please note the definition here is different as $V_0 = -E_0 - \phi$.

1.2.3 Data visualization techniques

In section 1.2.1 and section 1.2.2, we have demonstrated that, under a series of reasonable approximations, the measured ARPES intensity $I = I(\theta, \phi, E_{kin}, h\nu)$ can be mapped to $I = I(k_x, k_y, k_z, E)$. In weak correlated systems, which works for the materials discussed in this thesis, we thus can extract the band structure $E_i = E_i(k_x, k_y, k_z)$ in principle by simply tracking the spectral intensity extrema from $I(k_x, k_y, k_z, E)$.

However, the measured ARPES data are always suffering from both intrinsic and extrinsic broadening, which makes the spectral peak tracking difficult. The intrinsic broadening includes k_z broadening due to the finite photoelectron free path [10], broadening due to sample quality [11] and thermal broadening [12]. The extrinsic broadening originates from the finite experimental resolution. For a certain measurement, the broadening may

mainly come from one or a few mentioned above. For example, limited by the photoelectron mean-free-path, the detected photoelectrons are mainly excited from a very thin slab at the surface ($\Delta z\sim 1$ nm). Thus, as indicated by the Heisenberg's uncertainty principle $\Delta z \Delta k_z \geq 1$, the ultimate intrinsic k_z resolution is $\Delta k_z \sim 0.1 \text{Å}^{-1}$. This broadening can be overcome by using a high photon energy range to increase the kinetic energy of photoelectron, but it is at the cost of parallel momentum and energy resolution.

To sum up, even for weakly correlated systems, multiple broadening effects are still nonnegligible. From a simple perspective, the ARPES spectrum of a non-interacting system can be regarded as a "pure" broadening free spectrum convoluted with a blurring function which contains all the broadening effects

$$\begin{aligned} I(\boldsymbol{k}, E) &= \textstyle\sum_i I_0(\boldsymbol{k}, E_i(\boldsymbol{k})) \otimes R(\boldsymbol{k}, E), \\ I_0\big(\boldsymbol{k}, E_i(\boldsymbol{k})\big) &= \begin{cases} M(\boldsymbol{k}, E), E = E_i(\boldsymbol{k}) \\ 0, E \neq E_i(\boldsymbol{k}) \end{cases}. \end{aligned} \tag{1.20}$$

Here, I_0 is the broadening-free spectrum, R is the blurring function, M is the matrix element and $E_i(\boldsymbol{k})$ is the band dispersion we intend to obtain. Mathematically, if we know the exact form of $R(\boldsymbol{k}, E)$, one can retrack I_0 by deconvolution. However, although the resolution function of the machine is obtainable, since R mixes all the broadening effects, it is practically impossible to develop an accurate form of R. Even if we managed to estimate R under some approximation, it is still challenging to obtain I_0 because deconvolution is mathematically unstable.

Experimentally, there are three commonly used data enhancement techniques to help extract the extrema from the spectra. They are referred to as the second derivative [13], maximum curvature [14] and minimum gradient [15] methods. The basic idea is similar for these three methods: the peak feature in the raw data can be converted to sharper peak

feature after the calculation of local second derivative, curvature and the inverse of the gradient.

Take 2D ARPES data $I = I(\xi, \eta)$ as an example. Here, ξ and η are two variables in the measurement. The data can be a band dispersion when $(\xi, \eta) = (k_{\parallel}, E)$ or an energy contour when $(\xi, \eta) = (k_x, k_y)$. The second derivative can be calculated as

$$I_{2d}(x, y) = A_x \frac{\partial^2 I}{\partial x^2} + A_y \frac{\partial^2 I}{\partial y^2}. \tag{1.21}$$

A_x and A_y are positive parameters originating from different units of I_0, x and y. In the limit where $A_x \gg A_y$ or $A_x \ll A_y$, the 2D second derivative evolves to the 1D case along momentum distribution curves (MDCs) or energy distribution curves (EDCs).

Similarly, the 2D curvature can be calculated as

$$I_c(x, y) \sim \frac{\left[1+C_x\left(\frac{\partial I}{\partial x}\right)^2\right]C_y\frac{\partial^2 I}{\partial y^2} - 2C_xC_y\frac{\partial I}{\partial x}\frac{\partial I}{\partial y}\frac{\partial^2 I}{\partial x \partial y} + \left[1+C_y\left(\frac{\partial I}{\partial y}\right)^2\right]C_x\frac{\partial^2 I}{\partial x^2}}{\left[1+C_x\left(\frac{\partial I}{\partial x}\right)^2+\left(\frac{\partial I}{\partial y}\right)^2\right]^{\frac{3}{2}}}. \tag{1.22}$$

It has two independent positive parameters C_x and C_y, thus has one more degree of freedom than the second derivative method whose only free parameter is A_x/A_y. We can also notice that in the limit where $C_x \ll 1$ and $C_y \ll 1$, the curvature method evolves to the second derivative method as

$$I_c(x, y) \sim C_x \frac{\partial^2 I}{\partial x^2} + C_y \frac{\partial^2 I}{\partial y^2}|_{C_{x,y} \ll 1}. \tag{1.23}$$

Therefore, by tuning the parameters, the curvature method should always have better performance than the second derivative method.

The third method, the minimum gradient method has been recently developed and has proved to be effective for ARPES data on high-temperature superconductors [15]. It can be calculated as

$$I_G(x,y) \sim \frac{I}{\sqrt{G_x\left(\frac{\partial I}{\partial x}\right)^2 + G_y\left(\frac{\partial I}{\partial y}\right)^2}}. \tag{1.24}$$

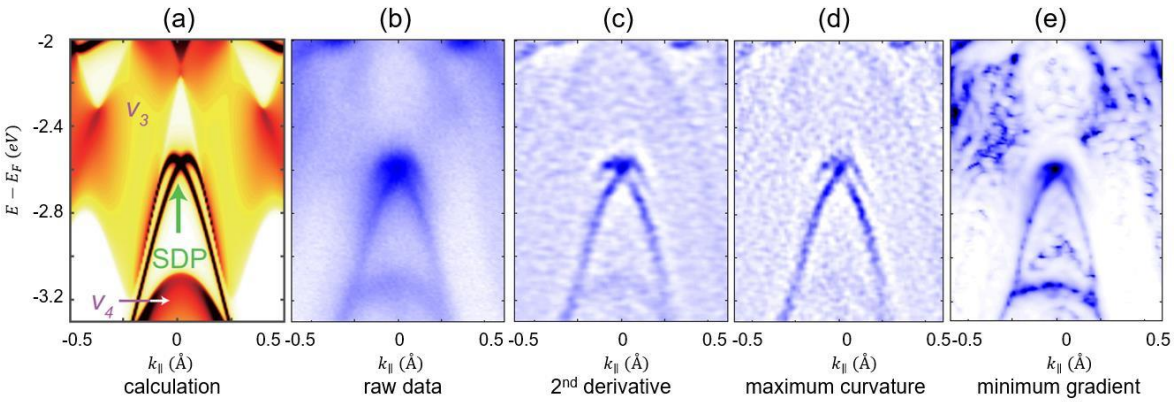


Fig. 1.12 Comparison of three data enhancement methods. (a) *Ab initio* calculation of band structure near the surface Dirac cone of *1T-PtSe*$_2$. (b) Raw ARPES data. (c) Second derivative data. (d) Maximum curvature data. (e) Minimum gradient data.

Figure 1.12 compares these three data enhancement methods on ARPES data of *1T-PtSe*$_2$. All methods make the surface states feature sharper and the result is consistent with corresponding *ab initio* calculation as shown in Fig. 1.12(a). We should emphasize here that these three methods are just tools to distinguish fine band structure, but we need to be careful when they are used for quantitative analysis since they rely on several free parameters and may result in artificial features.

1.2.4 Maximum intensity projection and 3D visualization

With the rapid improvement of the efficiency of experimental data acquisition, modern ARPES often deals with a large volume of data in three or four dimensions (e.g. $I = I(k_x, k_y, k_z, E)$. Therefore, it is important to develop methods which can search for desirable

features from the big data. In this section, we will introduce the maximum intensity projection (MIP) method, which has been widely used in the field of medical imaging [16-18]. We notice that it is also a powerful tool for ARPES data 3D visualization and band gap detection.

Figure. 1.13 illustrates how it works for a simple one-dimension single-band case. MIP, namely, means projecting the maximum value of intensity along a certain direction (here, along EDCs). Assuming the matrix element has a very weak momentum dependence, one should get a constant MIP value for any occupied momentum states as shown in Fig. 1.13(a). Then, consider a gap of 2Δ is formed at $\boldsymbol{k} = \boldsymbol{k_G}$ where the density of states splits into two parts [19, 20], upper half and lower half to two different energy levels. Therefore, the MIP value should drop by 50% accordingly and MIP would leave a dip feature around $\boldsymbol{k_G}$, as shown in Fig. 1.13(b). For real ARPES data, the drop might not reach 50% because of the finite momentum resolution and a noisy background, as shown in Fig. 1.13(c).

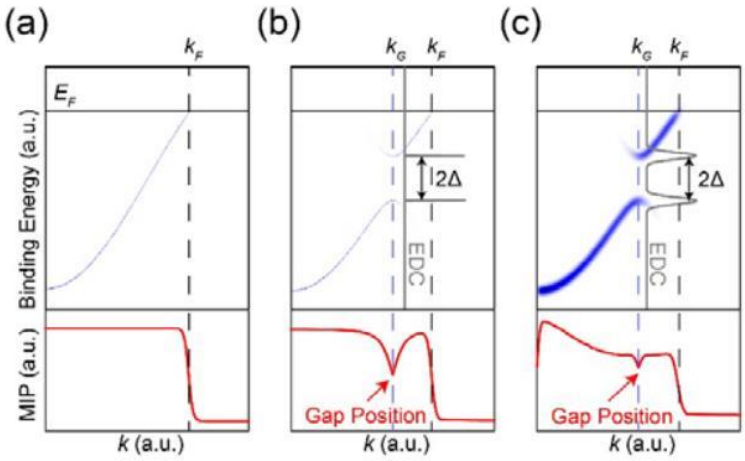


Fig. 1.13 Schematic illustration of the principle of maximum intensity (MIP) for gap detection. (a) Ideal band dispersion (upper) and the corresponding MIP curve (lower). (b) Ideal band dispersion with a band gap opening at $\boldsymbol{k_G}$ with a magnitude of 2Δ (upper) and corresponding MIP curve showing a dip at $\boldsymbol{k_G}$ (lower). Energy distribution curve (EDC) at $\boldsymbol{k_G}$ showing two sharp δ-function peaks from both upper and lower part of the gap. (c) The same band dispersion as (b) but convoluted with arbitrary momentum and energy Lorentzian broadening functions (upper), and corresponding MIP curve (lower) showing a weakened dip at $\boldsymbol{k_G}$. EDC at $\boldsymbol{k_G}$ showing two Lorentzian-shape peaks from both upper and lower part of the gap.

Similar to this simple 1D schematic, it can be easily applied to 3D real ARPES data $I = I(k_x, k_y, E)$ as shown in Fig. 1.14. By applying the MIP method on the low-temperature data of CDW material *2H-TaSe*$_2$, one can observe multiple dip features in Fig. 1.14(b), indicating the gap opening in the momentum space. This observation also show good agreement with the tight-binding simulation as shown in Fig. 1.14(c). The detail of this material will be further discussed in Chapter 3.

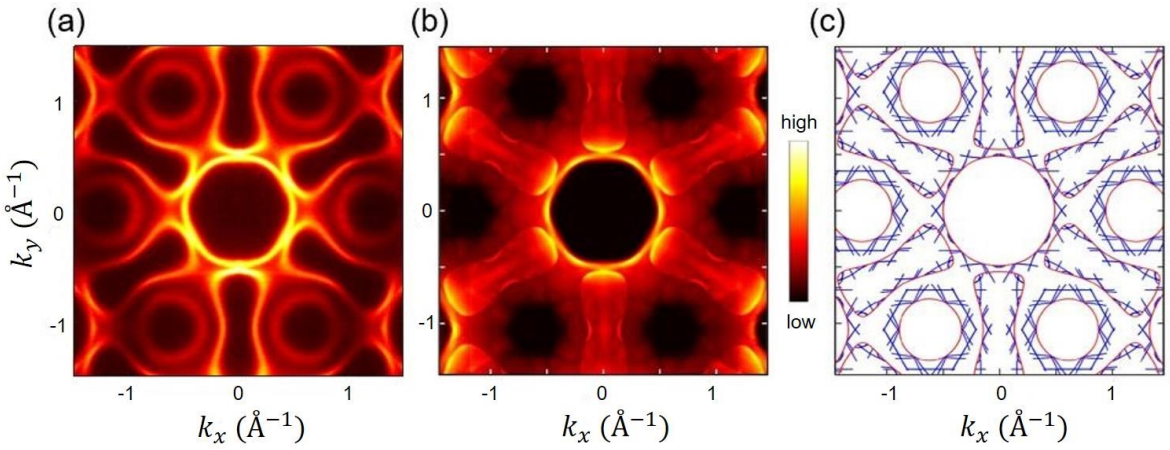


Fig. 1.14 MIP method on *2H-TaSe*$_2$ data. (a) ARPES measured energy contour at E_F in the high-temperature normal phase. (b) MIP of low-temperature ARPES data. The dark features are CDW gap candidates in $k_x - k_y$ space. (c) Illustration of band crossing indicated by tight-binding simulation. The blue lines show the $k_x - k_y$ plane projection of the intersection lines between original main bands (MBs) and CDW folded bands (FBs) in an energy window of 200 meV below E_F. The red curves show the energy contour at E_F of the normal phase.

ARPES data 3D visualization can be realized by applying the MIP method in arbitrary directions (perspectives). Fig. 1.15 shows an example of 3D visualization of ARPES data on the features near *M* point of *2H-TaSe*$_2$ in the low-temperature phase. The gap features can be clearly seen as the transparent part in the 3D visualization.

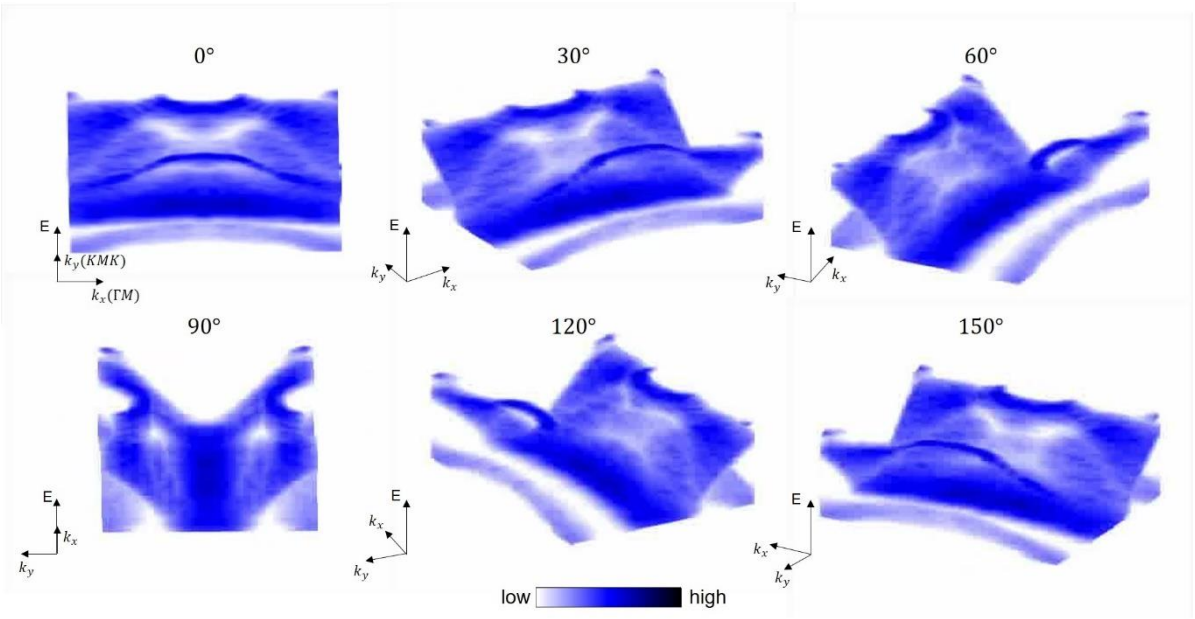


Fig. 1.15 3D visualization of ARPES data on the band structure near M point of *2H-TaSe*$_2$ in the low-temperature phase from different perspectives.

1.3 Facilities: synchrotron-based ARPES

The ARPES data presented in the thesis are collected from I05 branch of Diamond Light Source (DLS), UK and Spectromicroscopy branch of Elettra, Italy. They are synchrotron-based ARPES facilities. Compared with lab-based ARPES, such as laser-ARPES and Helium-lamp-ARPES, synchrotron light source has a wider range of tuneable photon energy and much higher light brilliance. In this section, a brief introduction of these two facilities containing key parameters is presented.

1.3.1 I05 branch at DLS

Diamond Light Source (DLS) is the UK's national synchrotron, half a kilometre in circumference as shown in Fig. 1.16(a). It is designed to produce very intense beams of X-

rays, infrared and ultraviolet light. Synchrotron light can be 10 billion times brighter than the sun. Electrons are accelerated through the linear accelerator (Linac) and booster synchrotron to nearly the speed of light before they enter the storage ring, as shown in Fig. 1.16(b). The bending magnets and insertion devices including undulators inside the ring change the electron path dramatically and thus cause the emission of intensive synchrotron light. This light can then be channeled out of the storage ring and into the experimental stations, called beamline. I05 branch is one of the beamlines at DLS which is dedicated to the study of electronic structure by ARPES.



Fig. 1.16 Diamond Light Source (DLS), Harwell Campus, UK. (a) Overlooking view of DLS. (b) Schematic of DLS including electron gun, linear accelerator (Linac), booster synchrotron storage ring and beamlines. The figure is adapted from Ref. [21].

As illustrated in Fig. 1.17, X-ray radiation is generated by a 5m-long APPLE-II undulator and then passes through an optical system including monochromator and focusing mirrors. The beamline consists of two branches: one high-resolution ARPES with high beam flux and one nano-ARPES equipped with Fresnel zone plate (FZP).

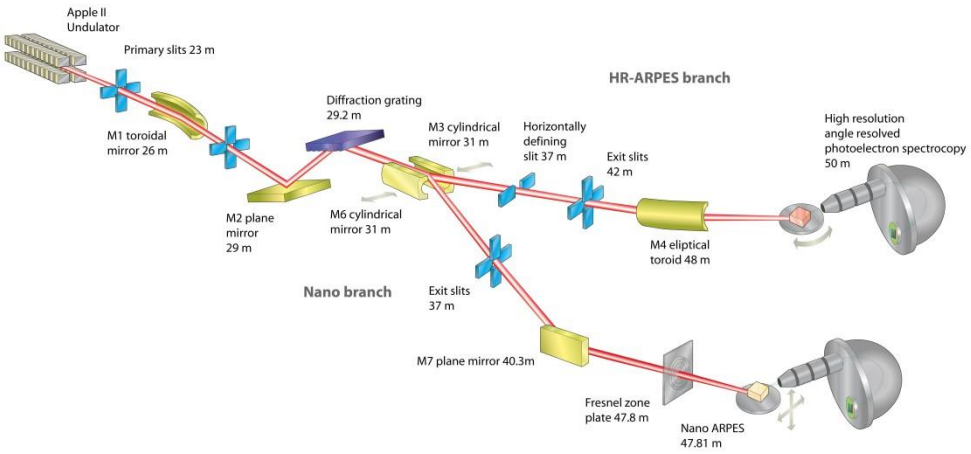


Fig. 1.17 Sketch of the optical system of Beamline I05 at DLS. It consists of two branches: high-resolution ARPES and nano-ARPES. This figure is adapted from Ref. [22].

The high-resolution branch (HR-ARPES) delivers a high flux of beam in a spot size of 50×50 μm^2. The energy resolution allows efficient data acquiring at 5-10 meV resolution in the core operation range of 18-80 eV. Higher photon energies, up to 240 eV, can be used for broad Fermi surface mapping. The ARPES end station is equipped with a cryogenic six-degree-of-freedom sample manipulator covering all emission angles in the temperature range 7 K$<T<$300 K, and housed in an ultrahigh vacuum of 5×10^{-11} mbar. The system is equipped with a hemispherical electron analyzer (model R4000, VG Scienta) and the angular resolution is below 0.2° [23].

The nano-ARPES branch delivers a FZP focused ultra-small spot with a size about 0.7×0.7 μm^2. The photon energy range for nano-ARPES is 60-95 eV. The sample can be cooled down to 10 K. Flexible adjustment of photoemission direction is possible with two-axes sample goniometer, rotation of analyser as well as deflection mode of the analyser (model DA30, VG Scienta) [23].

1.3.2 Spectromicroscopy branch at Elettra

Similar to DLS, Elettra is an Italian third-generation synchrotron radiation facility located on the outskirts of Trieste, as shown in Fig. 1.18(a). It has been serving the national and international scientific and industrial community since 1993 and has been completely revised and upgraded in 2009. Currently, 28 beamlines utilize the radiation generated by the Elettra source, as shown in Fig. 1.18(b). Spectromicroscopy branch is one of them.

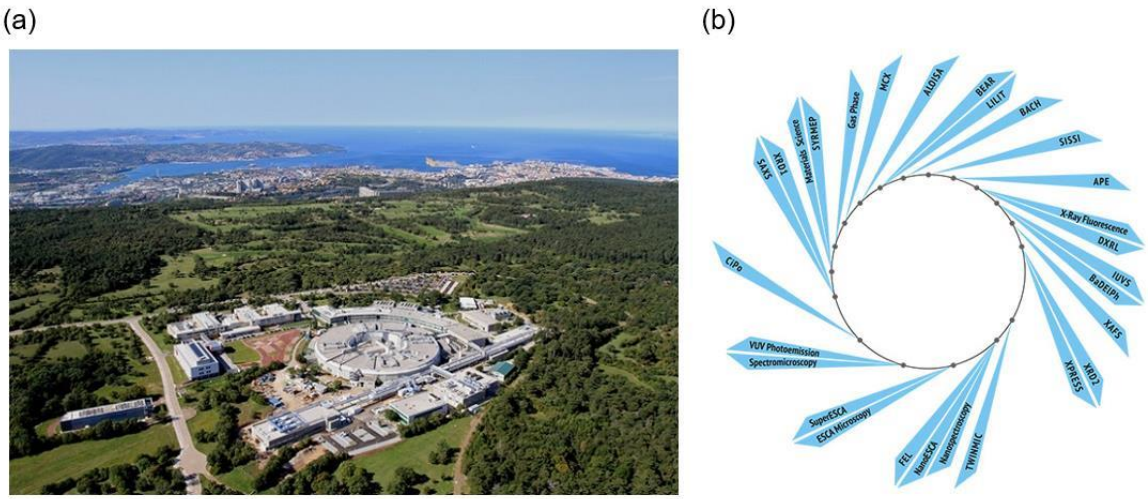


Fig. 1.18 Elettra synchrotron, Trieste, Italy. (a) Overlooking view of Elettra synchrotron. (b) 28 beamlines utilize the radiation generated by the Elettra source. This figure is adapted from Ref. [24].

As illustrated in Fig. 1.19, in contrast to nano-ARPES at DLS, Spectromicroscopy branch use Schwarzschild objectives (SO) instead of FZP to focus the beam spot down to a size of $0.8\times0.8\ \mu m^2$. The beamline is performed using two fixed photon energies of 27 and 74 eV. The ARPES is performed with energy and angular resolutions down to 14 meV and 0.15° by means of internal movable electron energy analyzer mounted on precise two axes goniometer setup. The sample can be measured at 15-470 K in an ultrahigh vacuum of

1×10^{-10} mbar. The sample focusing and real-space imaging is stable thanks to the XYZR sample scanning stage [25]. The Fermi surface mapping is achieved using a homemade analyzer inside the measuring chamber which can scan along both polar and tilt directions.

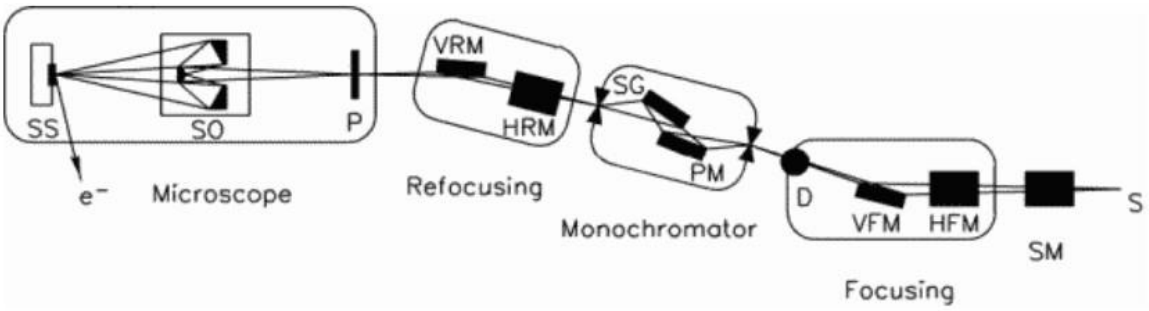


Fig. 1.19 Sketch of the optical system of Beamline Spectromicroscopy. The system consists of focusing optical, monochromator, refocusing optical and microscope optical. The core focusing elements are the Schwarzschild objectives (SO). SM: spherical mirror. HFM: horizontal focusing mirror. VFM: vertical focusing mirror. PM: plane mirror. SG: spherical grating. HRM: horizontal refocusing mirror. VRM: vertical refocusing mirror. P: pinhole. SO: Schwarzschild objectives. SS: sample stage. This figure is adapted from Ref. [26].

References

[1] H. Hertz: Uber einen Einfluss des ultravioletten Lichtes auf die elektrische Entladung (On the influence of ultraviolet light on the electric discharge). *Ann. Physik* **31**, 983 (1887); for a very good review on the history of photoemission see: H.P. Bartel, Ch. Kleint: *Prog. Surf. Sci.* **49** (1995) 107.

[2] A. Einstein: *Ann. Physik* **17** (1905) 132.

[3] Hüfner S. Photoelectron spectroscopy: principles and applications. *Springer Science & Business Media*, 2013.

[4] Y. Chen, Studies on the electronic structures of three-dimensional topological insulators by angle resolved photoemission spectroscopy, *Frontiers of Physics*, **7** (2012) 175.

[5] Chen, C. (2018). Electronic structures of novel quantum materials studied by spatially angle-resolved photoemission spectroscopy (*Doctoral dissertation*, University of Oxford).

[6] Liu C. Electronic structure of iron arsenic high-temperature superconductors studied by angle-resolved photoemission spectroscopy (ARPES). (*Doctoral dissertation*, Iowa State University, 2011.

[7] S.A. Lindgren, L. Wallden, J. Rundgren, P. Westrin, Low-energy electron-diffraction from Cu (111) - subthreshold effect and energy-dependent inner potential - surface relaxation and metric distances between spectra, *Physical Review B*, **29** (1984) 576.

[8] L. Hedin, Lundqvis. Bi, Explicit local exchange-correlation potentials, *Journal of Physics Part C Solid State Physics*, **4** (1971) 2064.

[9] J. Neve, P. Westrin, J. Rundgren, On the choice of local exchange-correlation potential for leed application to Cu (111), *Journal of Physics C-Solid State Physics*, **16** (1983) 1291.

[10] V.N. Strocov, Intrinsic accuracy in 3-dimensional photoemission band mapping, *Journal of Electron Spectroscopy and Related Phenomena*, **130** (2003) 65.

[11] Z.K. Liu, Y.L. Chen, J.G. Analytis, S.K. Mo, D.H. Lu, R.G. Moore, I.R. Fisher, Z. Hussain, Z.X. Shen, Robust topological surface state against direct surface contamination, *Physica E-Low-Dimensional Systems & Nanostructures*, **44** (2012) 891.

[12] J.A.R. Samson, Line broadening in photoelectron spectroscopy, *Review of Scientific Instruments*, **40** (1969) 1174.

[13] T. Sato, T. Kamiyama, T. Takahashi, K. Kurahashi, K. Yamada, Observation of $d_{x^2-y^2}$-like superconducting gap in an electron-doped high-temperature superconductor, *Science*, **291** (2001) 1517.

[14] P. Zhang, P. Richard, T. Qian, Y.M. Xu, X. Dai, H. Ding, A precise method for visualizing dispersive features in image plots, *Review of Scientific Instruments*, **82** (2011) 043712.

[15] Y. He, Y. Wang, Z.X. Shen, Visualizing dispersive features in 2D image via minimum gradient method, *Review of Scientific Instruments*, **88** (2017) 073903.

[16] M.P. Marks, S. Napel, J.E. Jordan, D.R. Enzmann, Diagnosis of carotid-artery disease - preliminary experience with maximum-intensity-projection spiral CT angiography, *American Journal of Roentgenology*, **160** (1993) 1267.

[17] S. Napel, M.P. Marks, G.D. Rubin, M.D. Dake, C.H. McDonnell, S.M. Song, D.R. Enzmann, R.B. Jeffrey, CT angiography with spiral CT and maximum intensity projection, *Radiology*, **185** (1992) 607.

[18] C.M. Anderson, D. Saloner, J.S. Tsuruda, L.G. Shapeero, R.E. Lee, Artifacts in maximum-intensity-projection display of MR angiograms, *American Journal of Roentgenology*, **154** (1990) 623.

[19] K. Rossnagel, On the origin of charge-density waves in select layered transition-metal dichalcogenides, *Journal of Physics: Condensed Matter*, **23** (2011) 213001.

[20] Y.W. Li, J. Jiang, H.F. Yang, D. Prabhakaran, Z.K. Liu, L.X. Yang, Y.L. Chen, Folded superstructure and degeneracy-enhanced band gap in the weak-coupling charge density wave system *2H-$TaSe_2$*, *Physical Review B*, **97** (2018) 115118.

[21] How Diamond Works. www.diamond.ac.uk/Home/About/How-Diamond-Works.

[22] M. Hoesch, T.K. Kim, P. Dudin, H. Wang, S. Scott, P. Harris, S. Patel, M. Matthews, D. Hawkins, S.G. Alcock, T. Richter, J.J. Mudd, M. Basham, L. Pratt, P. Leicester, E.C. Longhi, A. Tamai, F. Baumberger, A facility for the analysis of the electronic structures of solids and their surfaces by synchrotron radiation photoelectron spectroscopy, *Review of Scientific Instruments*, **88** (2017) 013106.

[23] Diamond Light Source I05 endstation: https://www.diamond.ac.uk/Instruments/Structures-and-Surfaces/I05.html

[24] Beamlines at Elettra. https://www.elettra.trieste.it/lightsources/elettra/beamlines.html.

[25] Spectromicroscopy endstation of Elettra. Beamline description: https://www.elettra.trieste.it/lightsources/elettra/elettra-beamlines/spectro-microscopy/beamline.html.

[26] Monochromator and beamline optics:
https://www.elettra.trieste.it/lightsources/elettra/elettra-beamlines/spectro-microscopy/beamline.

Chapter 2

Overview of Transition Metal Dichalcogenides

Transition metal dichalcogenides (TMDs) are a large family of materials with a long and fruitful research history [1-4]. With a variety of chemical elements and crystal structures, different TMD compounds can exhibit their unique properties ranging from charge density waves (CDWs) to superconductive and topological phases. Furthermore, very recently, with the discovery of graphene and the great attention on 2D materials, TMDs stand out for their flexible crystal and electronic structure with tuneable gap size [2, 3].

In this section, we will give a brief overview of TMDs which covers their crystal and electronic structures, and exotic properties. Since it is an enormous scope of the topic, we will only focus on the part which is related to the compounds studied and elaborate further in the remainder of the thesis (Chapter 3-5 on *2H-$TaSe_2$*, *1T-$PtSe_2$* and *2M-WS_2*, respectively).

2.1 Crystal Structure

Transition metal dichalcogenides (TMDs) have a common chemical formula, MX_2. *M* stands for a transition metal element, e.g. *Ta*, *Pt* and *W*. *X* stands for a chalcogen element, i.e. *S*, *Se* and *Te*. Most of TMDs crystallize in a graphite-like layered structure which makes them easily be thinned down to atomic thin film by mechanical exfoliation. Although TMDs have various crystal structures, they have two common types of building blocks characterized by the *H* and *T* structure.

H and *T* phases are illustrated in Fig. 2.1. The building block has a three-atom-layer sandwich structure (chalcogen-metal-chalcogen). In the *H* structure, the transition metal atoms are trigonal prismatic coordinated by chalcogen atoms, whereas in the *T* structure, the coordination is octahedral.

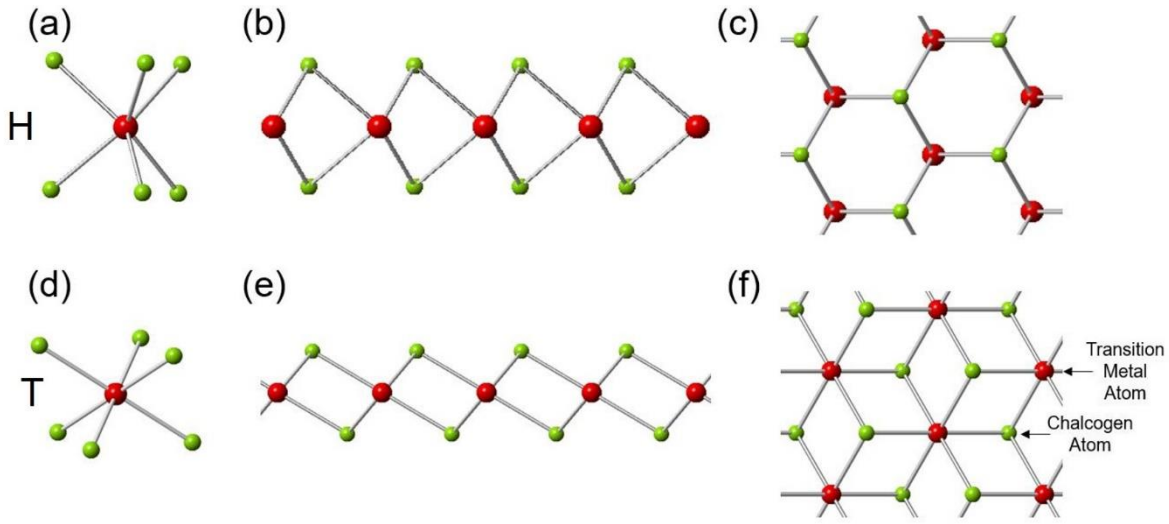


Fig. 2.1 *H* and *T* structure of TMDs. (a) The building block of *H* structure. (b) Side view of *H* structure. (c) Top view of *H* structure. (d) The building block of *T* structure. (e) Side view of *T* structure. (f) Top view of *T* structure.

In some materials, such as WTe_2 and $MoTe_2$, the *T* structure is not thermally stable, and it undergoes 2×1 Peierls distortion at low temperature. The *T* structure is then transformed into the *T'* structure as shown in Fig. 2.2.

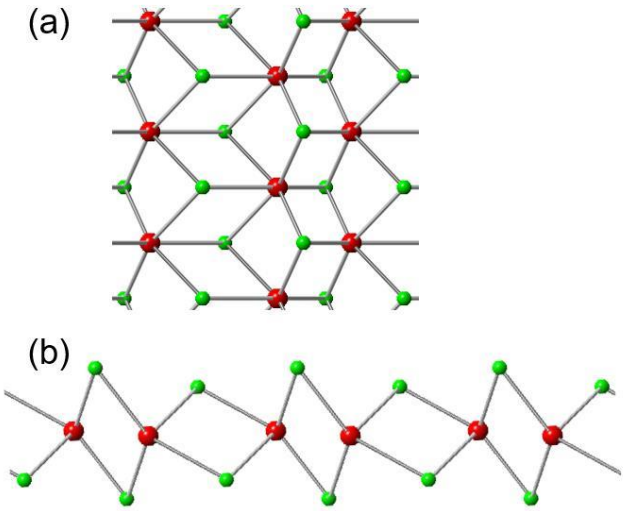


Fig. 2.2 *T'* structure of TMDs. (a) Top view. (b) Side view.

The above *H*, *T* and *T'* building blocks are the basic structure of a single layer of TMDs. The variation in the stacking geometry of neighbouring layers further increases the diversity of bulk crystal structures. Fig. 2.3 presents several examples: different stacking orders of *H* structure can result in *2H* or *3R* phase [see Figs. 2.3(a) and (b)], whereas T_d and *2M* phase consists of *T'* single layer structure [see Figs. 2.3(c) and (d)].

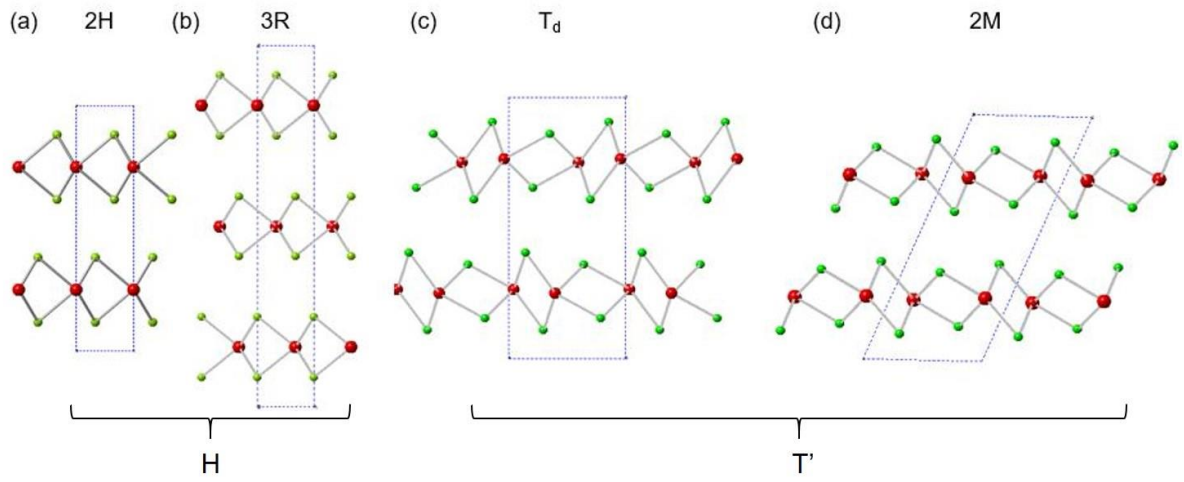


Fig. 2.3 Bulk TMD crystal structure based on different stacking geometry. Side view of *2H* (a), *3R* (b), T_d (c), and *2M* (d) structure. In *2H* and *3R* structure, the monolayer has the *H* structure, whereas in the T_d and *2M* structure, the monolayer is of *T'* type.

In the rest of this section, we will elaborate on three typical crystal structures which are *2H* for $TaSe_2$ (Chapter 3), *1T* for $PtSe_2$ (Chapter 4) and *2M* for WS_2 (Chapter 5).

2.1.1 *2H* structure

The *2H* structure is commonly seen in group V and VI TMDs (e.g. *2H*-$TaSe_2$ and *2H*-MoS_2). The term "*2H*" means that its unit cell contains two layers of *H*-type building blocks. As shown in Figs. 2.3(a) and 2.4(a), *2H*-MX_2 has inversion symmetry with oppositely oriented upper and lower layers, although it lacks an inversion centre for each layer. *2H*-MX_2 is in space group $P6_3/mmc$ (194) which belongs to the hexagonal crystal class, and one can find the complete list of symmetry operations in Ref. [5].

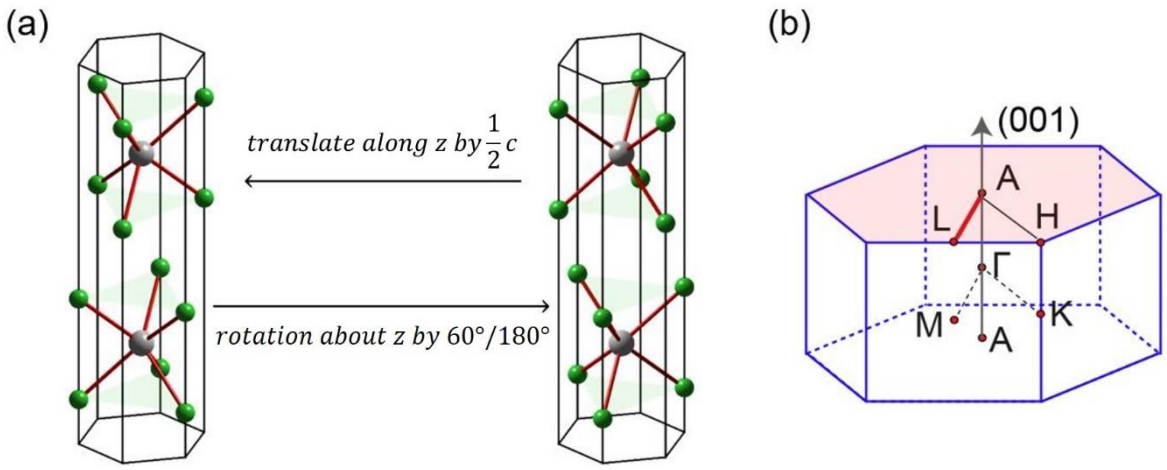


Fig. 2.4 Non-symmorphic symmetry of *2H-MX*$_2$. (a) The six-/two-fold screw symmetry of *2H-MX*$_2$. (b) The BZ of *2H-MX*$_2$. The red $A-L-H$ plane hosts the non-symmorphic symmetry protected four-fold degeneracy in the non-SOC case, whereas the degeneracy is only preserved along $A-L$, as indicated by the red line, in the SOC case.

This space group is non-symmorphic with symmetry operations that shift the origin point by a fraction of the unit cell. The non-symmorphic operation related is a six-/two-fold screw symmetry as shown in Fig. 2.4. Recently, the non-symmorphic symmetry has attracted intensive interest since it can protect the degeneracy of electronic states described in reciprocal space [6-9]. In this case, the screw symmetry leads to four-fold degeneracy in the $A-L-H$ plane in the non-spin-orbital-coupling (non-SOC) systems or $A-L$ in the systems with nonnegligible SOC (See Appendix A). The nodal-line feature in the *2H-TaSe*$_2$ will be further discussed in Chapter 3.

2.1.2 *1T* structure

Group IV, VII and X TMDs usually crystallize in the *1T* phase, such as *1T-TiSe*$_2$, *1T-ReS*$_2$ and *1T-PtSe*$_2$. The term "*1T*" means that its unit cell contains one layer of *T*-type building block. As shown in Figs. 2.1(d)-(f) and Fig. 2.5, *1T-MX*$_2$ has inversion symmetry. It is in group *P*-3*m*1 (164) which belongs to the trigonal crystal class, and one can find the complete list of symmetry operations in Ref. [5].

Figure 2.5 presents the symmetry operation elements of *1T-MX*$_2$. The point group of *P*-3*m*1 is D_{3d}, which includes the centre of inversion and a C_{3v} axis. The C_{3v} axis is along *c* which is a three-fold rotation axis with 3 mirror planes parallel to it [see Fig. 2.5(b)]. The inversion symmetry provides 3 additional two-fold rotation axes perpendicular to the C_{3v} axis, as shown in Fig. 2.5(c). We will further mention that C_{3v} coexisted with time-reversal and inversion symmetries protect the type-II Dirac point in the *1T-PtSe*$_2$ family in Chapter 4.

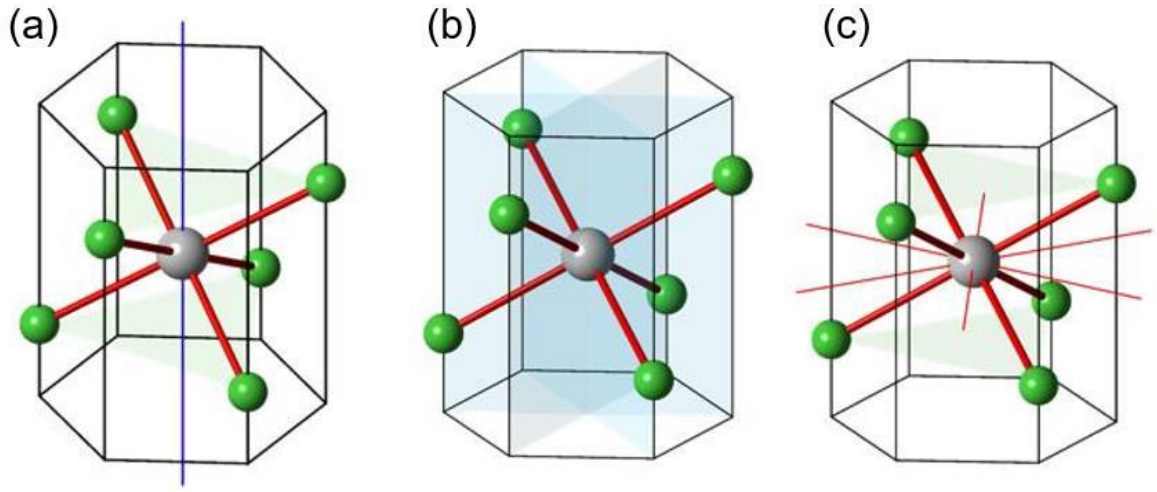


Fig. 2.5 Symmetry operation elements of *1T-MX*$_2$. (a) The blue line shows the three-fold rotation axis. (b) The three light blue planes are the three mirror planes parallel to the three-fold rotation axis. (c) The three red lines indicate the three two-fold rotation axes perpendicular to the three-fold rotation axis.

2.1.3 *2M* structure

2M is a unique phase of WS_2. The common *2H*-WS_2 is semiconducting while *2M*-WS_2 is a topological superconductor (TSC) candidate [10] which will be further discussed in Chapter 5. The single layer of *2M*-WS_2 is of *T'*-type as shown in Fig. 2.3(d). In the term "*2M*", "2" means that its unit cell contains two layers of *T'*-type structure and "*M*" means that it is monoclinic. *2M*-WS_2 crystallizes in the space group $C_{2/m}$ (12) in which the inversion symmetry is preserved, in contrast to the non-centrosymmetric T_d phase. One can find a complete list of symmetry operations in Ref. [5].

Since WS_2 may crystallize in multiple phases including *2H*, *1T'* and *2M*, even in a single flake of sample. It is not trivial to spatially distinguish different phases from the crystal structure perspective. Surface experimental technique such as STM can only distinguish the *2H* phase from *1T'* and *2M* phase, as *1T'* and *2M* share the same single layer structure, they have an identical surface atomic arrangement. Raman spectroscopy is a suitable technique which shows characteristic peaks of the low-symmetry *2M*-phase with micron spatial resolution. Figure 2.6 shows the characteristic results of STM and Raman measurement on the *2M*-WS_2 single crystal.

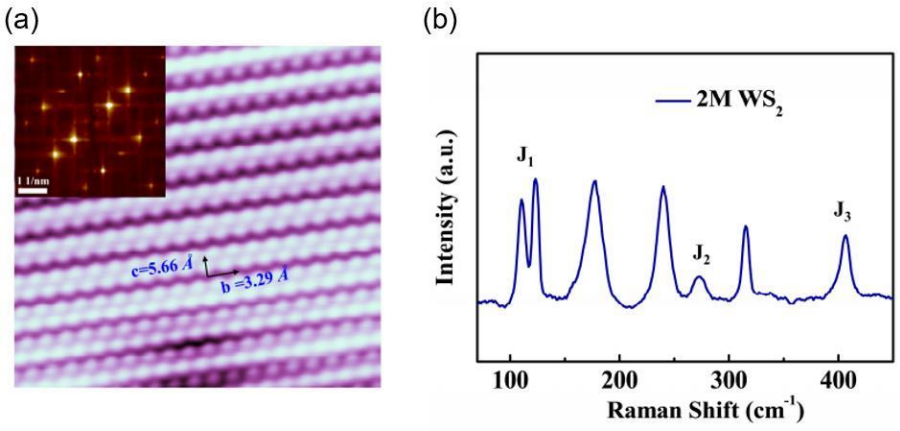


Fig. 2.6 Characteristic results of STM (a) **and Raman measurement** (b) **on the *2M*-WS_2 single crystal.** The figure is adapted from Ref. [10].

2.2 Electronic Structure

Transition metal dichalcogenides (TMDs) have attracted intensive research interest as an alternative 2D material family over graphene with tuneable electronic structure. As a large family of materials with over 40 members, the electronic structure of TMDs depends on a variety of factors. In this section, we present three factors, from the most dominating one which determines the general band structure to the minor one which determines the fine structure. In section 2.1.1, ***d***-orbit filling of the transition metal element is discussed with the comparison of TMDs from different groups. In section 2.1.2, the band structures of *1T* and *2H* crystal structure are compared. In section 2.1.3, spin-orbit coupling (SOC) is discussed with the comparison of TMDs from the same group but different periods.

2.2.1 *d*-orbit filling of the transition metal element

From the crystal structure as shown in Fig. 2.1, in both *T* and *H* structure, each metal atom of TMDs provides four electrons to fill the bonding states with chalcogen atoms such that the oxidation states of the metal and chalcogen atoms are +4 and -2, respectively. Therefore, the electronic structure of TMDs strongly depends on the ***d***-orbit filling of the transition metal element [2, 3].

Since the non-bonding ***d*** electrons are energetically located near the Fermi level, and from the basic band structure theory, each band can occupy two electrons, TMDs with an odd number of non-bonding ***d*** electrons have half-filled bands whereas an even number of non-bonding ***d*** electrons leads to a completely filled case. Therefore, group V TMDs (featuring $\boldsymbol{d^1}$ transition metal centres) are metallic with large Fermi surfaces, whereas group IV ($\boldsymbol{d^0}$), VI

(d^2) and X (d^6) TMDs are primarily semiconducting, or in some special cases semi-metallic with very small Fermi surfaces if the energy gap is negative (e.g. group IV *1T-$TiSe_2$*).

Figure 2.7 compares the calculated band structure from four typical TMDs from group IV, V, VI and X which substantiate the argument above. The double band near the Fermi level in *2H-$TaSe_2$* [Fig. 2.7(b)] and *2H-WSe_2* [Fig. 2.7(c)] are due to the bilayer splitting. These calculations are preliminary and might be inaccurate in details of the fine structure, however, they are sufficient to show the electronic structure evolution depends on the ***d***-orbit filling of the transition metal atoms.

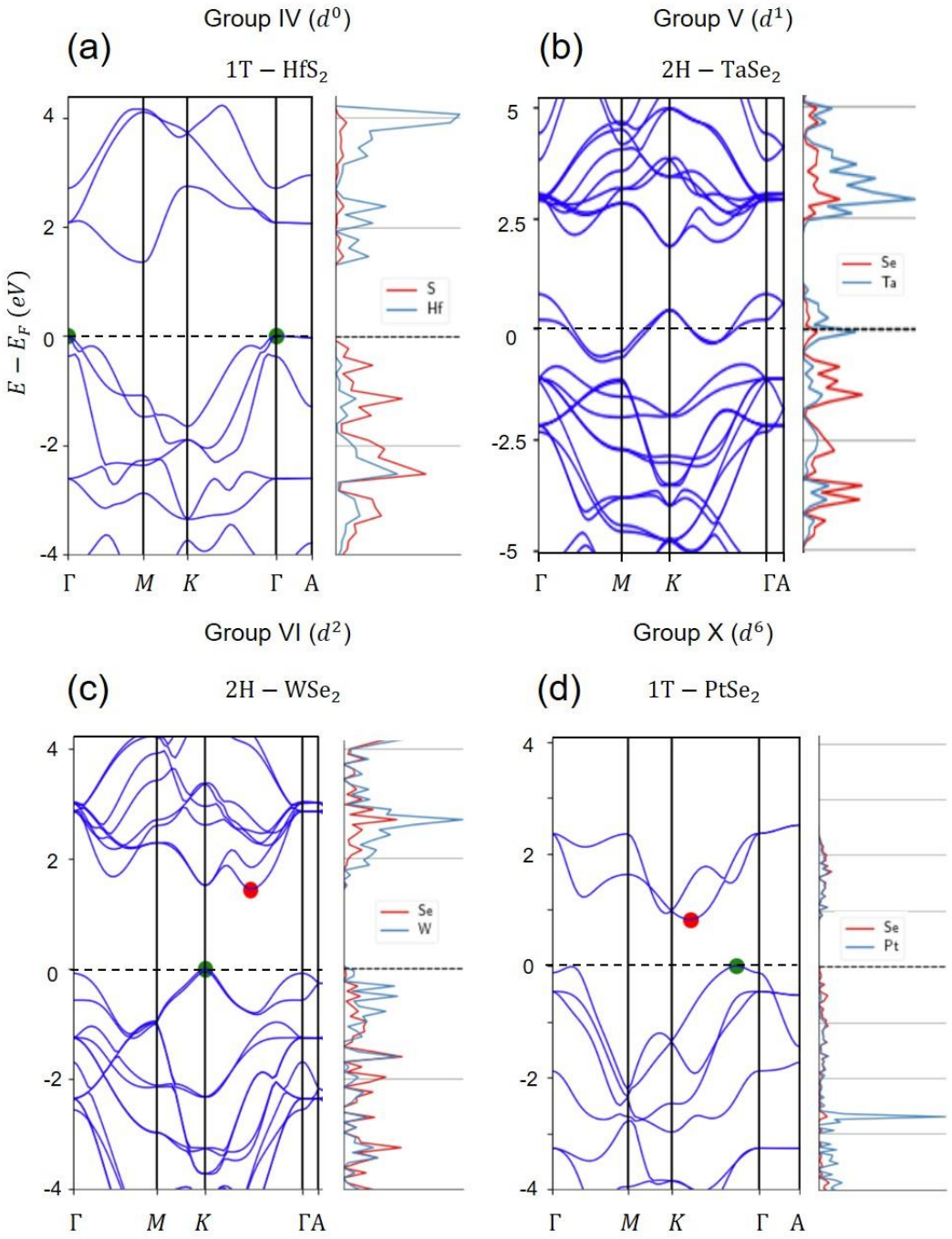


Fig. 2.7 Electronic structure dependence on the *d*-orbit filling of transition metal atoms. *Ab initio* calculated band dispersion of selected TMDs along $\Gamma - M - K - \Gamma$ (left) and density of states (DOS) (right) from group IV *1T-HfS_2* (a), group V *2H-$TaSe_2$* (b), group VI *2H-WSe_2* (c) and group X *1T-$PtSe_2$* (d). All the calculations are extracted from Ref. [11].

2.2.2 Coordination environment of the transition metal

The crystal field also has a dramatic influence on the electronic structure of TMDs. This topic is complicated and varies for specific cases. For example, group VI *2H-$MoTe_2$* and *2H-WS_2* are semiconductors with sizeable energy gap, however, *T_d-$MoTe_2$* is a type-II Weyl semimetal [12] and *2M-WS_2* is a TSC candidate [10]. Furthermore, the crystal field might also have a significant impact on the ***p***-orbit of the chalcogen atoms as well as the ***d***-orbit of the transition metal atoms, especially for the group X TMDs. We will not cover all aspects of this topic which requires careful group theory analysis for different cases, one can find a detailed discussion in Ref. [13]. In this section, we will provide a general picture by a comparison of the electronic structure of *1T* and *2H* structure *TaS_2*. *1T* crystal field effect on the electronic structure will be discussed in detail in Chapter 4 and the comparison of band structures between *2H*- and *2M-WS_2* will be elaborated in Chapter 5.

Figure 2.8 shows the band structure of (a) *1T*- and (b) *2H-TaS_2*. As shown in the schematics, the non-bonding ***d*** electrons of the transition metal are located within the gap between the bonding (***σ***) and antibonding (***σ****) bands of *M-X* bonds. In the *1T* case, the trigonal crystal field split the non-bonding ***d***-orbit into two groups, $d_{z^2,x^2-y^2,xy}$ and $d_{yz,xz}$. Since the transition metal centre has the $\boldsymbol{d^1}$ configuration, the lower group is partially filled [3, 14]. In contrast, in the *2H* case, they are divided to three groups, d_{z^2}, d_{xy,x^2-y^2} and $d_{xz,yz}$. The first group consisting of two bands is about 1 eV below the other two [3, 15], and thus half-filled by the $\boldsymbol{d^1}$ metal centre. Please note, for simplicity purpose, the orbital components shown here are from electron states near Γ. The orbital projection for the whole momentum space is complicated and one can find discussions in Ref. [15].

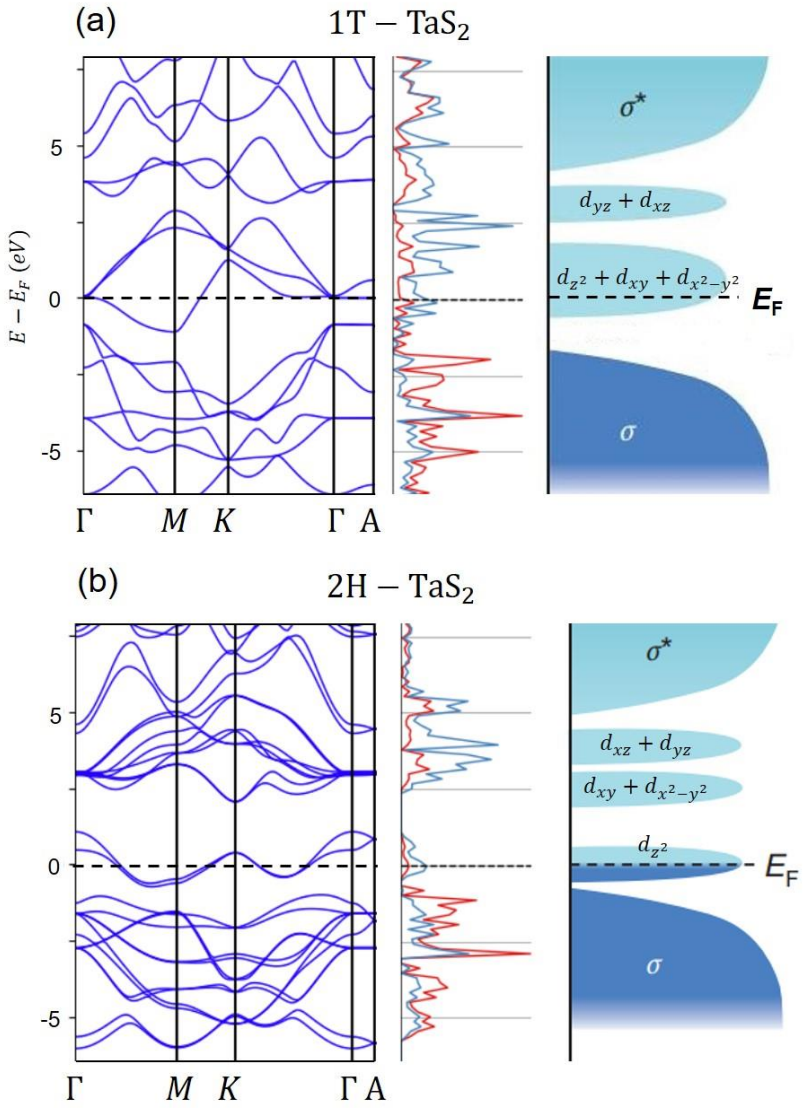


Fig. 2.8 Electronic structure dependence on the coordination environment of the transition metal. Comparison of electronic structure between *1T-TaS*$_2$ (a) and *2H-TaS*$_2$ (b). *Ab initio* calculated band dispersions and DOS are extracted from Ref. [11]. The schematics of the crystal-field diagram are adapted from Ref. [3].

2.2.3 Spin-orbit coupling

Compared to the ***d***-orbit filling and the coordination environment of the transition metal, the effect of spin-orbit coupling (SOC) on the electronic structure is minor and can only be

observable in the fine structure. Therefore, TMDs within the same group and crystal structure have similar electronic structure, however, a trend of enhanced SOC effect with a heavier element can still be observed.

Figure 2.9 compares 4 types of MX_2 monolayer systems in the same group with the same H crystal structure with and without the inclusion of the SOC. We can clearly see that the results without SOC show high similarity for these four compounds. In contrast, the SOC has very little effect on the lightest compound MoS_2, whereas the energy splitting of the valence band (VB) top at *K* caused by SOC is about 500 meV in the heaviest compound WSe_2.

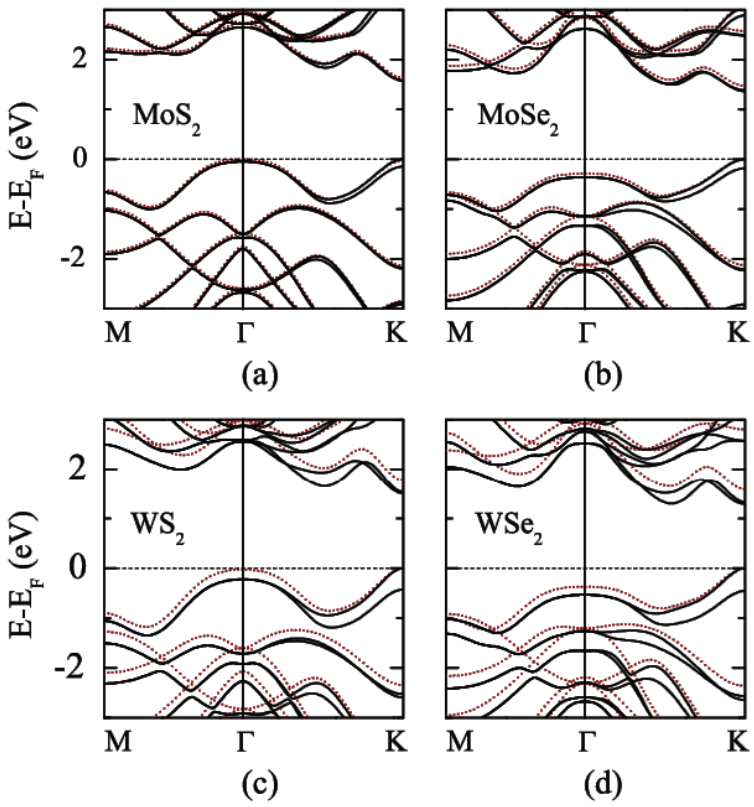


Fig. 2.9 Electronic structure dependence on the strength of SOC. Electronic structures calculated for MoS_2 (a), $MoSe_2$ (b), WS_2 (c) and WSe_2 (d) monolayer systems with (solid line) and without (dotted line) inclusion of the SOC. The figure is adapted from Ref. [16].

2.3 Exotic Properties

With variable crystal structure of different symmetries, tunable electronic structure of different Fermi surface topology, and the ability to be exfoliated to an atomic thin layer, TMDs have attracted intensive interest from both fundamental physics aspects and promising application potential as efficient electronics and spintronics. In this section, we will present a brief overview on the TMDs hosting charge density wave (CDW) and superconducting states (section 2.3.1), topological band structure (section 2.3.2) and other interesting properties as 2D materials (section 2.3.3).

2.3.1 Charge density waves and superconductivity

Charge density wave (CDW) states have been discovered in 1975 in group V TMDs [17]. Although CDWs are a common ground state for many metallic TMDs, their behaviors are very different. Since the classical Peierls model requires large parallel FS, it is challenging to apply this theory to quasi-2D TMD systems with complicated FS geometry [4]. Currently, there are various theories on the driving force for the formation of CDWs in TMDs including electron-phonon mediated Fermi surface nesting [18], van Hove singularity nesting [19], Fermi patch nesting [20], exciton insulators [21] and the formation of polarons [22]. However, they can only explain different parts of the experimental results and we still lack a universal picture.

CDWs are intriguing also because of its close relationship with superconductivity. They are usually next to each other in the phase diagram. TMDs in which with both CDW and superconducting phases coexist provide ideal platforms to study their correlation. Currently, most experimental results indicate competition between these two phases. The alkali

element intercalation of *2H-TaS_2* can suppress the CDW order but increase the superconducting transition temperature T_c [20, 23]. The emergence of superconductivity after the suppression of commensurate CDW order is observed in gate-controlled ionic intercalation of *1T-TaS_2* thin flakes [24]. For *2H-$TaSe_2$*, transport measurements show an enhancement of T_c and a suppression of CDW in the monolayer limit compared to the bulk crystal [25]. On the contrary, thickness dependent measurement on *2H-$NbSe_2$* shows an enhanced CDW order with weakened superconductivity as the thickness decreases [26, 27]. However, ARPES study on *2H-$NbSe_2$* illustrate that the maximized superconductivity at points in the momentum space are directly connected by the CDW ordering vector. This might indicate that CDWs can also boost superconductivity in the TMD systems and question the prevailing understanding of competition relation between these two phases [28].

Table 2.1 summarizes the CDW and superconducting states in several of the most studied TMDs. They include group IV *1T-MX_2*, group V *1T-MX_2* and group V *2H-MX_2*. CDW configuration, the transition temperature of CDW and superconducting phases are listed. Models that have been developed to describe the formation of these CDW states are also listed.

Compound	CDW (superlattice and T_{CDW})	T_{SC} (K)	Model
1T-$TiSe_2$ (group IV)	Commensurate 2×2×2 (202 *K*) [29]	4.15 for *$Cu_{0.08}TiSe_2$* [30]	Exciton insulator [21, 31]

1T-VSe$_2$ (group V)	In-plane commensurate 4×4 (3q), out-of-plane incommensurate $q_z = 0.314c^*$ (110 K) In-plane commensurate 4×4 (2q), out-of-plnae incommensurate $q_z = 0.307c^*$ (90 K) [32]	NA	Free-energy model [32]
2H-NbSe$_2$ (group V)	Incommensurate ~3×3 (33.5 K) [17]	7.2 [33]	Electron-phonon coupling asisted Fermi-surface nesting [18]
2H-TaSe$_2$ (group V)	Incommensurate ~3×3 (122 K) Commensurate 3×3 (90 K) [34]	0.15 [17]	Electron-phonon coupling asisted Fermi-surface nesting [18, 35]
2H-TaS$_2$ (group V)	Incommensurate ~3×3 (75 K) [36]	1 [37]	Fermi patch nesting [20]
1T-TaS$_2$ (group V)	Incommensurate ~$\sqrt{13} \times \sqrt{13}$ (543 K) Near Commensurate ~$\sqrt{13} \times \sqrt{13}$ (352 K) Commensurate ~$\sqrt{13} \times \sqrt{13}$ (183 K) [38]	5 for p>3 GPa [39]	Mott insulator [31], Formation of polarons [22]

Table 2.1 Summary of CDW and superconducting states in selected TMDs.

2.3.2 Nontrivial topological band structure

Topological quantum materials usually require a band inversion caused by strong SOC and appropriate symmetries which protect the degeneracy of states. As introduced in sections 2.1 and 2,2, the flexible crystal structures and tunable electronic structure of TMDs might provide a fertile group to search for novel quantum material with nontrivial topological band structure.

It has been reported that the trigonal crystal field in the *1T-MX_2* system can induce an intricate band structure with multiple band inversions [40, 41]. A series of TMDs which crystallize in *1T* or distorted *T'* structure was theoretically predicted to be topological nontrivial and then experimentally confirmed. For the bulk crystals, *1T-$PtSe_2$* family compounds are type-II Dirac semimetal (DSM) candidates [42] and the tilted Dirac cone along k_z direction has been observed by ARPES [40, 41, 43, 44]. *T_d-$MoTe_2$* hosts a type-II Weyl semimetal (WSM) phase by breaking the space inversion symmetry [12]. The *2M-WS_2* compound constructed from *1T'* WS_2 layers exhibits a superconducting transition at $T_c = 8.8$ K and it is predicted to host a single surface Dirac cone on the (100) surface. The coexistence of superconductivity and topological surface states (TSS) makes it a TSC candidate [10]. In addition to the bulk crystals, low-dimensional TMDs can also host topologically nontrivial phases. For example, the *1T'* phase of monolayer *WTe_2* is suggested as a large-gap quantum spin Hall (QSH) insulator [45], and later verified by ARPES [46], scanning tunneling microscopy (STM) [46], and transport studies [47, 48]. Table 2.2 summarizes selected TMDs with topologically nontrivial band structures.

Compound	Topological Class	Theory Refs	Experiment Refs
1T-$PdTe_2$ (bulk)	Type-II Dirac Semimetal	[42]	[13, 49-52]
1T-$PtTe_2$ (bulk)	Type-II Dirac Semimetal	[42]	[43, 53]
1T-$PtSe_2$ (bulk)	Type-II Dirac Semimetal	[42]	[41, 44]
T_d-$MoTe_2$ (bulk)	Type-II Weyl Semimetal	[54, 55]	[12]
2M-WS_2 (bulk)	Topological Superconductor	[10]	[10, 56]
1T'-WTe_2 (monolayer)	Quantum spin Hall Insulator	[45]	[46-48]

Table 2.2 Summary of TMDs with topologically nontrivial band structures.

2.3.3 Other interesting properties as 2D materials

TMDs are 2D materials with hexagonal lattice with similar lattice constant. Therefore, it makes them perfect to be fabricated as heterostructure with each other or with other 2D materials, such as graphene. For example, van der Waals *MoS_2-WSe_2* heterostructures have been studied by micro-ARPES. The interaction of two layers has been confirmed by the observation of distinct band dispersion around the Γ point [57]. The study on the *MoS_2*-graphene indicates a bandgap opening in the π band of graphene due to a periodic Moiré pattern created by lattice mismatch between graphene and MoS_2. Furthermore, motivated by the unexpected Mott state and superconducting phase in the magic-angle twist bilayer graphene superlattices [58, 59], signatures of Moiré-trapped valley excitons in *$MoSe_2$*/*WSe_2* heterobilayers have been reported [60-62]. It is also theoretically predicted that Moiré superlattices of bilayer TMDs can result in a mosaic pattern of topological insulator (TI) regions and normal insulator regions [63].

In addition to the van der Waals heterostructure in the vertical direction, the coplanar heterostructure also shows promising application potential. Laser irradiation induced phase

transition is reported between semiconducting *2H*- and metallic *1T'*-$MoTe_2$, achieving a true 2D device with an ohmic contact [64]. The extremely low contact barrier height is realized in the coplanar polymorphic integration of few-layer *1T'* and *2H-*$MoTe_2$ grown by chemical vapour deposition (CVD) [65]. The *2H/1T* transition in MoS_2 is achieved by electron beam irradiation [66] and chemical method [67]. These fruitful studies have shown that TMDs have the potential to become the next generation of highly efficient electronic devices [64-68].

References

[1] H.F. Yang, A.J. Liang, C. Chen, C.F. Zhang, N.B.M. Schroeter, Y.L. Chen, Visualizing electronic structures of quantum materials by angle-resolved photoemission spectroscopy, *Nature Reviews Materials*, **3** (2018) 341.

[2] S. Manzeli, D. Ovchinnikov, D. Pasquier, O.V. Yazyev, A. Kis, 2D transition metal dichalcogenides, *Nature Reviews Materials*, **2** (2017) 17033.

[3] M. Chhowalla, H.S. Shin, G. Eda, L.J. Li, K.P. Loh, H. Zhang, The chemistry of two-dimensional layered transition metal dichalcogenide nanosheets, *Nature Chemistry*, **5** (2013) 263.

[4] K. Rossnagel, On the origin of charge-density waves in select layered transition-metal dichalcogenides, *Journal of Physics: Condensed Matter*, **23** (2011) 213001.

[5] http://cci.lbl.gov/cctbx/explore_symmetry.html.

[6] Q.D. Gibson, L.M. Schoop, L. Muechler, L.S. Xie, M. Hirschberger, N.P. Ong, R. Car, R.J. Cava, Three-dimensional Dirac semimetals: Design principles and predictions of new materials, *Physical Review B*, **91** (2015) 205128.

[7] S.M. Young, C.L. Kane, Dirac Semimetals in Two Dimensions, *Physical Review Letters*, **115** (2015) 126803.

[8] C. Chen, X. Xu, J. Jiang, S.C. Wu, Y.P. Qi, L.X. Yang, M.X. Wang, Y. Sun, N.B.M. Schroter, H.F. Yang, L.M. Schoop, Y.Y. Lv, J. Zhou, Y.B. Chen, S.H. Yao, M.H. Lu, Y.F. Chen, C. Felser, B.H. Yan, Z.K. Liu, Y.L. Chen, Dirac line nodes and effect of spin-orbit coupling in the nonsymmorphic critical semimetals MSiS (M = Hf, Zr), *Physical Review B*, **95** (2017) 125126.

[9] A.J. Liang, J. Jiang, M.X. Wang, Y. Sun, N. Kumar, C. Shekhar, C. Chen, H. Peng, C.W. Wang, X. Xu, H.F. Yang, S.T. Cui, G.H. Hong, Y.Y. Xia, S.K. Mo, Q. Gao, X.J. Zhou, L.X. Yang, C. Felser, B.H. Yan, Z.K. Liu, Y.L. Chen, Observation of the topological surface state in the nonsymmorphic topological insulator *KHgSb*, *Physical Review B*, **96** (2017) 165143.

[10] Y. Fang, J. Pan, D. Zhang, D. Wang, H.T. Hirose, T. Terashima, S. Uji, Y. Yuan, W. Li, Z. Tian, J. Xue, Y. Ma, W. Zhao, Q. Xue, G. Mu, H. Zhang, F. Huang, Discovery of superconductivity in *2M* WS_2 with possible topological surface states, *Advanced Materials*, (2019) 1901942.

[11] https://materialsproject.org/.

[12] J. Jiang, Z.K. Liu, Y. Sun, H.F. Yang, C.R. Rajamathi, Y.P. Qi, L.X. Yang, C. Chen, H. Peng, C.C. Hwang, S.Z. Sun, S.K. Mo, I. Vobornik, J. Fujii, S.S.P. Parkin, C. Felser, B.H. Yan, Y.L. Chen, Signature of type-II Weyl semimetal phase in $MoTe_2$, *Nature Communications*, **8** (2017) 13973.

[13] M.S. Bahramy, O.J. Clark, B.J. Yang, J. Feng, L. Bawden, J.M. Riley, I. Markovic, F. Mazzola, V. Sunko, D. Biswas, S.P. Cooil, M. Jorge, J.W. Wells, M. Leandersson, T. Balasubramanian, J. Fujii, I. Vobornik, J.E. Rault, T.K. Kim, M. Hoesch, K. Okawa, M. Asakawa, T. Sasagawa, T. Eknapakul, W. Meevasana, P.D.C. King, Ubiquitous formation of bulk Dirac cones and topological surface states from a single orbital manifold in transition-metal dichalcogenides, *Nature Materials*, **17** (2018) 21.

[14] K. Rossnagel, N.V. Smith, Spin-orbit coupling in the band structure of reconstructed *1T-*TaS_2, *Physical Review B*, **73** (2006) 073106.

[15] Y. Ge, A.Y. Liu, Effect of dimensionality and spin-orbit coupling on charge-density-wave transition in *2H-*$TaSe_2$, *Physical Review B*, **86** (2012) 104101.

[16] Z.Y. Zhu, Y.C. Cheng, U. Schwingenschlogl, Giant spin-orbit-induced spin splitting in two-dimensional transition-metal dichalcogenide semiconductors, *Physical Review B*, **84** (2011) 153402.

[17] J.A. Wilson, F. Di Salvo, S. Mahajan, Charge-density waves and superlattices in the metallic layered transition metal dichalcogenides, *Advances in Physics*, **24** (1975) 117.

[18] F. Flicker, J. van Wezel, Charge order from orbital-dependent coupling evidenced by $NbSe_2$, *Nature Communications*, **6** (2015) 7034.

[19] T.M. Rice, G.K. Scott, New mechanism for a charge-density-wave instability, *Physical Review Letters*, **35** (1975) 120.

[20] D. Shen, B. Xie, J. Zhao, L. Yang, L. Fang, J. Shi, R. He, D. Lu, H. Wen, D. Feng, Novel mechanism of a charge density wave in a transition metal dichalcogenide, *Physical Review Letters*, **99** (2007) 216404.

[21] H. Cercellier, C. Monney, F. Clerc, C. Battaglia, L. Despont, M.G. Garnier, H. Beck, P. Aebi, L. Patthey, H. Berger, L. Forro, Evidence for an excitonic insulator phase in *1T-*$TiSe_2$, *Physical Review Letters*, **99** (2007) 146403.

[22] L. Stojchevska, I. Vaskivskyi, T. Mertelj, P. Kusar, D. Svetin, S. Brazovskii, D. Mihailovic, Ultrafast Switching to a Stable Hidden Quantum State in an Electronic Crystal, *Science*, **344** (2014) 177.

[23] A. König, K. Koepernik, R. Schuster, R. Kraus, M. Knupfer, B. Büchner, H. Berger, Plasmon evolution and charge-density wave suppression in potassium intercalated *2H-*$TaSe_2$, *EPL (Europhysics Letters)*, **100** (2012) 27002.

[24] Y.J. Yu, F.Y. Yang, X.F. Lu, Y.J. Yan, Y.H. Cho, L.G. Ma, X.H. Niu, S. Kim, Y.W. Son, D.L. Feng, S.Y. Li, S.W. Cheong, X.H. Chen, Y.B. Zhang, Gate-tunable phase transitions in thin flakes of *1T-TaS_2*, *Nature Nanotechnology*, **10** (2015) 270.

[25] Y.F. Yang, S. Fang, V. Fatemi, J. Ruhman, E. Navarro-Moratalla, K. Watanabe, T. Taniguchi, E. Kaxiras, P. Jarillo-Herrero, Enhanced superconductivity upon weakening of charge density wave transport in *2H-TaS_2* in the two-dimensional limit, *Physical Review B*, **98** (2018) 035203.

[26] M.M. Ugeda, A.J. Bradley, Y. Zhang, S. Onishi, Y. Chen, W. Ruan, C. Ojeda-Aristizabal, H. Ryu, M.T. Edmonds, H.Z. Tsai, A. Riss, S.K. Mo, D.H. Lee, A. Zettl, Z. Hussain, Z.X. Shen, M.F. Crommie, Characterization of collective ground states in single-layer *$NbSe_2$*, *Nature Physics*, **12** (2016) 92.

[27] X.X. Xi, L. Zhao, Z.F. Wang, H. Berger, L. Forro, J. Shan, K.F. Mak, Strongly enhanced charge-density-wave order in monolayer *$NbSe_2$*, *Nature Nanotechnology*, **10** (2015) 765.

[28] T. Kiss, T. Yokoya, A. Chainani, S. Shin, T. Hanaguri, M. Nohara, H. Takagi, Charge-order-maximized momentum-dependent superconductivity, *Nature Physics*, **3** (2007) 720.

[29] F.J. Disalvo, D.E. Moncton, J.V. Waszczak, Electronic properties and superlattice formation in semimetal *$TiSe_2$*, *Physical Review B*, **14** (1976) 4321.

[30] E. Morosan, H.W. Zandbergen, B.S. Dennis, J.W.G. Bos, Y. Onose, T. Klimczuk, A.P. Ramirez, N.P. Ong, R.J. Cava, Superconductivity in *Cu_xTiSe_2*, *Nature Physics*, **2** (2006) 544.

[31] S. Hellmann, T. Rohwer, M. Kallane, K. Hanff, C. Sohrt, A. Stange, A. Carr, M.M. Murnane, H.C. Kapteyn, L. Kipp, M. Bauer, K. Rossnagel, Time-domain classification of charge-density-wave insulators, *Nature Communications*, **3** (2012) 1069.

[32] D.J. Eaglesham, R.L. Withers, D.M. Bird, charge-density-wave transitions in *1T-VSe_2*, *Journal of Physics C-Solid State Physics*, **19** (1986) 359.

[33] F. Soto, H. Berger, L. Cabo, C. Carballeira, J. Mosqueira, D. Pavuna, P. Toimil, F. Vidal, Electric and magnetic characterization of *$NbSe_2$* single crystals: Anisotropic superconducting fluctuations above *T_C*, *Physica C-Superconductivity and Its Applications*, **460** (2007) 789.

[34] D.E. Moncton, J.D. Axe, F.J. Disalvo, Neutron-Scattering Study of Charge-Density Wave Transitions in *2H-$TaSe_2$* and *2H-$NbSe_2$*, *Physical Review B*, **16** (1977) 801.

[35] Y.W. Li, J. Jiang, H.F. Yang, D. Prabhakaran, Z.K. Liu, L.X. Yang, Y.L. Chen, Folded superstructure and degeneracy-enhanced band gap in the weak-coupling charge density wave system *2H-$TaSe_2$*, *Physical Review B*, **97** (2018) 115118.

[36] G.A. Scholz, O. Singh, R.F. Frindt, A.E. Curzon, Charge-density wave commensurability in *2H-TaS_2* and *Ag_xTaS_2*, *Solid State Communications*, **44** (1982) 1455.

[37] S. Nagata, T. Aochi, T. Abe, S. Ebisu, T. Hagino, Y. Seki, K. Tsutsumi, Superconductivity in the layered compound *2H-TaS_2*, *Journal of Physics and Chemistry of Solids*, **53** (1992) 1259.

[38] S.C. Bayliss, A.M. Ghorayeb, D.R.P. Guy, Thermal and transport evidence for a phase-transition in *1T-TaS_2* observed at 282 K upon warming, J*ournal of Physics C-Solid State Physics*, **17** (1984) L533.

[39] B. Sipos, A.F. Kusmartseva, A. Akrap, H. Berger, L. Forro, E. Tutis, From Mott state to superconductivity in *1T-TaS_2*, *Nature Materials*, **7** (2008) 960.

[40] M.S. Bahramy, O.J. Clark, B.J. Yang, J. Feng, L. Bawden, J.M. Riley, I. Markovic, F. Mazzola, V. Sunko, D. Biswas, S.P. Cooil, M. Jorge, J.W. Wells, M. Leandersson, T. Balasubramanian, J. Fujii, I. Vobornik, J.E. Rault, T.K. Kim, M. Hoesch, K. Okawa, M. Asakawa, T. Sasagawa, T. Eknapakul, W. Meevasana, P.D.C. King, Ubiquitous formation of bulk Dirac cones and topological surface states from a single orbital manifold in transition-metal dichalcogenides, *Nature Materials*, **17** (2018) 21.

[41] Y.W. Li, Y.Y.Y. Xia, S.A. Ekahana, N. Kumar, J. Jiang, L.X. Yang, C. Chen, C.X. Liu, B.H. Yan, C. Felser, G. Li, Z.K. Liu, Y.L. Chen, Topological origin of the type-II Dirac fermions in *$PtSe_2$*, *Physical Review Materials*, **1** (2017) 074202.

[42] H.Q. Huang, S.Y. Zhou, W.H. Duan, Type-II Dirac fermions in the *$PtSe_2$* class of transition metal dichalcogenides, *Physical Review B*, **94** (2016) 121117.

[43] M. Yan, H. Huang, K. Zhang, E. Wang, W. Yao, K. Deng, G. Wan, H. Zhang, M. Arita, H. Yang, Lorentz-violating type-II Dirac fermions in transition metal dichalcogenide *$PtTe_2$*, *Nature Communications*, **8** (2017) 257.

[44] K.N. Zhang, M.Z. Yan, H.X. Zhang, H.Q. Huang, M. Arita, Z. Sun, W.H. Duan, Y. Wu, S.Y. Zhou, Experimental evidence for type-II Dirac semimetal in *$PtSe_2$*, *Physical Review B*, **96** (2017) 125102.

[45] X.F. Qian, J.W. Liu, L. Fu, J. Li, Quantum spin Hall effect in two-dimensional transition metal dichalcogenides, *Science*, **346** (2014) 1344.

[46] S.J. Tang, C.F. Zhang, D. Wong, Z. Pedramrazi, H.Z. Tsai, C.J. Jia, B. Moritz, M. Claassen, H. Ryu, S. Kahn, J. Jiang, H. Yan, M. Hashimoto, D.H. Lu, R.G. Moore,

C.C. Hwang, C. Hwang, Z. Hussain, Y.L. Chen, M.M. Ugeda, Z. Liu, X.M. Xie, T.P. Devereaux, M.F. Crommie, S.K. Mo, Z.X. Shen, Quantum spin Hall state in monolayer *1T'-WTe_2*, *Nature Physics*, **13** (2017) 683.

[47] S.F. Wu, V. Fatemi, Q.D. Gibson, K. Watanabe, T. Taniguchi, R.J. Cava, P. Jarillo-Herrero, Observation of the quantum spin Hall effect up to 100 kelvin in a monolayer crystal, *Science*, **359** (2018) 76.

[48] Z.Y. Fei, T. Palomaki, S.F. Wu, W.J. Zhao, X.H. Cai, B.S. Sun, P. Nguyen, J. Finney, X.D. Xu, D.H. Cobden, Edge conduction in monolayer *WTe_2*, *Nature Physics*, **13** (2017) 677.

[49] Y. Liu, J.-Z. Zhao, L. Yu, C.-T. Lin, A.-J. Liang, C. Hu, Y. Ding, Y. Xu, S.-L. He, L. Zhao, G.-D. Liu, X.-L. Dong, J. Zhang, C.-T. Chen, Z.-Y. Xu, H.-M. Weng, X. Dai, Z. Fang, X.-J. Zhou, Identification of Topological Surface State in *$PdTe_2$* Superconductor by Angle-Resolved Photoemission Spectroscopy, *Chinese Physics Letters*, **32** (2015) 067303.

[50] H.-J. Noh, J. Jeong, E.-J. Cho, K. Kim, B. Min, B.-G. Park, Experimental Realization of Type-II Dirac Fermions in a *$PdTe_2$* Superconductor, *Physical Review Letters*, **119** (2017) 016401.

[51] O.J. Clark, M.J. Neat, K. Okawa, L. Bawden, I. Markovic, F. Mazzola, J. Feng, V. Sunko, J.M. Riley, W. Meevasana, J. Fujii, I. Vobornik, T.K. Kim, M. Hoesch, T. Sasagawa, P. Wahl, M.S. Bahramy, P.D.C. King, Fermiology and Superconductivity of Topological Surface States in *$PdTe_2$*, *Physical Review Letters*, **120** (2018) 156401.

[52] F.C. Fei, X.Y. Bo, R. Wang, B. Wu, J. Jiang, D.Z. Fu, M. Gao, H. Zheng, Y.L. Chen, X.F. Wang, H.J. Bu, F.Q. Song, X.G. Wan, B.G. Wang, G.H. Wang, Nontrivial Berry

phase and type-II Dirac transport in the layered material $PdTe_2$, *Physical Review B*, **96** (2017) 041201.

[53] D.Z. Fu, X.Y. Bo, F.C. Fei, B. Wu, M. Gao, X.F. Wang, M. Naveed, S.A. Shah, H.J. Bu, B.G. Wang, L. Cao, W.Q. Zou, X.G. Wan, F.Q. Song, Quantum oscillations in type-II Dirac semimetal $PtTe_2$, *Physical Review B*, **97** (2018) 245109.

[54] A.A. Soluyanov, D. Gresch, Z.J. Wang, Q.S. Wu, M. Troyer, X. Dai, B.A. Bernevig, Type-II Weyl semimetals, *Nature*, **527** (2015) 495.

[55] Y. Sun, S.C. Wu, M.N. Ali, C. Felser, B.H. Yan, Prediction of Weyl semimetal in orthorhombic $MoTe_2$, *Physical Review B*, **92** (2015) 161107.

[56] Y. Yuan, J. Pan, X. Wang, Y. Fang, C. Song, L. Wang, K. He, X. Ma, H. Zhang, F. Huang, W. Li, Q.K. Xue, Evidence of anisotropic Majorana bound states in 2M-WS_2, *Nature Physics*, **1** (2019).

[57] N.R. Wilson, P.V. Nguyen, K. Seyler, P. Rivera, A.J. Marsden, Z.P.L. Laker, G.C. Constantinescu, V. Kandyba, A. Barinov, N.D.M. Hine, X.D. Xu, D.H. Cobden, Determination of band offsets, hybridization, and exciton binding in 2D semiconductor heterostructures, *Science Advances*, **3** (2017) e1601832.

[58] Y. Cao, V. Fatemi, S. Fang, K. Watanabe, T. Taniguchi, E. Kaxiras, P. Jarillo-Herrero, Unconventional superconductivity in magic-angle graphene superlattices, *Nature*, **556** (2018) 43.

[59] Y. Cao, V. Fatemi, A. Demir, S. Fang, S.L. Tomarken, J.Y. Luo, J.D. Sanchez-Yamagishi, K. Watanabe, T. Taniguchi, E. Kaxiras, R.C. Ashoori, P. Jarillo-Herrero, Correlated insulator behaviour at half-filling in magic-angle graphene superlattices, *Nature*, **556** (2018) 80.

[60] K.L. Seyler, P. Rivera, H.Y. Yu, N.P. Wilson, E.L. Ray, D.G. Mandrus, J.Q. Yan, W. Yao, X.D. Xu, Signatures of moire-trapped valley excitons in $MoSe_2/WSe_2$ heterobilayers, *Nature*, **567** (2019) 66.

[61] K. Tran, G. Moody, F.C. Wu, X.B. Lu, J. Choi, K. Kim, A. Rai, D.A. Sanchez, J.M. Quan, A. Singh, J. Embley, A. Zepeda, M. Campbell, T. Autry, T. Taniguchi, K. Watanabe, N.S. Lu, S.K. Banerjee, K.L. Silverman, S. Kim, E. Tutuc, L. Yang, A.H. MacDonald, X.Q. Li, Evidence for moire excitons in van der Waals heterostructures, *Nature*, **567** (2019) 71.

[62] C.H. Jin, E.C. Regan, A.M. Yan, M.I.B. Utama, D.Q. Wang, S.H. Zhao, Y. Qin, S.J. Yang, Z.R. Zheng, S.Y. Shi, K. Watanabe, T. Taniguchi, S. Tongay, A. Zettl, F. Wang, Observation of moire excitons in WSe_2/WS_2 heterostructure superlattices, *Nature*, **567** (2019) 76.

[63] Q.J. Tong, H.Y. Yu, Q.Z. Zhu, Y. Wang, X.D. Xu, A. Yao, Topological mosaics in moire superlattices of van der Waals heterobilayers, *Nature Physics*, **13** (2017) 356.

[64] S. Cho, S. Kim, J.H. Kim, J. Zhao, J. Seok, D.H. Keum, J. Baik, D.H. Choe, K.J. Chang, K. Suenaga, S.W. Kim, Y.H. Lee, H. Yang, Phase patterning for ohmic homojunction contact in $MoTe_2$, *Science*, **349** (2015) 625.

[65] J.H. Sung, H. Heo, S. Si, Y.H. Kim, H.R. Noh, K. Song, J. Kim, C.S. Lee, S.Y. Seo, D.H. Kim, H.K. Kim, H.W. Yeom, T.H. Kim, S.Y. Choi, J.S. Kim, M.H. Jo, Coplanar semiconductor-metal circuitry defined on few-layer $MoTe_2$ via polymorphic heteroepitaxy, *Nature Nanotechnology*, **12** (2017) 1064.

[66] Y.C. Lin, D.O. Dumcencon, Y.S. Huang, K. Suenaga, Atomic mechanism of the semiconducting-to-metallic phase transition in single-layered MoS_2, *Nature Nanotechnology*, **9** (2014) 391.

[67] R. Kappera, D. Voiry, S.E. Yalcin, B. Branch, G. Gupta, A.D. Mohite, M. Chhowalla, Phase-engineered low-resistance contacts for ultrathin MoS_2 transistors, *Nature Materials*, **13** (2014) 1128.

[68] M. Acerce, D. Voiry, M. Chhowalla, Metallic *1T* phase MoS_2 nanosheets as supercapacitor electrode materials, *Nature Nanotechnology*, **10** (2015) 313.

Chapter 3

ARPES Study on the CDW System *2H-$TaSe_2$*

Charge-density waves (CDWs) have been studied in quasi-two-dimensional (quasi-2D) transition metal dichalcogenides (TMDs) for decades [1-3]. However, two fundamental questions remain unsolved from an electronic structure perspective [4]: (1) what influence do CDWs have on the electron-lattice system, or how does electronic band reconstruct in a CDW phase? (2) What is the driving force of the CDW transition? For the first question, pseudogap states have been reported near the normal-incommensurate transition temperature [5-7]. In the commensurate regime, Fermi surface (FS) folding, band folding, CDW gap opening, and mysterious high-energy "kinks" have been observed by angle-resolved photoemission spectroscopy (ARPES) [8-11]. However, there still exists controversy about the most fundamental parameter, the size of the CDW gap obtained by different experimental approaches (including ARPES [5, 10, 12, 13], scanning tunnelling spectroscopy [14], and optical spectroscopy [15]), which calls for further exploration. For the second questions, the leading candidate model for CDW mechanism, FS nesting (Peierls instability indicated by a divergence of electronic susceptibility) faces constant questioning in quasi-2D systems [16, 17]. Unlike quasi-1D cases in which the nesting criterion is reasonably met due to perfectly parallel FS sheets [18], FS topology is much more complicated and hence weak-nested in quasi-2D CDW systems [16]. To make this model solid, more effects including electron-electron interaction [11] and momentum-dependent

electron-phonon coupling [17, 19, 20] are introduced. Some researchers imply that 2D systems might fall in the strong-coupling regime [4, 21] where the classical Peierls weak-coupling model [21-23] fails. Besides, other mechanisms such as Fermi patch nesting [24], saddle point nesting [25] and lattice-driven [26] models are proposed. In short, there is still intense controversy on electronic band reconstruction in the CDW phase and essential lack of a standard model for CDW formation in quasi-2D TMDs.

Although, as a typical quasi-2D CDW system, *2H-$TaSe_2$* has been intensively investigated in the past decades, there still lacks consistency between various experimental results with existing theories. On one hand, the electronic structure of *2H-$TaSe_2$* detected by ARPES near the Fermi level shows a clear gap opening and backfolding features in the CDW phase [4, 5, 10]. From temperature-dependent measurements [7, 27], superstructure order and the FS nesting vector show consistent evolution. These results strongly favour the conventional nesting instability to be the major driven force of the CDW phase although part of the folded bands (FBs) remains experimentally elusive [4, 5]. On the other hand, theorists believe that a Peierls nested construction is mathematically too fragile to be applied to TMD systems [17]. Despite the argument on the driving mechanism, an extreme uncertainty of the magnitude of the CDW gap in *2H-$TaSe_2$* from 24 to 160 meV [10, 12-15] makes it an ambiguous criterion for theory screening.

In this chapter, we report a systematic ARPES study on the typical CDW system *2H-$TaSe_2$*. We directly observe the fine structure of FBs near $\bar{\Gamma}$ which is missing in the previous ARPES study on the CDW phase of *2H-$TaSe_2$* (see section 3.3). CDW band gap with precise momentum-energy distribution has been revealed (see section 3.4). Our comprehensive experimental results and analysis validate the band hybridization picture suggested in previous studies [4, 10]. Beyond that, a strong correlation between the degeneracy of band crossings and the magnitude of the gap is experimentally confirmed by a dramatic

enhancement of gap size at corresponding momentum. We propose a general model for CDWs in the 2D systems as electron-phonon coupling mediated FS nesting as shown in section 3.6.

3.1 Overview of CDW in *2H-$TaSe_2$*

The crystal structure of *2H-$TaSe_2$* has been elaborated in section 2.1.1. *2H-$TaSe_2$* exhibits a second-order transition from normal metallic phase to near commensurate 3×3 ordered phase at 122 K followed by a first-order lock-in transition to the commensurate 3×3 ordered phase at 90 K [4] upon cooling. With virtually the highest commensurate CDW onset temperature in *2H*-TMD family [28], electronic band reconstruction in *2H-$TaSe_2$* is reasonably strong for observation. Moreover, compared to other classical TMD systems such as Mott insulator *1T-TaS_2* [11] and superconducting *2H-$NbSe_2$* [9], the phase diagram of *2H-$TaSe_2$* is less complex. Mott state caused by electron-electron interaction is excluded. The superconducting transition at an extremely low temperature of 0.15 K [28] indicates minimal competition against CDWs. Thus, *2H-$TaSe_2$* is a relatively pure and canonical system for 2D-CDW measurements and a touchstone for modelling.

The CDW in *2H-$TaSe_2$* causes a significant reconstruction of atomic coordination in real space as well as electronic band structure in reciprocal space, as shown in Fig. 3.1. In real space, six Ta_b atoms move towards the centre Ta_a atom, forming a seven-atom cluster, while the Ta_c positions remain unchanged [4]. In reciprocal space, in agreement with early studies [4, 5, 10], the $\overline{K}$-centred hole-pocket completely disappears whereas the $\overline{M}$-centred electron-pocket is partially gapped, forming triangular pockets on the FS. The details of the structure of the folded band in the CDW phase will be elaborated in section 3.3. The validity of 3×3 FS folding (details of this model can be found in Appendix B) in the momentum space is

strengthened as all these experimental features have their counterparts in the calculation, as shown in Fig. 1.1(d).

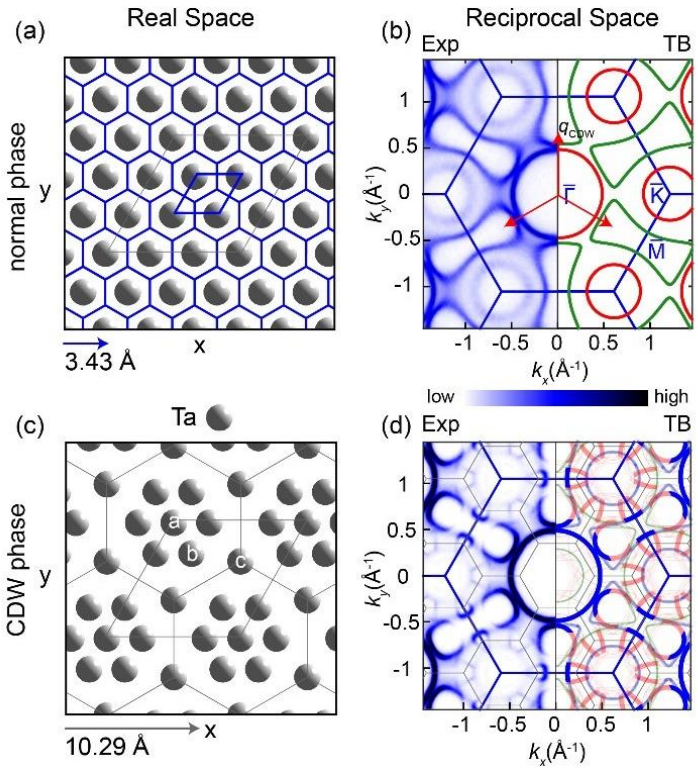
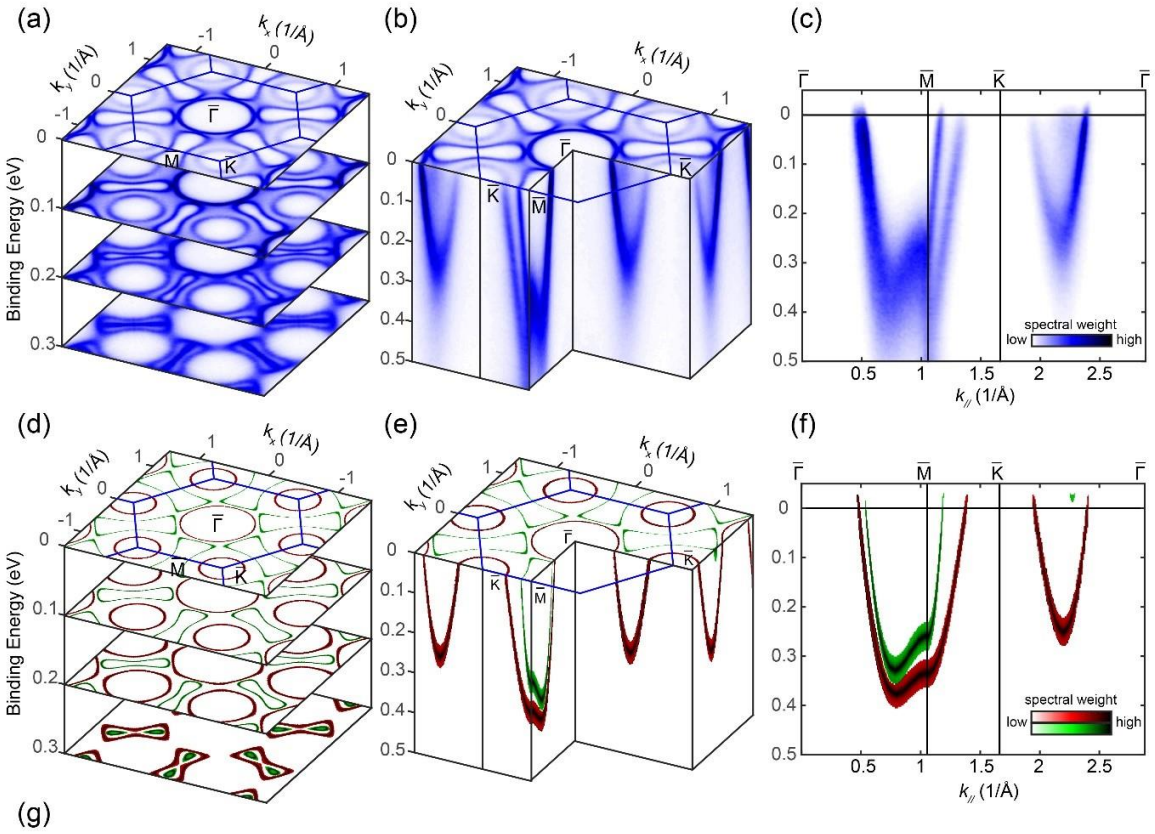


Fig. 3.1 Superlattice formation and FS reconstruction in the CDW phase transition. *Ta* layer atomic arrangement in the (a) normal phase and (c) CDW phase. Wigner-Seitz (hexagon) and conventional (rhombus) unit cells are appended with blue lines. Note that the atomic displacement in the CDW phase is exaggerated for better illustration. The new unit cells under the tripled translation vector (the grey arrow) are appended with grey lines. In the (b) normal phase and (d) CDW phase, ARPES measured Fermi surface (left panel) and corresponding TB fitting (right panel) are compared. TB fitting based on 3×3 FS folding (details and principles can be found in Appendix B) can well explain the measured band reconstruction at 10 K. The main bands (MBs), first- and second-order folded bands (FBs) are marked by blue, red and green lines, respectively. The thickness of lines indicates spectral weight enhancement due to the pronounced matrix element effect. The triple CDW nesting vectors $q = \frac{2}{3}\bar{\Gamma}\bar{M}$ are indicated by red arrows in (b).

3.2 Band Structure of the High-temperature Phase

3.2.1 In-plane band structure

As shown in Figs. 3.2(a)-(c), the ARPES-measured electronic structure in the high-temperature normal phase shows a clear semimetallic nature. The in-plane FS consists of circular hole-pocket centred at $\bar{\Gamma}$ and $\bar{K}$, and "dog-bone" electron-pockets centred at $\bar{M}$ [see Figs. 3.2(a) and (b)]. The electron- and hole-pockets are from two different band sheets. The experimental band dispersion agrees well with previous ARPES study [4, 5, 10] and recent *ab initio* calculation [29], though in which E_F is slightly overestimated by about 50 meV. The semimetal FS topology originate directly from its chemical configuration: The *Ta-Se* bond requires four electrons from each *Ta* atom since the oxidation of *Ta* and *Se* are +4 and -2, respectively. Considering the outermost electron shell of *Ta* atom is $6\boldsymbol{s^2}5\boldsymbol{d^3}$, there is one $5\boldsymbol{d}$ conducting electron left for each site (two electrons for a unit cell) half-filling the two band sheets at Fermi level [30].



(g)

meV	t_0	t_1	t_2	t_3	t_4	t_5
α band (red)	-45.1	157.8	203.2	25.7	0.02	0.48
β band (green)	501.3	-15.9	557.1	-72.0	-13.9	12.2

Fig. 3.2 ARPES measured and Tight-binding (TB) reconstructed band structure in the normal phase. (a)-(c) ARPES data. (a), Equal energy contours from E_F to $E_F - 0.3$ eV. (b) The 3D plot of ARPES data. (c) Cut along momentum $\bar{\Gamma} - \bar{M} - \bar{K} - \bar{\Gamma}$. (d)-(f) TB calculations of (a)-(c), which show a good agreement with ARPES data (a)-(c). Two band sheets are presented in red and green, respectively. An arbitrary Lorentzian convolution is applied in the calculations for a better comparison with ARPES data. (g) Fitted parameters of the TB calculations.

For further analysis of the fine band structure in the low-temperature CDW phase [see section 3.3] based on the analytical band dispersion of the high-temperature normal phase,

we have performed an empirical two-dimensional tight-binding (TB) model [9, 10, 16, 31] to fit local maxima of spectral data:

$$\begin{aligned} E(\boldsymbol{k}) = t_0 &+ t_1(2\cos\xi\cos\eta + \cos 2\xi) \\ &+ t_2(2\cos 3\xi\cos\eta + \cos 2\eta) \\ &+ t_3(2\cos 2\xi\cos 2\eta + \cos 4\xi) \\ &+ t_4(\cos\xi\cos 3\eta + \cos 5\xi\cos\eta + \cos 4\xi\cos 2\eta) \\ &+ t_5(\cos 3\xi\cos 3\eta + \cos 6\xi) \end{aligned}$$

where $\boldsymbol{k} = (k_x, k_y)$ denotes the wave vectors parallel to the cleavage surface as k_x along $\bar{\Gamma}\bar{K}$ and k_y along $\bar{\Gamma}\bar{M}$, $\xi = \frac{1}{2}k_x a$ and $\eta = \frac{\sqrt{3}}{2}k_y a$ (a is the in-plane lattice constant). Note that this fitting model only aims at extracting an analytical formula of the band dispersion. Basically, such a method can fit all kinds of band structure under a given symmetry if we add enough terms. Therefore, no specific physical meaning is attached to the hopping parameters t_i as they have in the TB theory. The fitting result is presented in Figs. 3.2(d)-(f) which matches the ARPES data perfectly, and the fitted parameters are listed in Fig. 3.2(g).

3.2.2 Out-of-plane band structure

Since *2H-TaSe*$_2$ is a layered quasi-2D material, we should not expect a very strong band dispersion along the k_z direction. However, as we have discussed in section 2.1.1, the non-symmorphic symmetry of *2H*-structure requires the band degeneracy at the $k_z = \pi$ plane in the non-SOC cases and along $A - L$ in the SOC cases.

As shown in Fig. 3.3, the above argument has been confirmed in *2H-TaSe*$_2$. The *ab initio* calculation indicates a four-fold degenerated band at $A - L - H - A$ plane if SOC is excluded [4, 31]. When SOC is applied, the degeneracy is lifted except along $A - L$ direction, as shown in Figs. 3.3(c) and (d). The overall FS topology at different k_z changes

slightly which is consistent with the quasi-2D nature of this material, as illustrated in Fig. 3.3 (d).

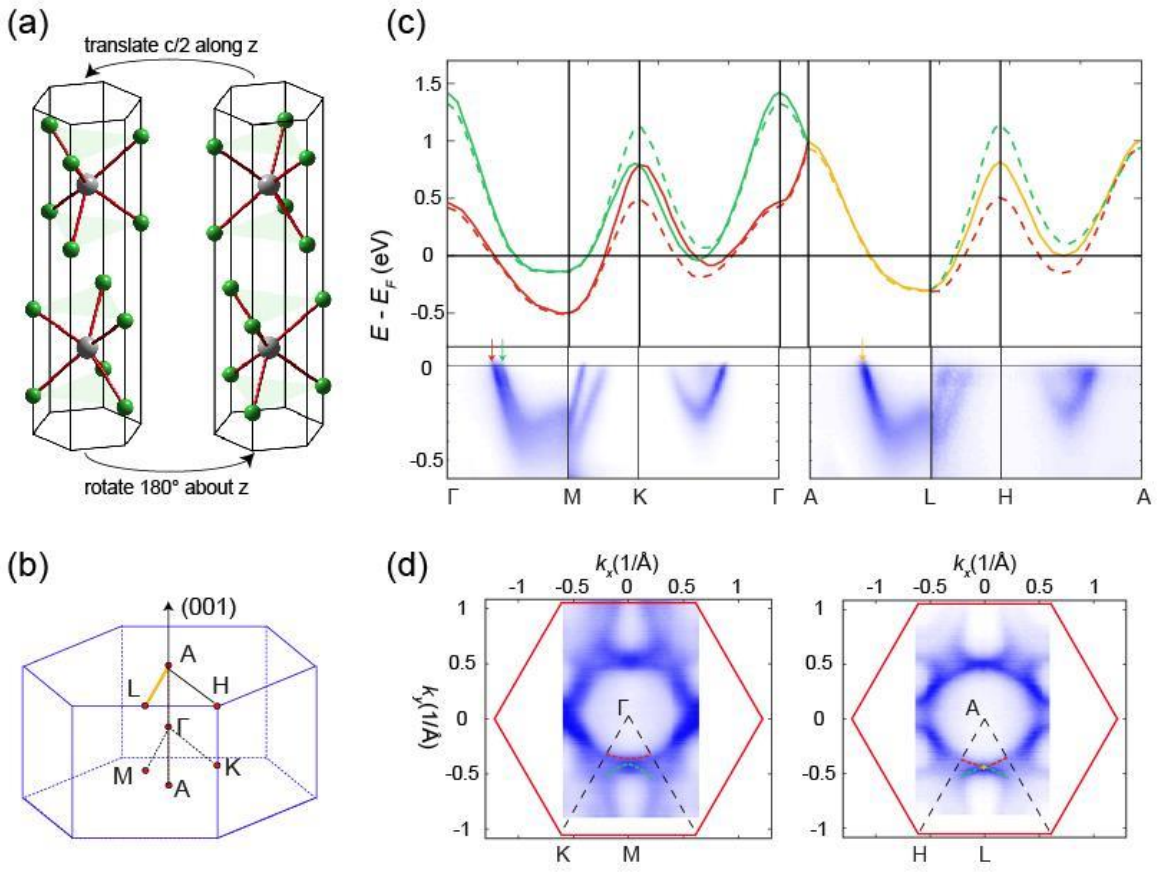


Fig. 3.3 Non-symmorphic symmetry protected band degeneracy. (a) The non-symmorphic screw symmetry operation of the *2H*-structure. (b) 3D BZ of *2H-TaSe*$_2$. The non-symmorphic protected degenerated line along $A-L$ is marked as the yellow line. (c) *Ab initio* calculated (upper panel) and ARPES measured (lower panel) band dispersion at $\Gamma-M-K-\Gamma$ plane and $A-L-H-A$ plane, showing good agreement. Calculation excluding (including) SOC is indicated as solid (dashed) lines. Two band are marked in red and green respectively, and the four-fold degenerated band is marked in yellow. (d) FS mapping at $k_z=\Gamma$ plane (left panel) and $k_z=A$ plane (right panel). The ARPES measurement is collected at 176 K.

From the photon-energy-dependent measurement, we can clearly see the band evolution from $\Gamma - M$ to $A - L$, as shown in Fig. 3.4. The band splitting reaches its maximum at $\Gamma - M$ whereas become degenerated at $A - L$.

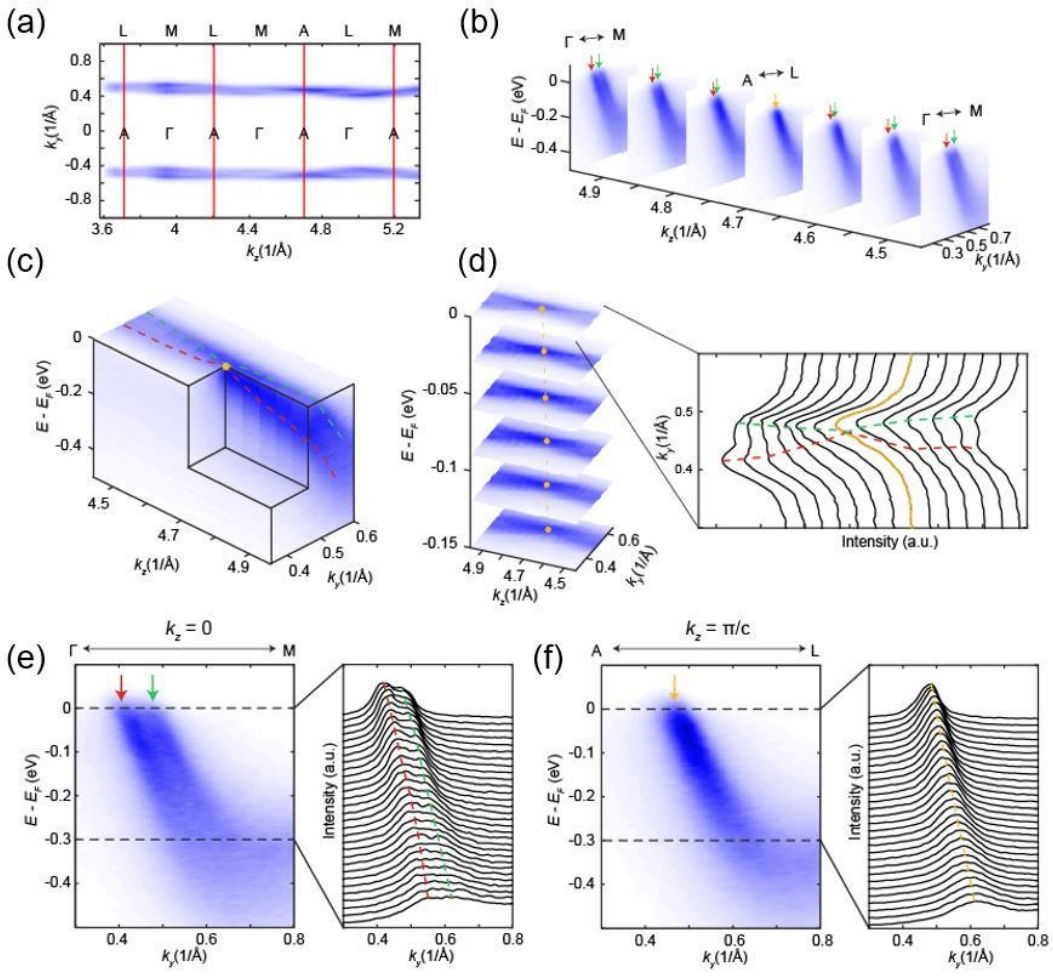


Fig. 3.4 k_z-dependent ARPES measurement from $\Gamma - M$ to $A - L$. (a) Fermi surface in the $k_y - k_z$ plane. (b) Band dispersion evolution from $\Gamma - M$ to $A - L$. (c) 3D plot of k_z-dependent ARPES data. (d) Equal energy contours in the $k_y - k_z$ plane from E_F to $E_F -$ 0.15 eV (left panel). MDC stacking plot of equal energy contour at E_F. (e) Cut along $\Gamma - M$ (left panel) and corresponding MDC stacking plot (right panel). (f) Cut along $A - L$ (left panel) and corresponding MDC stacking plot (right panel). Two bands are indicated as red and green markers. The degenerated band along $A - L$ is indicated as yellow markers. The ARPES measurement is collected at 176 K.

3.3 Fine Structure of Folded Bands in the Low-Temperature CDW Phase

3.3.1 Band structure reconstruction in CDW phase

A general comparison of band structure between the high-temperature normal phase and low-temperature CDW phase is presented in Fig. 3.5. As shown in the 3D intensity plots [Figs. 3.5(a) and (b)], the band reconstruction in the CDW phase happens not only near E_F, but also at high binding energies, as marked in Fig. 3.5(b). Consistent with previous report [5], we have observed clear pseudogaps at $\bar{K}$-centred hole-pockets [see Fig. 3.5(c)] marked by the suppression of spectral weight near E_F. In the CDW state, we observe clear CDW gap as large as 70 meV at the Fermi crossing of the $\bar{K}$-centred pockets. We also notice some anomalies of band dispersions at high binding energy [see Fig. 3.5(d)]. The momentum positions of these high energy anomalies match exactly with the band crossings between the main band (MB) and corresponding folded bands (FBs) as predicted by TB simulation [see Fig.3.5(e)]. However, the fine structure of FBs around $\bar{\Gamma}$ is very weak with this measured photon energy (80 eV) in Fig. 3.5, which is probably due to the matrix element effect induced by the weak CDW superpotential [31]. To see the fine structure of the FBs clearly, we switch to another photon energy (50 eV) in the following, where the intensity around $\bar{\Gamma}$ is significantly enhanced (the possibility of the contribution from the k_z effect has been ruled out as discussed in Appendix C).

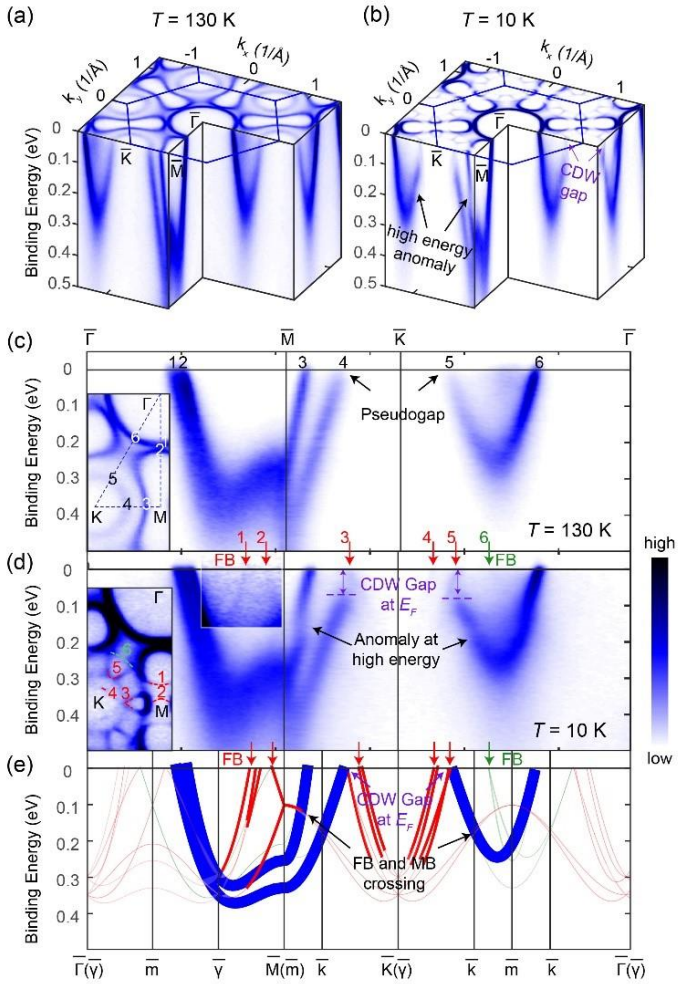


Fig. 3.5 Band structure reconstruction in the 3×3 CDW phase. (a), (b) 3D intensity plot of ARPES data using photon energy 80 eV measured in normal phase at 130 K (a) and CDW phase at 10 K (b). (c)-(e) Comparison among experimental band dispersion in normal phase (c), CDW phase (d), and calculation (e) based on TB fitting and FS folding scheme (see more details in Appendix B) along high symmetry direction $\bar{\Gamma} - \bar{K} - \bar{M} - \bar{\Gamma}$. In (c), (d) the insets show corresponding ARPES FS maps. Features at E_F are marked correspondingly. In (e), MBs, first- and second-order FBs are marked with blue, red, and green lines, respectively. The thickness of lines in TB fitting indicates spectral weight enhancement due to pronounced matrix element effect.

3.3.2 CDW folded bands (FBs) and new translational symmetry

Here, we provide an equivalent interpretation for CDW band reconstruction as FS folding but from a distinct perspective to emphasize the new translational symmetry. As indicated in the upper panel of Fig. 3.6(a), if all bands (MBs plus FBs) in the CDW phase are included, regardless of the prominent matrix element effect, then the FS should have the corresponding symmetry of the mini-BZs (new BZ based on the tripled translational vector in CDW phase). Take two mini-BZs, mini-BZ *1* marked magenta centred at $\bar{\Gamma}$ and mini-BZ *2* marked green next to it, as examples. They are indistinguishable as linked by a CDW reciprocal vector $\boldsymbol{q} = \frac{2}{3}\bar{\Gamma}\bar{M}$ but totally different in the normal phase. When the systems evolve into the CDW phase, identical band dispersions form in both mini-BZs. However, their intensities are "rendered" unevenly as if they are in a "background" of different MBs. Mini-BZ *1* has a "blank background", so it is rendered by pure CDW FB features in the low-temperature phase [see the upper panel of Fig. 3.6(b)]. The direct observation of the fine-folded superstructure without any interference of MBs provides compelling experimental evidence for FS folding scheme under 3×3 ordering. In contrast, mini-BZ *2* is under an MB "background" with mirror symmetry, hence its CDW spectrum shows a weak FB feature with a six-fold rotational symmetry appended on top [see the lower panel of Fig. 3.6(b)].

This perspective is further strengthened by a detailed comparison of band dispersions between the CDW phase and the normal phase in mini-BZ *2* [Figs. 3.6(c)-(f)]. Before, the new symmetry is introduced, high symmetric points, $\bar{m}_i$ ($i = 1,2,3,4$) and $\bar{k}_j$ ($j = 1,2,3$) are inequivalent in momentum space, hence corresponding band dispersions vary [see Figs. 3.6(c) and (d)]. The formation of FBs under CDW superpotential compensates for this difference in the CDW state [see Figs. 3.6(e) and (f)], making the dispersion near $\bar{m}_i$ (and $\bar{k}_j$) equivalent except for intensity difference. The emergence of FBs is revealed by ARPES

intensity plots [Figs. 3.6(e) and (f)] as well as corresponding peaks in the momentum distribution curve (MDC) plots [Figs. 3.6(i) and (j)].

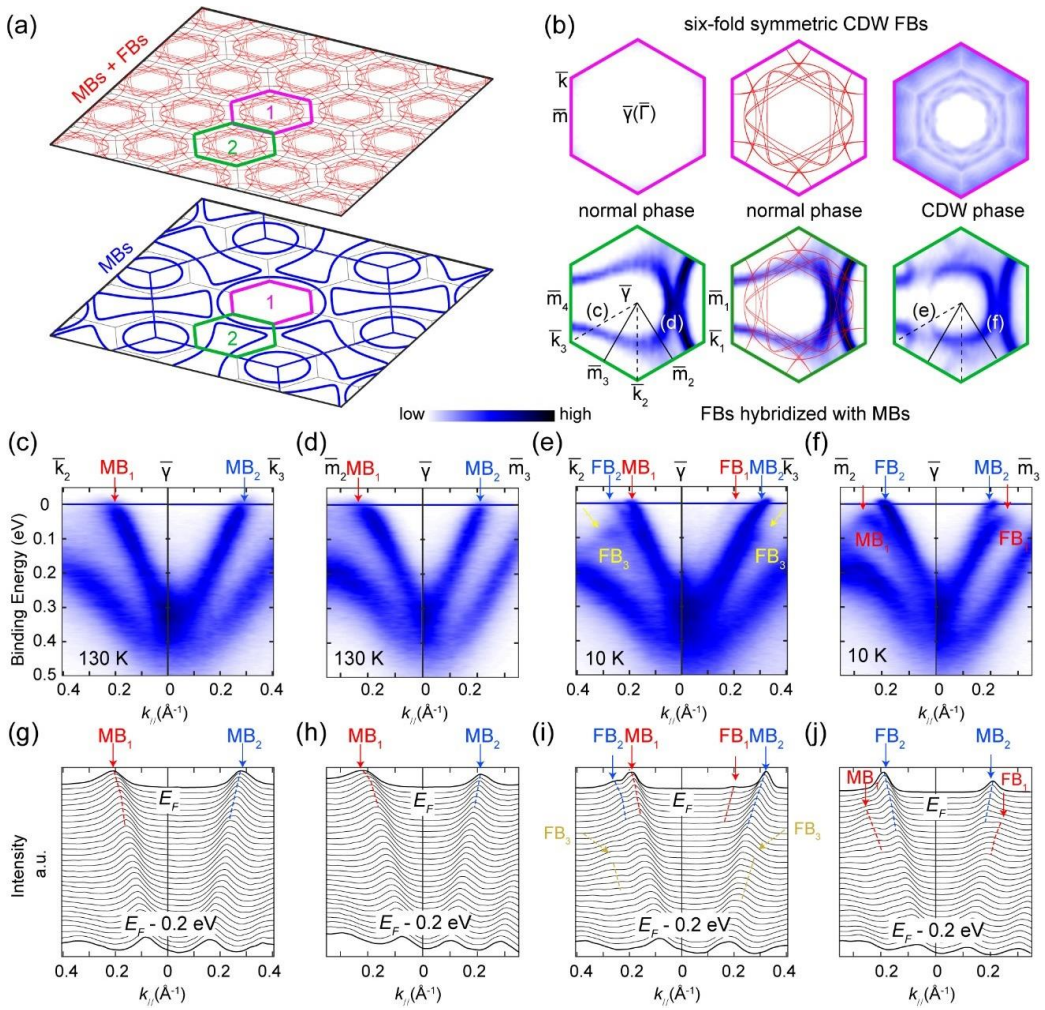


Fig. 3.6 Weak FBs features with new periodicity on top of MBs. (a) Schematics of FS of MBs (lower) and overall bands (MBs + FBs) in the CDW phase (upper). Original BZs and the new mini-BZs are marked by blue and grey lines. The two-bold mini-BZs (*1*, magenta; *2*, green) are selected to present how FBs interact with MBs in (b). (b) Pure folded features with six-fold rotational symmetry (upper row) and folded features under the influence of MBs (lower row) in mini-BZ *1* and mini-BZ *2* indicated in (a), respectively. (c), (d) Normal phase experimental band dispersion along $\bar{k}_2 - \bar{\gamma} - \bar{k}_3$ (c) and $\bar{m}_2 - \bar{\gamma} - \bar{m}_3$ (d) in mini-BZ *2* indicated in (b). (e), (f) Same as (c), (d) but in CDW phase. (g)-(j) MDC plots of (c)-(f) in an energy window from E_F to $E_F - 0.2$ eV.

Based on this understanding, the mini-BZ becomes the building block with all the information on electronic structure in CDW regime. The FS in a single mini-BZ consists of concentric multi-walled $\bar{\gamma}$-centred electron-pockets and double-walled $\bar{k}$-centred electron-pockets (see Fig. 3.7). We note that the sign of the Hall coefficient reverses [6] during the CDW phase transition, which may be related to the annihilation of hole-pockets on the FS.

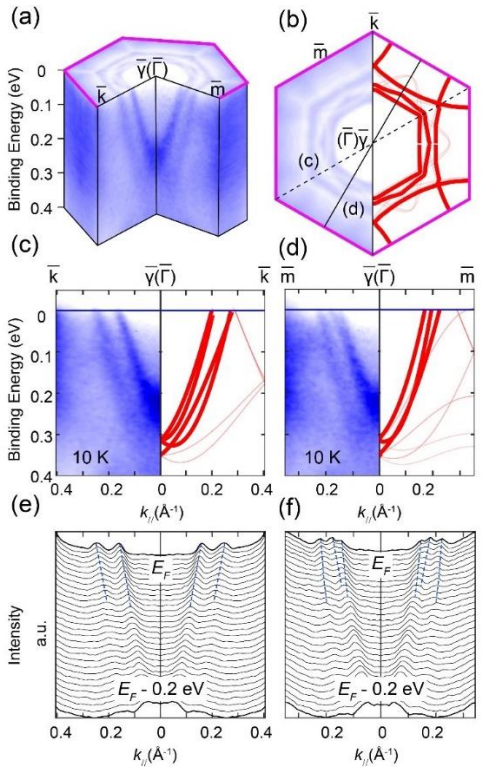


Fig. 3.7. Pure folded features at $\bar{\Gamma}$. (a) 3D intensity plot of ARPES data of mini-BZ *1* [the magenta hexagon shown in Fig. 3.6(a)] in CDW phase. (b) Zoomed-in FS around $\bar{\Gamma}$ showing pure folded features. Comparison shows an excellent agreement between experimental E_F contour (left) and corresponding simulation based on TB fitting and FS folding (right). (c), (d) Comparisons show an excellent agreement between experimental CDW band dispersion and corresponding simulation based on TB fitting and FS folding along $\bar{k} - \bar{\gamma}(\bar{\Gamma}) - \bar{k}$ (c) and $\bar{m} - \bar{\gamma}(\bar{\Gamma}) - \bar{m}$ (d). The small mismatch between experiment and calculation of the binding energy of band bottom at $\bar{\Gamma}$ might be a k_z effect (discussions can be found in Appendix C). (e), (f) MDC plots of (c), (d) in an energy window from E_F to $E_F - 0.2$ eV.

3.4 Distribution of the Magnitude of CDW Gaps in the Momentum-Energy Space

3.4.1 Distribution of the location of CDW gaps in the momentum space

Our systematic ARPES study has confirmed the validity of the FS folding scheme on electronic band structure reconstruction in the CDW regime. To some extent, the first question on the electronic structure reconstruction in the CDW phase raised in the beginning of this chapter is answered. However, why this state is energetically favoured remains elusive. Borisenko *et al.* [5] have suggested that energy gain, marked by the formation of pseudogaps at $\bar{K}$-centred hole-pockets, occurs near the CDW onset transition at 122 K, despite that the normal-to-incommensurate CDW transition is second order with no latent heat associated. However, the lock-in transition around 90 K is first-order, supported by a hysteresis on specific heat [32], we thus argue that discontinuous energy gain should occur when commensurate CDW FBs are formed and band gaps are created near E_F. The observed pseudogap [see Fig. 3.5(c)], on the other hand, may originate from precursor fluctuations of the CDW order in the normal state [5, 27].

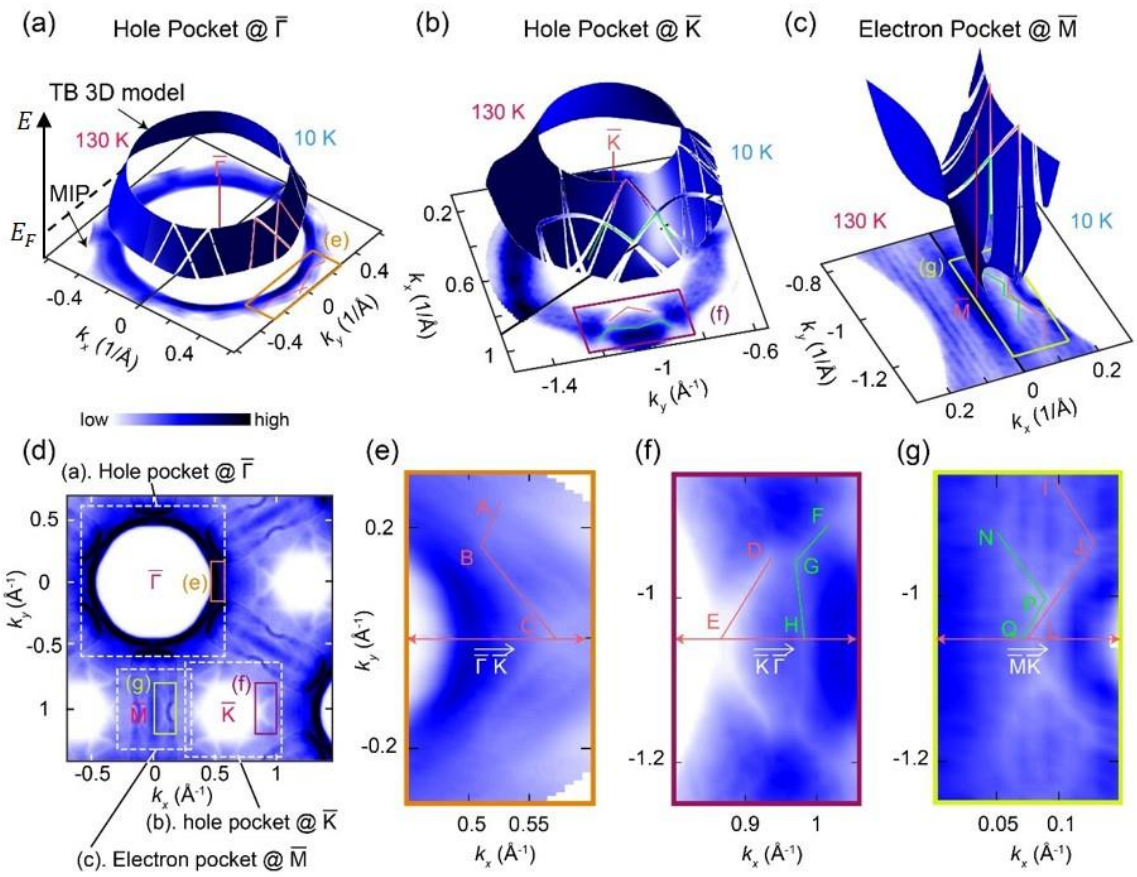


Fig. 3.8 Maximum intensity projection (MIP) and CDW gap candidates. (a)-(c) Illustration of 3D TB band sheet (upper) and corresponding MIP map (lower) in three momentum areas: hole-pocket centred at $\bar{\Gamma}$ (a), hole-pocket centred at $\bar{K}$, and dog-bone electron-pocket centred at $\bar{M}$ (c). The transparent patterns in the 3D models are intersection lines between the MB sheet (blue surface) and the first-order FB sheets (not shown), which are regarded as CDW gap candidates. Their projection matches nicely with the dip features in MIP. (d) MIP map in a wide momentum range. White dashed rectangles indicate the momentum areas shown in (a)-(c) and coloured rectangles indicate the momentum areas shown in (e)-(g). (e)-(g) Zoomed-in MIP map of specific momentum area in (a)-(c). The projection of the CDW gap candidates in $k_x - k_y$ plane is highlighted by solid lines.

Identification and positioning of the CDW gap in momentum space has never been a trivial process [4]. We notice that a dip in the local density of states (LDOS) is created at the energy positions where the band gap is formed under a periodic potential. Similarly, CDW gaps should also suppress the spectral weight of the MB along energy and leave a local dip in the intensity map. Based on this idea, we have developed a method using the dip trace in the maximum intensity projection (MIP) map (see more details in section 1.2.4) to track the momentum distribution of the CDW gap. 2D momentum distributions of the CDW gap candidates are illustrated in the broad MIP map [Fig. 3.8(d)] and three zoomed-in areas [Figs. 3.8(e)-(g)], which show excellent agreement with the intersection lines between MB and FB sheets based on TB model in Figs. 3.8(a)-(c). We thus suggest that CDW gaps are caused by hybridization between MBs and FBs.

3.4.2 Nesting degeneracy enhanced CDW gaps

To further visualize these band gaps, band dispersions along the gap positions are presented in comparison with high-temperature counterparts (see Fig. 3.9). We have proved that the MIP method not only precisely locates the CDW gaps in the momentum space, but also render gap values that are consistent with the ones measured by the conventional method (see also in Appendix D). Most of the expected gaps (e.g., $A - B - C$ [Fig. 3.9(a)] and $D - E$ [Fig. 3.9(b)]) are resolved, whereas other only render broad features (e.g., $I - J$ [Fig. 3.9(d)]) due to finite energy resolution and broadening effects. Both two MB sheets forming the electron- and hole-pockets in the normal phase open CDW gaps with intricate momentum-energy distribution over the whole BZ in an energy window over 0.2 eV. The gap which completely destroys the $\overline{K}$-centred hole-pocket at E_F is an extension of $D - E$

[see Figs. 3.8(b), 3.8(f) and 3.9(b)], and the one which partially gap the $\bar{M}$-centred electron-pocket is an extension of $L-J$ and $I-J$ below E_F [see Figs. 3.8(c), 3.8(g) and 3.9(d)].

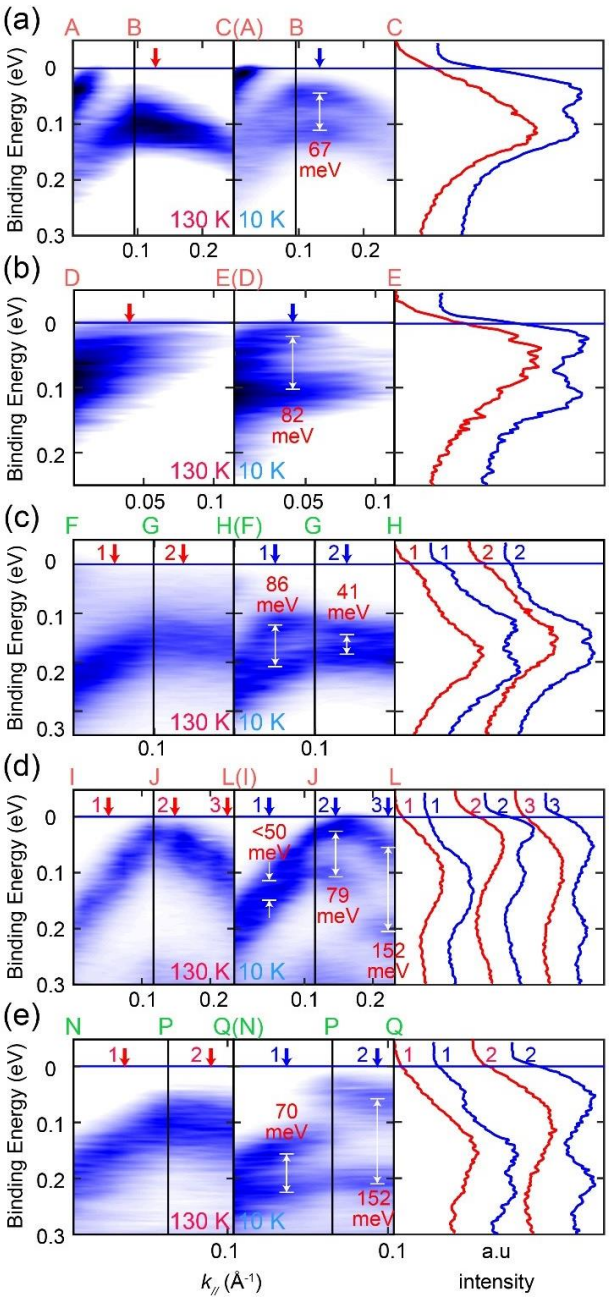


Fig. 3.9 Band dispersion along CDW gap candidates. Comparison of band dispersion along the CDW gap candidates (shown in Fig. 3.8) between normal (130 K, left) and CDW phase (10 K, middle). Energy distribution curves (EDCs) plots (right) at the momenta of interest marked by red and blue arrows in normal and CDW phase, respectively, show a split density of states (DOS), indicating the formation of CDW gaps.

Interestingly, we have obtained various values of CDW gaps of 2Δ varying from below 50 meV [e.g., the gap between *G* and *H* shown in Fig. 3.9(c)] to above 140 meV [e.g., the gap near *L* and *Q* shown in Figs. 3.9(d) and (e), respectively] at different energy-momentum positions and noticed that the magnitude of CDW gap has a strong dependence on nesting degeneracy (which is defined by the number of the first-order FBs intersected with the given MB). This effect is most evident along gap $J - L$ where the magnitude jumps from about 80 to over 140 meV near the quadruple *L* point [see Fig. 3.9(d)]. The degeneracy dependence argument also provides an explanation for the anisotropy of the gap size on the $\bar{K}$-centred hole-pocket reported in the early study [10]. Since point *E* in the $\bar{K} - \bar{\Gamma}$ direction is also quadruple-degenerated, gap size reaches its maxima accordingly [see Figs. 3.8(f) and 3.9(b)]. Furthermore, as the concept of a constant gap is no longer valid, we can put an end to debates among various experimental results from 24 to 160 meV [4].

Our TB model shows that most of the experimentally observed CDW gaps have a nesting degeneracy factor of 2 except for the highly degenerate crossing points of gaps [e.g., $A - B - C$ excluding *B* and *C* shown in Fig. 3.8(e), $D - E$ excluding *E* shown in Fig. 3.8(f), and $I - J - L$ excluding *J* and *L* shown in Fig. 3.8(g)]. The magnitude of these band gap with a nesting degeneracy of 2 range from 40 to 90 meV [see Fig. 3.9]. The anisotropy in the gap magnitude with the same nesting degeneracy suggests that a moderate-to-strong momentum-dependent electron-phonon coupling [17, 19, 20, 33, 34] might also play a role in the formation of CDW.

Although the CDW gaps below E_F might have limited contribution to the energy gain of the electron subsystem and thus attract less research interest, we prove that they can be the key to understand the CDW formation in the quasi-2D TMD system. First, as the gaps at E_F

are extensions of the lower ones, they must have the same origin which we attribute to the hybridization between MBs and FBs. Second, the magnitudes of gaps below E_F are well defined as both the lower and upper bands are clearly seen in ARPES measurements. The magnitudes of gaps at E_F, on the contrary, are tricky to quantitatively measure as the upper CB is unreachable. To deduce the full gap size, the assumption of particle-hole symmetry must be applied, which might not be preserved in this system [35]. Since the gaps at and below E_F are evolved from one to another and have the same nature, they should have comparable size. Therefore, surprisingly, since CDW formation results in prominent gap opening at high binding energy, it might imply that band sheets below E_F also play a part in the transition in contrast to the conventional FS nesting [29].

3.5 Electronic Susceptibility

Under the assumption that electron-phonon coupling does not vary with momentum, we can calculate the bare electronic susceptibility χ_q directly from the band structure obtained by ARPES and TB fitting using Lindhard function [4, 16] as follow:

$$\chi_q = \frac{1}{N}\sum_{\boldsymbol{k}}(f_{\boldsymbol{k+q}} - f_{\boldsymbol{k}})/(\epsilon_{\boldsymbol{k}} - \epsilon_{\boldsymbol{k+q}}),$$

where $f_{\boldsymbol{k}}$ is the Fermi-Dirac distribution function for state $\epsilon_{\boldsymbol{k}}$ and N is the number of atoms in the system. From the property of the Fermi-Dirac distribution, we can see that only the states near E_F contribute significantly to electronic susceptibility. In the conventional picture of Fermi nesting, the driving mechanism for the formation of CDW originates from the divergence of electronic susceptibility at $\boldsymbol{q}_{CDW}$. Therefore, in this picture, the CDW instability is a direct result of the special topology of the FS.

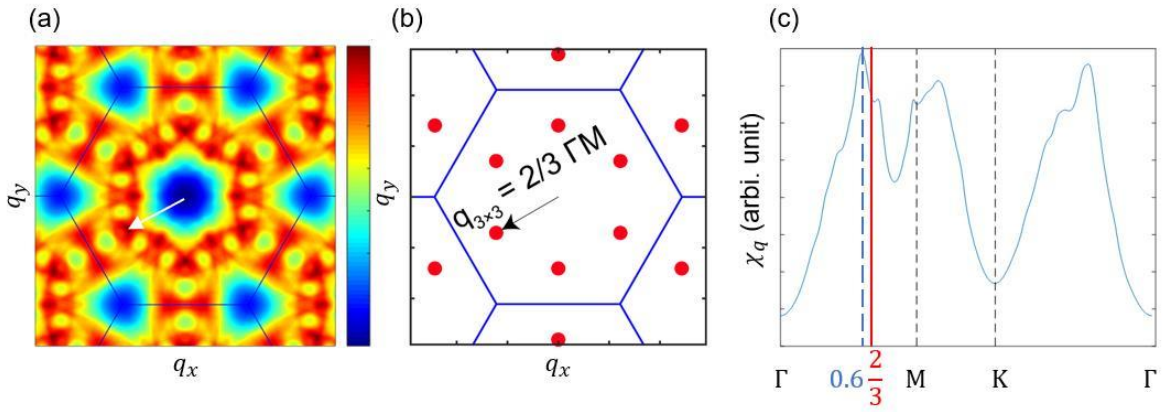


Fig. 3.10 Bare electronic susceptibility of *2H-TaSe*$_2$. (a) 2D distribution in the $q_x - q_y$ plane of the calculated bare electronic susceptibility of *2H-TaSe*$_2$. The white arrow indicates the "hot spot" in the calculated electronic susceptibility. (b) Schematic of expected "hot spot" of electronic susceptibility which is related to the CDW vector $\boldsymbol{q}_{3\times3}$, as indicated by the black arrow. (c) Electronic susceptibility dispersion along $\Gamma - M - K - \Gamma$ extracted from (a) shows the global peak at $0.6\ \Gamma M$, indicated as the blue dashed line, slightly off the expected CDW vector $\boldsymbol{q}_{3\times3} = \frac{2}{3}\Gamma M$ indicated as the red solid line.

Figure 3.10 shows the calculated bare electronic susceptibility based on the ARPES data and TB fitting. We can clearly see that the "hot spot" in the calculated map [see Fig. 3.10(a)] near the expected CDW vector $\boldsymbol{q}_{3\times3} = \frac{2}{3}\Gamma M$ [see Fig. 3.10(b)]. However, as shown in Fig. 3.10(c), there is a small discrepancy between the peak position of the calculated electronic susceptibility and the CDW vector. This might attribute to the invalidity of the assumption that electron-phonon coupling does not rely on the momentum. As we have illustrated in section 3.4.2, *2H-TaSe*$_2$ is a system with moderate to strong momentum dependent electron-phonon coupling supported by the anisotropy of CDW band gap size. Therefore, we believe that, similar as the successful model applied to *2H-NbSe*$_2$ [34], the CDW formation in *2H-TaSe*$_2$ can be explained by an electron-phonon coupling mediated FS nesting mechanism

taking into account both the full momentum and orbital dependence of the coupling matrix elements.

3.6 General Model of CDW in *2H*-TMDs: Electron-phonon Coupling mediated FS Nesting

From our systematic ARPES study on the CDW in *2H-TaSe*$_2$, we suggest the hybridization interpretation of CDW gaps based on the fine band structure in the low-temperature phase is valid, which is a natural expansion and development of previous ARPES studies [4, 10]. Rossnagel *et al.* [10] have proposed that band hybridization can be an alternative explanation for the high-energy kinks and anisotropy gap around *K* point compared to the electron-boson mode coupling effect argument. In our study, by mapping out the complete CDW gap distribution over the entire BZ, we recognize that the high energy "kinks" are extension of CDW gaps from the Fermi level to high binding energy. Our results confirm the validity of band hybridization, thus favour the electron-driven mechanism of the CDW formation. On the other hand, we also provide experimental evidence on momentum-dependent electron-phonon coupling.

Our analysis on the CDW gaps might give an insight on the controversy whether the weak-coupling Peierls model or the strong-coupling McMillan model [21] works better in a realistic quasi-2D *2H*-TMD system. Although an unexpected large gap magnitude [4, 10] is observed by ARPES, we believe it is too hasty to classify this system to strong-coupling regime. The experimentally observed band gap magnitude (with a nesting degeneracy factor of 2) of 40-90 meV is significantly larger than predicted value of 37 meV in the weak-coupling limit if the transition temperature of 122 K is given ($2\Delta(0) = 3.52k_BT$) [4]. On the

contrary, the strong-coupling theory provides a reasonable gap size of 73.5 meV ($2\Delta(0) = 7k_BT$) [4]; however, it requires a much severer lattice distortion of 0.16 Å rather than 0.05 Å suggested by neutron scattering measurements [3, 21, 36]. Our argument on CDW gap formation might give a favourable turn for the classical Peierls model in this dilemma. Peierls classical view in the simple 1D case describes homogeneous and complete CDW gaps at the mini-BZ boundary under the interaction between corresponding MB and a single FB [Figs. 3.11(a)-(c)]. In contrast, although FS in 2D-CDW system is partially gapped, triple-nesting-vector-induced FBs increase the degeneracy of the band crossing and thus further amplify the band gap magnitude. Degeneracy-enhanced CDW gaps near E_F stabilize the system and compensate for the poor FS nesting condition [Figs. 3.11(d)-(f)]. Therefore, although the measured gap size does not match the theoretical prediction, from an "average" perspective, since about half of the FS are gapped by interaction with two FBs, the gap value ($2\Delta \times 0.5 \approx 3.52k_BT_{CDW}$) should fall into the weak-coupling range.

To be more accurate, we should discard the classification between weak- and strong-coupling systems since the electron-coupling has nonnegligible momentum dependence. It is more adequate to describe *2H-$TaSe_2$* as an electron-phonon mediated FS nesting driven CDW system. However, as we have argued above, on the average level, it should fit into the weak-coupling regime.

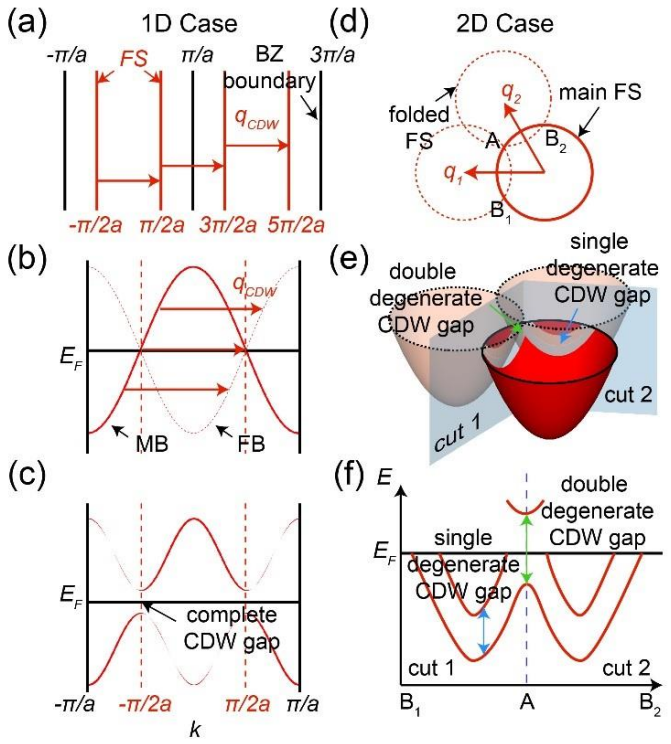


Fig. 3.11 Schematics of 1D and 2D Peierls CDW model. (a)-(c) Schematic of 1D Peierls CDW model. FS sheets (a) connected by the CDW nesting vector (marked by red arrows) in the 1D case are parallel to each other. FS nesting condition is well met. Dispersions of the MB and FB in the first BZ cross right at E_F (b). Interaction between the MB and a single FB cause the complete CDW gap opening at the boundary of the new mini-BZ (c). (d)-(f) Schematic of 2D Peierls CDW model. In the 2D case, folded FS and main FS only cross at discrete momentum (*A*, B_1 and B_2) at E_F (d). Note that two FBs cross with MB at A. Interaction between the MB and FBs only partially create CDW gaps at E_F; however, they extend to high binding energy (e). (f) Dispersions along CDW gaps $B_1 - A$ and $A - B_2$ indicated by blue shaded cut *1* and cut *2* in (e). CDW gap magnitude near the double degenerate point *A* is significantly larger than neighbouring single-degenerate ones. The CB near *A* is not shown in (e).

At the end of this chapter, taking *2H-$TaSe_2$* as a typical example, we describe how CDW are formed and influence the electronic band structure in quasi-2D TMD system. During the CDW transition, the delocalized *Ta* 5***d*** electrons driven by the electron-phonon mediated Peierls instability form a density modulation wave in the real space. Correspondingly in momentum space, FBs are formed as FS nesting suggested. Hybridization between MBs and FBs creates band gaps which lower the energy of electron subsystem. Through electron-phonon coupling, *Ta* atoms move to their new equilibrium position and form the 3×3 superlattice, whereas *Se* atoms are barely affected.

In summary, we have presented a direct observation of 3×3 CDW-induced FBs and constructed an appropriate model that accounts for the CDW gaps in *2H-$TaSe_2$*. Our results and modelling suggest that CDW instability in *2H-$TaSe_2$* can be explained by the electron-phonon mediated FS nesting as the driving mechanism.

Method

Sample Preparation: $2H - TaSe_2$ single crystals were grown from Ta metal and Se by iodine vapor transport [37].

ARPES: ARPES measurements were performed at beamline I05 high-resolution branch (Diamond Light Source, UK) equipped with an R4000 electron analyzer. Normal and CDW phase are measured at 130 K and 10 K, respectively. Fermi surface mapping was done using $h\nu = 80$ eV and 50 eV. The sample was mounted on the sample holder using epoxy and cleaved *in situ* in the ultrahigh vacuum.

References

[1] C. Scruby, P. Williams, G. Parry, The role of charge density waves in structural transformations of *1T* TaS_2, *Philosophical Magazine*, **31** (1975) 255.

[2] J.A. Wilson, F. Di Salvo, S. Mahajan, Charge-density waves and superlattices in the metallic layered transition metal dichalcogenides, *Advances in Physics*, **24** (1975) 117.

[3] D.E. Moncton, J.D. Axe, F.J. Disalvo, Neutron-Scattering Study of Charge-Density Wave Transitions in *2H-*$TaSe_2$ and *2H-*$NbSe_2$, *Physical Review B*, **16** (1977) 801.

[4] K. Rossnagel, On the origin of charge-density waves in select layered transition-metal dichalcogenides, *Journal of Physics: Condensed Matter*, **23** (2011) 213001.

[5] S. Borisenko, A. Kordyuk, A. Yaresko, V. Zabolotnyy, D. Inosov, R. Schuster, B. Büchner, R. Weber, R. Follath, L. Patthey, Pseudogap and charge density waves in two dimensions, *Physical Review Letters*, **100** (2008) 196402.

[6] D. Evtushinsky, A. Kordyuk, V. Zabolotnyy, D. Inosov, B. Büchner, H. Berger, L. Patthey, R. Follath, S. Borisenko, Pseudogap-driven sign reversal of the Hall effect, *Physical review letters*, **100** (2008) 236402.

[7] D. Inosov, D. Evtushinsky, V. Zabolotnyy, A. Kordyuk, B. Büchner, R. Follath, H. Berger, S. Borisenko, Temperature-dependent Fermi surface of *2H-*$TaSe_2$ driven by competing density wave order fluctuations, *Physical Review B*, **79** (2009) 125112.

[8] T. Valla, A. Fedorov, P. Johnson, J. Xue, K. Smith, F. DiSalvo, Charge-density-wave-induced modifications to the quasiparticle self-energy in *2H-*$TaSe_2$, *Physical Review Letters*, **85** (2000) 4759.

[9] D. Rahn, S. Hellmann, M. Kalläne, C. Sohrt, T. Kim, L. Kipp, K. Rossnagel, Gaps and kinks in the electronic structure of the superconductor *2H-$NbSe_2$* from angle-resolved photoemission at 1 K, *Physical Review B*, **85** (2012) 224532.

[10] K. Rossnagel, E. Rotenberg, H. Koh, N. Smith, L. Kipp, Fermi surface, charge-density-wave gap, and kinks in *2H-$NbSe_2$*, *Physical Review B*, **72** (2005) 121103.

[11] K. Rossnagel, E. Rotenberg, H. Koh, N.V. Smith, L. Kipp, Continuous tuning of electronic correlations by alkali adsorption on layered *1T-TaS_2*, *Physical Review Letters*, 95 (2005) 126403.

[12] R. Liu, W. Tonjes, V. Greanya, C. Olson, R. Frindt, Fermi surface of *2H−$TaSe_2$* and its relation to the charge-density wave, *Physical Review B*, **61** (2000) 5212.

[13] R. Liu, C. Olson, W. Tonjes, R. Frindt, Momentum Dependent Spectral Changes Induced by the Charge Density Wave in *2H−$TaSe_2$* and the Implication on the CDW Mechanism, *Physical Review Letters*, **80** (1998) 5762.

[14] C. Wang, B. Giambattista, C. Slough, R. Coleman, M. Subramanian, Energy gaps measured by scanning tunneling microscopy, *Physical Review B*, **42** (1990) 8890.

[15] J. Demsar, L. Forró, H. Berger, D. Mihailovic, Femtosecond snapshots of gap-forming charge-density-wave correlations in quasi-two-dimensional dichalcogenides *1T−TaS_2* and *2H−$TaSe_2$*, *Physical Review B*, **66** (2002) 041101.

[16] D. Inosov, V. Zabolotnyy, D. Evtushinsky, A. Kordyuk, B. Büchner, R. Follath, H. Berger, S. Borisenko, Fermi surface nesting in several transition metal dichalcogenides, *New Journal of Physics*, **10** (2008) 125027.

[17] M. Johannes, I. Mazin, Fermi surface nesting and the origin of charge density waves in metals, *Physical Review B*, **77** (2008) 165135.

[18] G. Gruner, The Dynamics of Charge-Density Waves, *Reviews of Modern Physics*, **60** (1988) 1129.

[19] Y. Yoshida, K. Motizuki, Electron-Lattice interactions and lattice instabilities of *1T-VSe_2*, *1T-$CrSe_2$* and *1T-TiS_2*, *Journal of the Physical Society of Japan*, **51** (1982) 2107.

[20] K. Motizuki, E. Ando, Theoretical-Study of lattice instability and lattice-dynamics of *2H-$TaSe_2$* and *2H-$NbSe_2$* .1. electron-lattice interaction and generalized electronic susceptibility, *Journal of the Physical Society of Japan*, **52** (1983) 2849.

[21] W.L. McMillan, Microscopic model of charge-density waves in *2H-$TaSe_2$*, *Physical Review B*, **16** (1977) 643.

[22] S.-K. Chan, V. Heine, Spin density wave and soft phonon mode from nesting Fermi surfaces, *Journal of Physics F: Metal Physics*, **3** (1973) 795.

[23] A.W. Overhauser, Charge-density waves and isotropic metals, *Advances in Physics*, **27** (1978) 343.

[24] D. Shen, B. Xie, J. Zhao, L. Yang, L. Fang, J. Shi, R. He, D. Lu, H. Wen, D. Feng, Novel mechanism of a charge density wave in a transition metal dichalcogenide, *Physical Review Letters*, **99** (2007) 216404.

[25] T.M. Rice, G.K. Scott, New mechanism for a charge-density-wave instability, *Physical Review Letters*, **35** (1975) 120.

[26] J.X. Dai, E. Calleja, J. Alldredge, X.D. Zhu, L.J. Li, W.J. Lu, Y.P. Sun, T. Wolf, H. Berger, K. McElroy, Microscopic evidence for strong periodic lattice distortion in two-dimensional charge-density wave systems, *Physical Review B*, **89** (2014) 165140.

[27] P. Leininger, D. Chernyshov, A. Bosak, H. Berger, D. Inosov, Competing charge density waves and temperature-dependent nesting in *2H-$TaSe_2$*, *Physical Review B*, **83** (2011) 233101.

[28] A.H. Castro Neto, Charge density wave, superconductivity, and anomalous metallic behavior in 2D transition metal dichalcogenides, *Physical Review Letters*, **86** (2001) 4382.

[29] J. Laverock, D. Newby Jr, E. Abreu, R. Averitt, K. Smith, R. Singh, G. Balakrishnan, J. Adell, T. Balasubramanian, k-resolved susceptibility function of *2H-$TaSe_2$* from angle-resolved photoemission, *Physical Review B*, **88** (2013) 035108.

[30] M. Chhowalla, H.S. Shin, G. Eda, L.J. Li, K.P. Loh, H. Zhang, The chemistry of two-dimensional layered transition metal dichalcogenide nanosheets, *Nature Chemistry*, **5** (2013) 263.

[31] K. Rossnagel, N. Smith, Spin-orbit splitting, Fermi surface topology, and charge-density-wave gapping in *2H−$TaSe_2$*, *Physical Review B*, **76** (2007) 073102.

[32] R.A. Craven, S.F. Meyer, Specific-heat and resistivity near charge-density-wave phase-transitions in *2H-$TaSe_2$* and *2H-TaS_2*, *Physical Review B*, **16** (1977) 4583.

[33] Y. Ge, A.Y. Liu, Effect of dimensionality and spin-orbit coupling on charge-density-wave transition in *2H-$TaSe_2$*, *Physical Review B*, **86** (2012) 104101.

[34] F. Flicker, J. van Wezel, Charge order from orbital-dependent coupling evidenced by *$NbSe_2$*, *Nature Communications*, **6** (2015) 7034.

[35] A. Soumyanarayanan, M.M. Yee, Y. He, J. van Wezel, D.J. Rahn, K. Rossnagel, E.W. Hudson, M.R. Norman, J.E. Hoffman, Quantum phase transition from triangular to

stripe charge order in *$NbSe_2$*, *Proceedings of the National Academy of Sciences of the United States of America*, **110** (2013) 1623.

[36] R.L. Withers, L.A. Bursill, Comments on the neutron-scattering study of the charge-density-wave - periodic-structural-distortion transition in *2H-$TaSe_2$* and *2H-$NbSe_2$* by Moncton, Axe, and Disalvo, Physical Review B, 26 (1982) 1469.

[37] A. König, K. Koepernik, R. Schuster, R. Kraus, M. Knupfer, B. Büchner, and H. Berger, Plasmon evolution and charge-density wave suppression in potassium intercalated $2H - TaSe_2$, *Europhysics Letters*, **100** (2012) 27002.

Chapter 4

ARPES Study on the Type-II Dirac Semimetal *1T-$PtSe_2$*

Recent discoveries of topological semimetals (TSMs) and topological insulators (TIs) show a tremendous triumph of realization of elementary (quasi)particles in low-energy condensed-matter systems [1-7]. Three-dimensional (3D) and two-dimensional (2D) massless Dirac fermions are experimentally observed in the bulk of topological Dirac semimetals (TDSMs, e.g., *Na_3Bi* [3] and *Cd_3As_2* [2]) and on the surface of TIs (e.g., *Bi_2Se_3* [7] and *Bi_2Te_3* [1]). The Weyl fermions observed in the topological Weyl semimetals (TWSMs, e.g., *TaAs* [4]) fill in the fermion table. Interestingly, since condensed-matter system could violate the stringent Lorentz symmetry, TSMs can potentially host quasiparticles beyond the standard model [8]. The first Lorentz-symmetry breaking Weyl fermion was discovered in the type-II TWSM *W*(*Mo*)*Te_2* [5, 8]. Its chirality-degenerate counterpart, type-II Dirac fermions have been theoretically proposed in *1T* structured group X transition-metal dichalcogenides (TMDs) [9] but remained experimentally elusive. Although preliminary angle-resolved photoemission spectroscopy (ARPES) results for *1T-$PdTe_2$* [10], *1T-$PtTe_2$* [11], and *1T-$PtSe_2$* [12] show consistency with the *ab initio* calculations, the signature of a strongly tilted conic dispersion along the k_z axis remains unclear and requires further experiments. Furthermore, the topologically nontrivial, exotic surfaces states (SSs) and related inversion of bulk band ordering for this material family are currently poorly understood and need careful scrutiny.

1T-$PtSe_2$ is a promising pristine type-II TDSM candidate compound for the proposed research, not only for being adjacent to various exotic topological states, such as TWSMs and TIs, but also for its application potentials. It has long been reported to have high performance in photocatalysis [13-15] and electrocatalysis [16] or as high-mobility field effect transistor (FET) material [17]. A novel Rashba effect discovered in centrosymmetric monolayer *1T-$PtSe_2$* might lead to new applications in electrically tuneable spintronics [18]. To understand the electronic origin of these desired properties [13, 14, 19, 20], a thorough investigation of its unique electronic structures and intrinsic topological nature is required.

In this chapter, we report our systematic study on the electronic structure of the bulk crystal *1T-$PtSe_2$* in the full 3D Brillouin zone (BZ) by high-resolution ARPES. Our results show clear semimetallic character from Fermi surface (FS) mapping. By carrying out broad-range photon-energy-dependent measurements, we are able to identify electronic states originating from both the bulk and the surface. A pair of well-resolved tilted linear crossings along k_z axis provide strong experimental evidence for type-II Dirac fermions. We also notice conic SSs around time-reversal-invariant momenta (TRIM) $\bar{\Gamma}$ and $\bar{M}$, which can be nicely reproduced by our (and previous) *ab initio* calculations [9]. We further confirm the nontrivial topology of the SSs by detailed analysis of eigenstates of the bulk states (BSs) and the intricate band inversion. Our results provide essential experimental evidence for type-II Dirac fermions in *1T-$PtSe_2$* as well as its topological properties.

4.1 Crystal Structure and Symmetry

$PtSe_2$ is a layered TMD crystallized in *1T* structure (see also in section 2.1.2). As illustrated in Fig. 4.1(a), each layer has a *Se-Pt-Se* sandwich structure with the centre *Pt* octahedrally surrounded by *Se* atoms. The lattice constants of the single crystal *1T-$PtSe_2$* are

confirmed by x-ray diffraction method [see Fig. 4.1(c)] to be $a = b = 3.72$ Å, $c = 5.06$ Å. Compared to *2H-TaSe*$_2$ ($c = 6.35$Å), *1T-PtSe*$_2$ has stronger interlayer coupling. The natural cleavage plane is the (001) surface with *Se* termination.

The space group of *1T-PtSe*$_2$ is *P*-3*m*1 (see also in section 2.1.2) and its hexagonal BZ is shown in Fig. 4.1(b). The crystal structure together with the absence of any magnetic order respects both inversion symmetry (IS) and time-reversal symmetry (TRS). The additional crystalline symmetry including a double point group of threefold rotation symmetry is necessary to protect the bulk Dirac point (BDP) [21, 22]. It is clearly shown that *1T-PtSe*$_2$ hosts C_{3v} symmetry about the *c* axis in the real space [see Fig. 4.1(a)] and correspondingly about k_z in the momentum space [see Fig. 4.1(b)] where the DP reside (not shown).

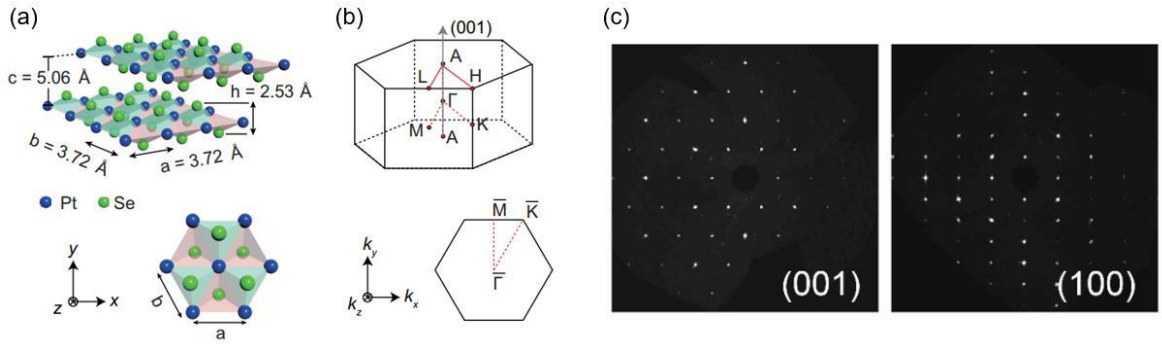


Fig. 4.1 Crystal structure and Brillouin zone (BZ) of *1T-PtSe*$_2$. (a) Crystal structure of *1T-PtSe*$_2$ showing the stacking of *Se-Pt-Se* planes. The lattice constant is indicated with the top view of the most probable cleavage plane shown in the lower panel. (b) BZ of *1T-PtSe*$_2$ with high-symmetry points indicated. Projected (001) surface BZ in the $k_x - k_y$ plane is shown in the lower panel. (c) X-ray diffraction pattern of (001) (left) and (100) (right) surface, respectively.

We compare the crystal structure of *1T-PtSe*$_2$ with that of the type-II TWSM *MoTe*$_2$. *MoTe*$_2$ crystallizes in the T_d structure (space group *Pmn*21, also see in section 2.1), which can be regarded as 2×1 in-plane Peierls distortion of *1T* structure breaking both the IS and the uniaxial rotational symmetry [5, 8, 23, 24]. Thus, the recovered crystalline symmetries in *1T-PtSe*$_2$ can merge a pair of Weyl points (WPs) into a DP, making it a candidate of type-II TDSM.

4.2 Band Structure in the 3D BZ

4.2.1 Determination of the high-symmetry points along k_z

To map the complete band structure over the 3D BZ, it is important to determine the high-symmetry points along k_z as elaborated in section 1.2.2. During the photon-energy-dependent measurement, the sample is aligned to $\Gamma - M/A - L$ direction. As shown in Fig. 4.2(a), from the energy contour at $E = E_F - 3.0$ eV, one can clearly identify periodic band features along the k_z direction, which allows us to determine the high-symmetry points in the BZ and extract the k_z value of each cut measured with certain photon energy.

The two cuts measured along $L - A - L$ ($k_z = \pi/c$, measured with $h\nu = 100$ eV) and $M - \Gamma - M$ ($k_z = 0$, measured with $h\nu = 75$ eV) are plotted in the left panel of Figs. 4.2(b) and (c), respectively. The dispersions of the three VBs below E_F are significantly different between these two high symmetry planes. One can observe that the top valence has a "Λ" shape at $k_z = 0$ plane but has a "V" shape at $k_z = \pi/c$ plane, as in agreement with the calculation shown in the right panel of Figs. 4.2(b) and (c). This comparison shows that we are able to accurately determine the k_z location of each cut and probe the full electronic structure of *1T-PtSe*$_2$ in the 3D BZ.

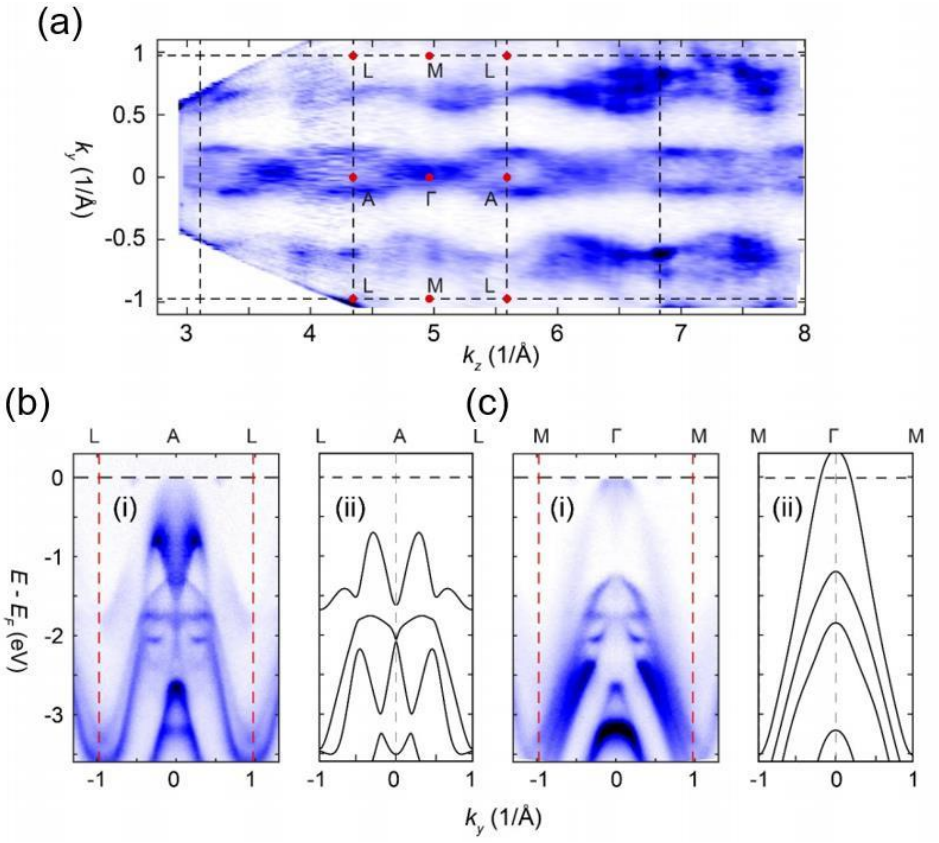


Fig. 4.2 k_z-dependent measurement via continuously changing photon energy of *1T-PtSe₂*. (a) Constant energy contour at 3.0 eV below E_F in the $k_{\parallel}$ vs. k_z plane. Identified high symmetry points are labelled. (b) High symmetry $L - A - L$ cut (left) and corresponding *ab initio* calculation (right). (c) High symmetry $M - \Gamma - M$ cut and corresponding *ab initio* calculation.

4.2.2 General band structure

The general band structure of *1T-PtSe₂* is shown in Fig. 4.3. The ARPES spectrum [see Figs. 4.3(a) and (c)] agrees with the *ab initio* calculations [see Figs. 4.3(b) and (d)] and confirms the semimetal nature. The FS [see Figs. 4.3(a) and (b)] consists of a hole pocket at the BZ centre $\bar{\Gamma}$, and small electron pockets along $\bar{\Gamma}\bar{M}$ and at the BZ corner $\bar{K}$. The detailed FS topology will be presented in section 4.2.3. Within 3 eV below E_F, there are four VBs,

labeled as v_1 to v_4 from top to bottom [see Fig. 4.3(d)]. Despite the layered structure, *1T-PtSe*$_2$ reveals a very 3D band structure (e.g., the v_1 band disperses strongly along the k_z direction). Band dispersions measured by ARPES [see Fig. 4.3(c)] show general agreement with our *ab initio* calculations except for additional small electron pocket along $\Gamma - M$ and $A - L$, which is probably due to the finite k_z resolution as the conduction-band bottom along $\bar{\Gamma}\bar{M}$ lies between $k_z = 0$ and $k_z = \pi/c$ planes [not shown in Fig. 4.3(d)]; also see Appendix E. By comparison with the BS calculations, the sharp features marked by the dashed green lines in the ARPES spectrum [see Fig. 4.3(c)] are identified as SSs, which is further discussed in section 4.2.4.

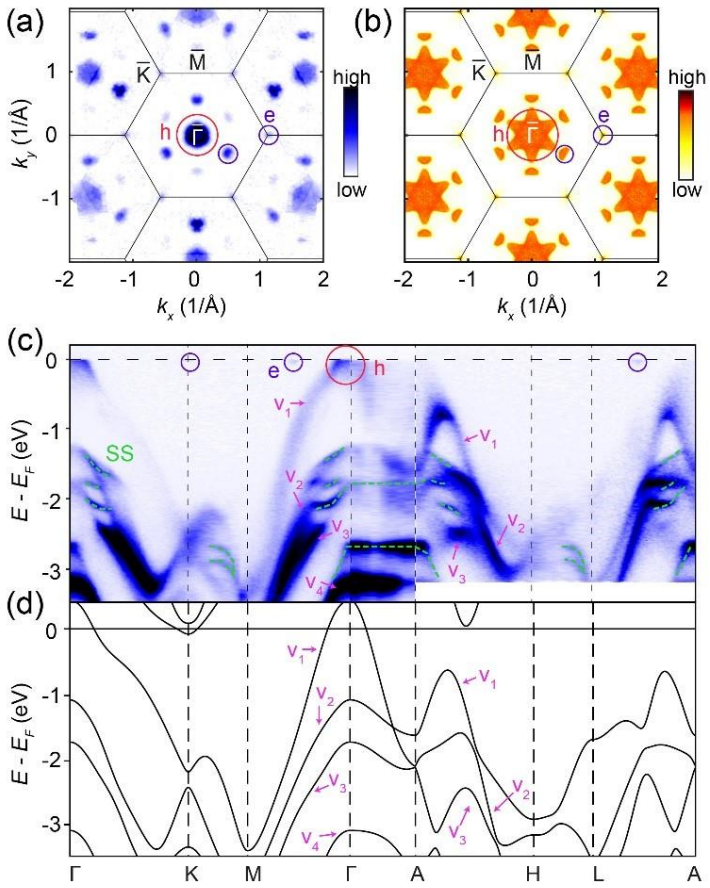


Fig. 4.3 General electronic band structure of *1T-PtSe*$_2$. (a) Broad-range photoemission Fermi energy contour from ARPES data, showing the correct symmetry and characteristics of semimetallic FSs. Electron and hole pockets are marked by purple and red circles. (b) Corresponding Fermi energy contour from surface-projected *ab initio* calculation in the same range as (a). Comparison between (c) the measured band dispersions and (d) corresponding calculated BSs along the high-symmetry $\Gamma - K - M - \Gamma - A - H - L - A$ direction. SSs are highlighted by dashed green lines. Electron and hole pockets are marked with purple and red circles as in (a). The VBs in (d) are labelled as v_i $(i = 1,2,3,4)$ (magenta arrows).

4.2.3 Detailed band structure near E_F

The (001) FS consists of a hole pocket at BZ centre $\bar{\Gamma}$, small electron pockets along $\bar{\Gamma}\bar{M}$ and at BZ corner $\bar{K}$. Although the conduction-band-bottom is not at the high symmetry k_z plane (see Appendix E), the electron pocket can be observed due to the k_z broadening effect. From Fig. 4.4(c), we can clearly observe the hole and electron pockets via isoenergy contours from $h\nu = 132$ eV measurement which is in good agreement with the *ab initio* calculation of $k_z = 0$ plane. In contrast, measurement at $h\nu = 162$ eV for $k_z = \pi/c$ [see Figs. 4.4(e) and (f)] show less density of states near E_F. The weak hole pocket at the BZ centre $\bar{\Gamma}$ and electron pockets along $\bar{\Gamma}\bar{M}$ might due to the projection from neighbouring k_z. The isoenergy contours at $h\nu = 162$ eV are also significantly different from their counterparts at $h\nu = 132$ eV. It shows two concentric hole and electron pockets at the BZ centre below $E_b = 0.6$ eV, while there is only a hole pocket in the BZ centre around the $k_z = 0$ plane.

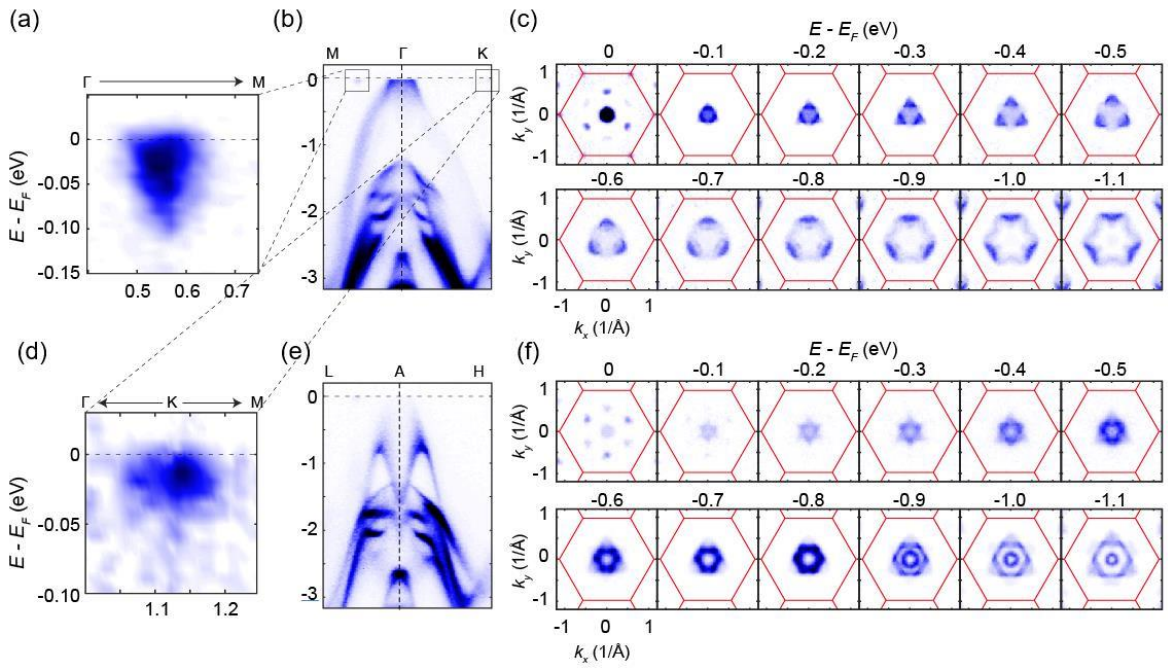


Fig. 4.4 Detailed band structure near E_F of *1T-PtSe*$_2$. (a) Zoomed in area of the small electron pocket along $\bar{\Gamma}\bar{M}$ direction as indicated in (b). (b) ARPES measurement along $M - \Gamma - K$ direction measured at $h\nu = 132$ eV. (c) ARPES isoenergy contours from E_F to $E = E_F - 1.1$ eV measured at $h\nu = 132$ eV. (d) Zoomed-in area of the small electron pocket at BZ corner $\bar{K}$ as indicated in (b). (e) ARPES measurement along $L - A - H$ direction measured at $h\nu = 162$ eV. (f) ARPES isoenergy contours from E_F to $E = E_F - 1.1$ eV measured at $h\nu = 162$ eV.

4.2.4 Distinguish surface and bulk states

Non-k_z-dispersive SSs are distinguished from k_z-dispersive BSs by continuously changing photon energy [see Figs. 4.5(a) and (b)]. Following this principle, we can observe a SS (labelled as α) between v_1 and v_2 and two more (labelled as β and γ) between v_2 and v_3 if cutting through the momentum slight off $\bar{\Gamma}$ [see Fig. 4.5(b)]. Another high-binding-energy SS at $\bar{\Gamma}$ below v_3 is observed with strong intensity [see Fig. 4.5(a)]. The sharp (i.e., not affected by the k_z broadening effect) peaks with strong spectral weight of these features further support their surface origin. From high-symmetry cuts [Figs. 4.5(d) and (e)] and 3D intensity plot of the ARPES spectrum [Figs. 4.5(j) and (k)] at the $k_z = 0$ and $k_z = \pi/c$ planes, we can see that the upper three SSs between v_1 and v_3 dominate the spectral weight in momentum space slightly off $\bar{\Gamma}$ ($k \approx 0.2$ Å^{-1}), while they merge into bulk at ($k \approx 0$) and away from ($k \gtrsim 0.5$ Å^{-1}) the BZ centre $\bar{\Gamma}$. In constant-energy contours measured at these two high-symmetry k_z planes [see Fig. 4.5(f)], the SSs (as highlighted by the green arrows) could also be clearly observed, showing negligible k_z variation.

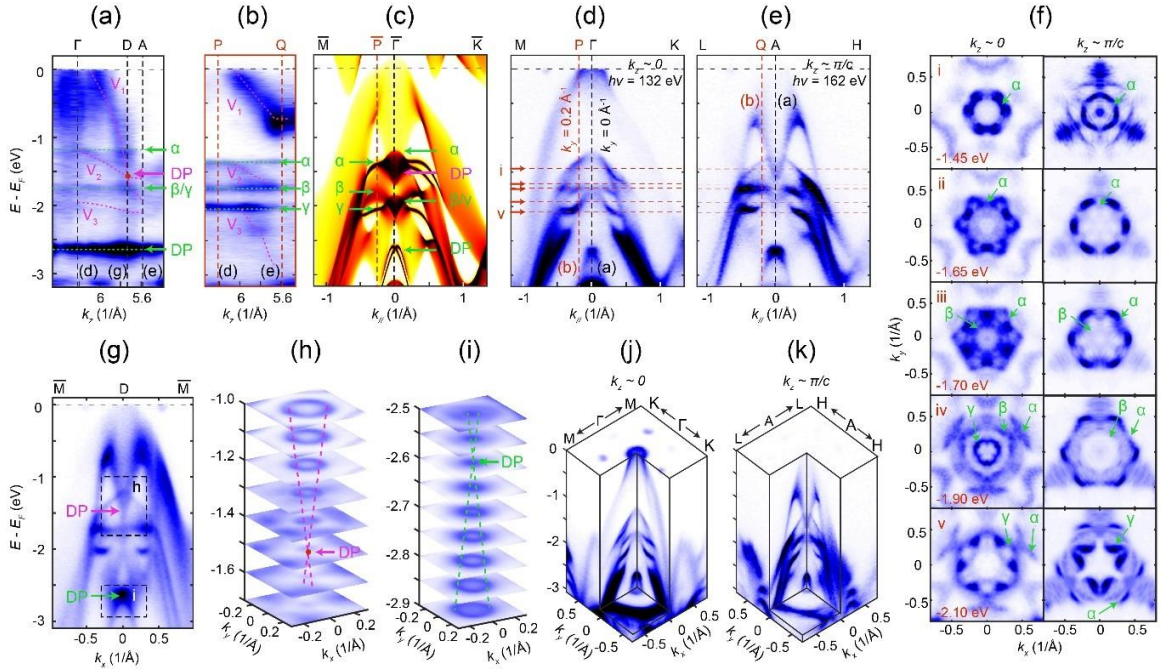


Fig. 4.5 Bulk and surface states in *1T-PtSe*$_2$. (a), (b) ARPES data along $\Gamma - A$ ($k_y = 0$) and $P - Q$ ($k_y = 0.2$ Å^{-1}) as indicated in (d) and (e), showing a strong k_z dependence in electronic band dispersion. Bulk states (BSs) and surface states (SSs) (including α, β and γ) are marked by dashed magenta and green lines, respectively. The type-II BDP formed by the crossing between v_1 and v_2 is indicated by the magenta arrow, whereas the surface Dirac point (SDP) between v_3 and v_4 is indicated by the green arrow (see text). (c) *Ab initio* calculated projected surface intensity along the $\bar{M} - \bar{\Gamma} - \bar{K}$ direction. SSs, BDP, and SDP are marked with the same colour as in (a) and (b). ARPES data (d) along $M - \Gamma - K$ at the $k_z = 0$ plane measured with a photon energy of 132 eV and (e) along $L - A - H$ at the $k_z = \pi/c$ plane measured with a photon energy of 162 eV. (f) ARPES energy contours at $k_z = 0$ plane (upper panel) and the $k_z = \pi/c$ plane (lower panel), respectively. Energy levels (i)-(v) are indicated by dashed red lines in (d) and (e). SSs are marked by green arrows. (j), (k) 3D ARPES intensity plot measured at photon energies of 132 eV and 162 eV for the $k_z = 0$ and $k_z = \pi/c$ planes, respectively.

Both bulk and surface electronic structures are well reproduced in our *ab initio* calculation [see Fig. 4.5(c)]. The type-II Dirac fermions shows its first hint in the k_z-dependent measurement [see Fig. 4.5(a)] where the dispersive v_1 band intersects with the less dispersive v_2 band at $E_D \approx E_F - 1.5$ eV and $k_D \approx 0.72\pi/c$. Another topological feature around $\bar{\Gamma}$ is a surface Dirac cone at high binding energy connecting v_3 and v_4 [see Figs. 4.5(c)-(e)]. Detailed band structure of the type-II Dirac cone and the topological nature of the SSs are further discussed in sections 4.3 and 4.4, respectively.

4.3 Type-II Dirac Cone

4.3.1 Visualization of the four-dimensional type-II Dirac cone

To map the whole (3+1)-dimensional (k_x, k_y, k_z, E) type-II Dirac cone, we carried out detailed photon-energy-dependent measurements in the range from 18 to 33 eV along the $\bar{\Gamma} - \bar{M}$ direction [see Fig. 4.6(c)]. For a better understanding of the four-dimensional (4D) structure, we project the data to 3D and 2D subspaces. Although the k_z dispersion suffers from the intrinsic broadening effect due to the relatively low photon energies, our ARPES spectra show good agreement with the calculation, which helps us locate the crossing point [type-II BDP, labelled as *D* in Figs. 4.5(a), 4.6(f) and 4.6(h)] between the v_1 and v_2 bands. Around the BDP, a highly anisotropic tilted conic dispersion is shown in the projection of the electronic structure in the (k_y, k_z, E) space [see Figs. 4.6(b) and (e)]. The VBs v_1 and v_2 touch at $k_z \approx 0.72\pi/c$ and quickly get separated as the slice moves away from *D* along k_z [see Figs. 4.6(c)]. Similarly, the k_y evolution [see Fig. 4.6(f)] shows that these two bands become degenerate at $k_y = 0$ and then gradually get separated with increased k_y.

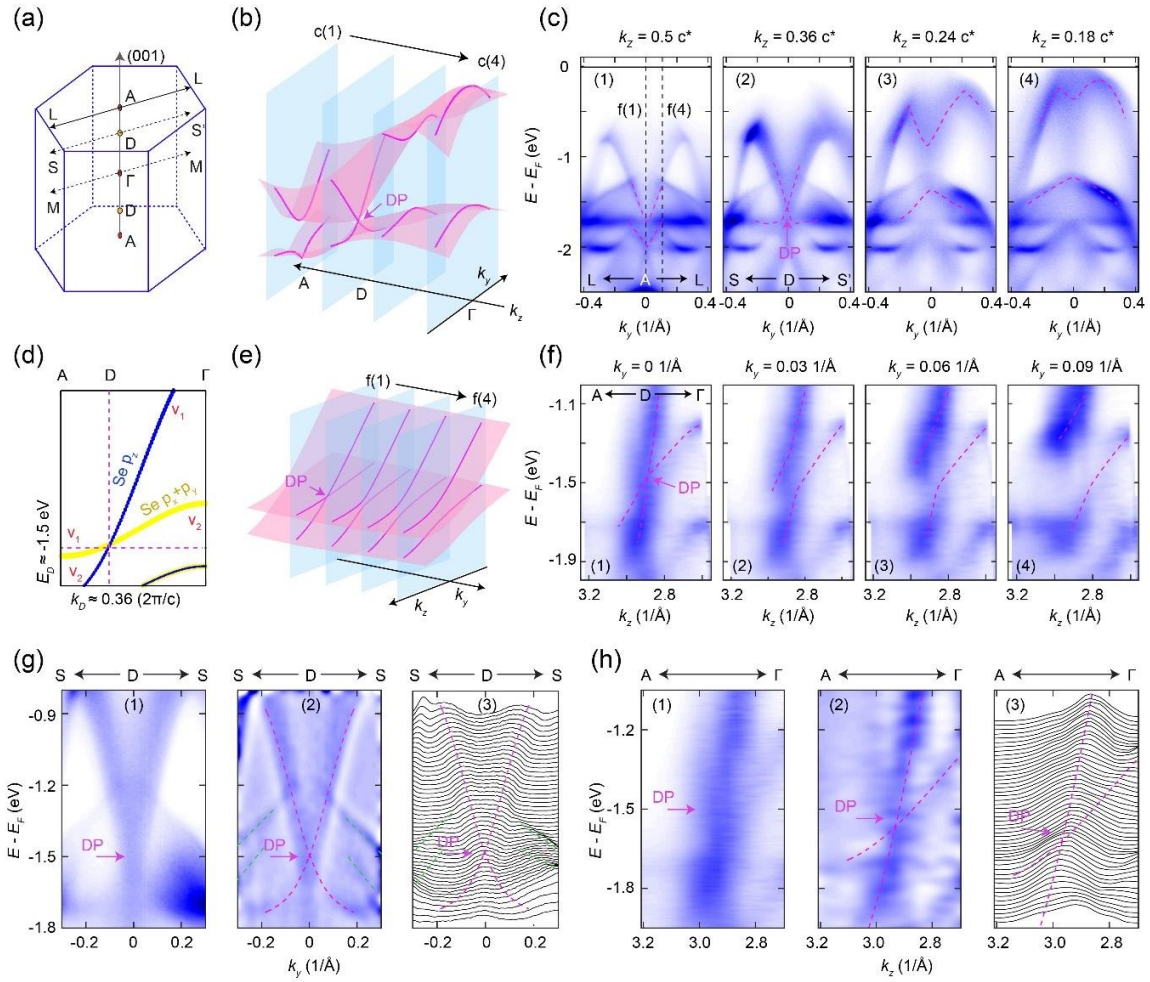


Fig. 4.6 Type-II Dirac cone in *1T-PtSe*$_2$. (a) Schematic of bulk BZ showing a pair of BDPs at $k_D = \pm 0.36\ (2\pi/c)$ along the k_z axis. (b) and (e) Projected Dirac cone reconstructed from the *ab inito* calculation in (k_y, k_z, E) space. The light blue planes (c1)-(c4) and (f1)-(f4) indicate ARPES measurements that slice through the Dirac cone at different $k_z(k_y)$ positions. (d) *Ab initio* calculated orbital-projected bulk dispersion showing that the type-II BDP is formed by v_1 and v_2 with a band inversion between *Se* $\boldsymbol{p_z}$ and $\boldsymbol{p_x + p_y}$. (g) Zoomed-in in-plane type-II Dirac band dispersion along k_z measured at $h\nu = 24$ eV (g1), corresponding second-derivative plots (g2), and momentum-distribution-curve (MDC) stacking plots (g3). (h) Zoomed-in type-II Dirac band dispersion along k_z measured at $h\nu = 18 - 33$ eV (h1), corresponding second-derivative plots (h2), and MDC stacking plot (h3). Calculated bulk band dispersions (dashed magenta lines) are appended on (g) and (h).

Closer scrutiny of the type-II DP by zoomed-in high-resolution cuts along the k_y and k_z directions is presented in Figs. 4.6(g) and (h). With the help of second-derivative and momentum-distribution-curve (MDC) plots, the experimental dispersion shows excellent agreement with *ab initio* calculation (dashed magenta lines), thus strongly supporting the existence of the type-II Dirac fermion. However, the tail-like spectral weight below the DP is caused by the intrinsic k_z broadening.

The distinction between type-I and type-II TDSMs also lies in the FS topology at E_D. In contrast with type-I DSMs (e.g., Na_3Bi [3] and Cd_3As_2 [2]) hosting pointlike FS in all momentum planes at E_D, type-II DSMs host DPs at the boundary of electron and hole pockets in certain momentum planes [e.g., the $k_x - k_z$ plane as shown in Fig. 4.7(d)] while they share similar in-plane ($k_x - k_y$) pointlike FSs [see Fig. 4.7(a)]. Our ARPES measurement on the type-II DSM *1T-*$PtSe_2$ confirms this scenario. Dirac band dispersion in $k_x - k_y - E$ space is mapped out using photon energy of 24 eV, as shown in Figs. 4.7(b) and (c). 3D visualization of the type-II Dirac cone in $k_x - k_z - E$ space is obtained by continuously changing photon energy as shown in Figs. 4.7(e) and (f). From the energy contour evolution, one can see that the electron pocket shrinks while the hole pocket grows when the binding energy increases near E_D. They finally touch at E_D, which is regarded as a critical energy in topological Lifshitz transition, giving rise to new physics [8, 25].

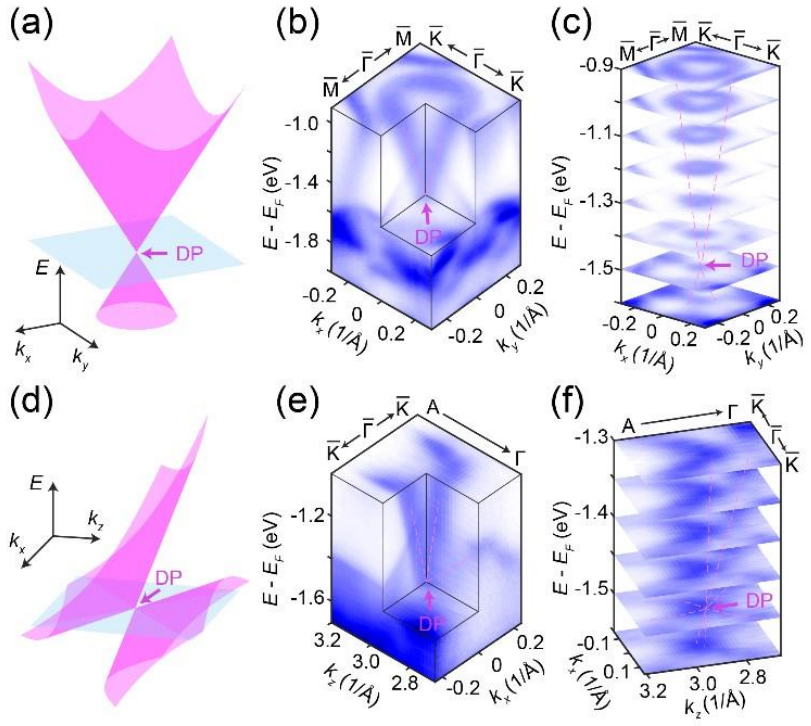


Fig. 4.7 3D visualization of type-II Dirac cone. (a) Schematic of type-II Dirac cone projected on $k_x - k_y - E$ space. (b) 3D ARPES intensity map measured at $h\nu = 24$ eV which slices through the type-II BDP. (c) ARPES energy contours of (b). (d) Schematic of type-II Dirac cone projected on $k_x - k_z - E$ space. (e) 3D k_z-dependent intensity map measured at $h\nu = 18 - 33$ eV. (f) ARPES energy contours of (e).

4.3.2 Anisotropy of type-II bulk Dirac cone in *1T-PtSe*$_2$

Figure. 4.8 shows detailed in-plane and along-k_z dispersion near the BDP. The in-plane dispersion, as shown in Fig. 4.8(a) and (b), illustrates the linear band crossing similar to conventional type-I TDSM. The slope of these two band dispersions (or the Fermi velocity of the Dirac fermion if E_F is tuned to E_D) at the BDP along $D - S$ direction is $\frac{1}{\hbar}\frac{dE_k}{dk} \approx \pm 6.4 \times 10^5\ m/s$. In contrast, the band dispersion along k_z show the strong anisotropic nature of the type-II Dirac cone. The slope of the flat and the steep bands at the BDP along

$A-\Gamma$ direction is fitted by EDCs and MDCs to be 9.1×10^4 m/s and 1.6×10^6 m/s, respectively.

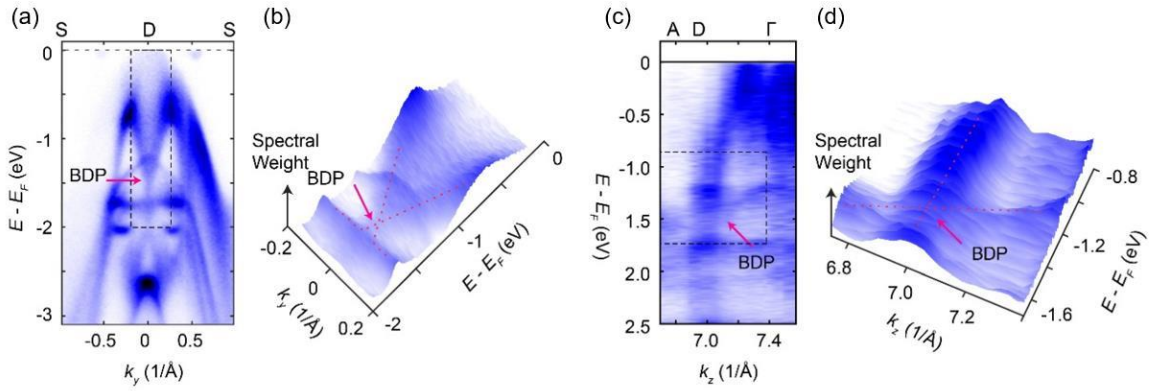


Fig. 4.8 Anisotropy of type-II bulk Dirac cone in *1T-PtSe₂*. (a) ARPES cut of the BDP along $S-D-S$ direction. (b) 3D spectral weight distribution plot of the area indicated by the dashed rectangle in (a). (c) ARPES cut of the BDP along $A-D-\Gamma$ direction. (d) 3D spectral weight distribution plot of the area indicated by the dashed rectangle in (c).

4.4 Topological Surface States

4.4.1 Topological Surface State at $\bar{\Gamma}$

In 3D centrosymmetric TIs (e.g., Bi_2Se_3 [7] and Bi_2Te_3 [1]), strong SOC results in the formation of an inverted band gap between the CB and VB of opposite parities [26]. Robust SSs connecting BSs at TRIM is one of the most prominent signatures of the nontrivial topological nature. Similarly, in TSMs, topological SSs could survive when mixing with the BSs and stabilize in the local inverted band gap well below E_F [27]. Hence, a direct observation of Dirac-like SSs connecting bulk continuum at TRIM $\bar{\Gamma}$ and $\bar{M}$ strongly indicates the nontrivial band structure of *1T-PtSe₂*.

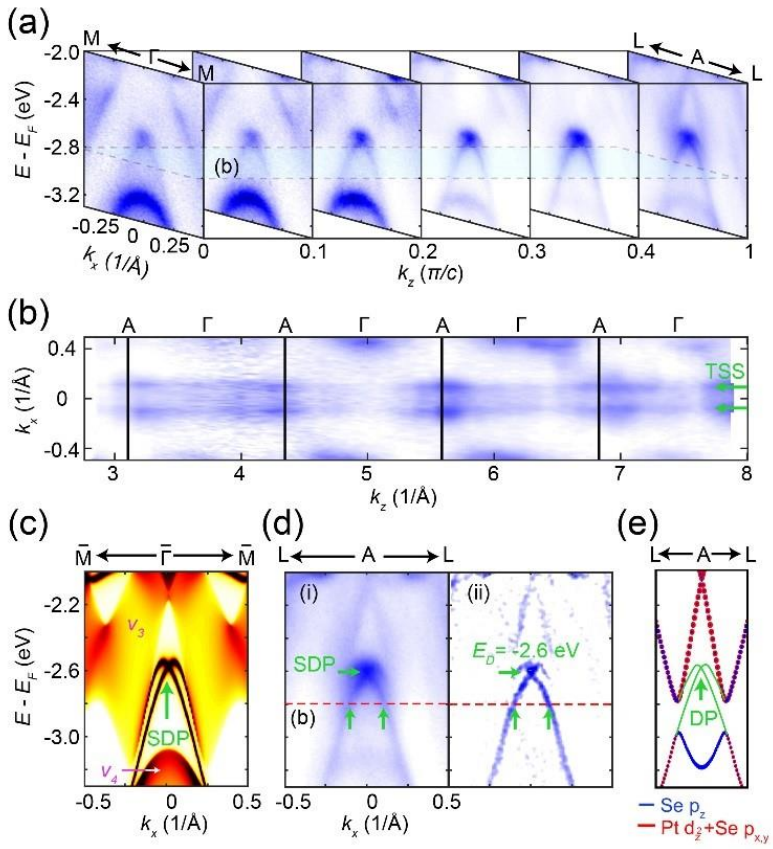


Fig. 4.9 TSSs at $\bar{\Gamma}$. (a) The k_z-dependent ARPES data of TSSs covering half of the BZ shows a 2D non-dispersive nature. The light-blue plane indicates the energy level of the ARPES energy contour shown in (b). (b) The k_z-dependent ARPES energy contour covering over four BZs at $E = E_F - 2.8$ eV, indicated by the blue plane in (a) and the dashed red lines in (d). TSSs are marked by green arrows. (c) *Ab initio* calculated projected surface intensity showing the topological nontrivial SSs in the local band gap between v_3 and v_4 bulk-state continuum. (d) ARPES data (i) and corresponding curvature [28] plot (ii) (see also in section 1.2.3) along $L - A - L$ in the same momentum-energy range as (c). (e) Schematic plot of TSSs in the inverted band gap.

Figure 4.9 summarizes the structure of TSSs at $\bar{\Gamma}$. The linear crossing at $E_D^{\Gamma} = E_F - 2.6$ eV is nondispersive along k_z [see Figs. 4.9(a) and (b)], which strongly supports its

surface origin. Band dispersion measured along $L - A - L$ [see Fig. 4.9(d)] is consistent with our calculation [see Fig. 4.9(c)] where the surface Dirac point (SDP) resides in the local inverted band gap between v_3 and v_4.

4.4.2 Topological Surface State at $\bar{M}$

We also spot flowerlike SSs at $\bar{M}$ connecting v_1 and the bulk continuum of v_2 and v_3 [see Fig. 4.10]. Band dispersions measured at two high-symmetry k_z along $K - M - K$ ($h\nu = 132$ eV) and $H - L - H$ ($h\nu = 162$ eV) confirm the surface origin of these states [see Figs. 4.10(a) and (b)]. The SSs form a double-arc-like feature in constant-energy-contours above the SDP [see Figs. 4.10(d)-(f)]. Our experimental results are perfectly reproduced by *ab initio* calculation showing that these SSs are topologically nontrivial and they cross at $\bar{M}$ and merge into upper v_1 and lower $v_2 + v_3$ BSs. The SDP is buried well beneath E_F at $E_D^M = E_F - 3.4$ eV. These additional topological surface states (TSSs) have not been discussed in previous works and, in tandem with the TSSs at $E_D^\Gamma = E_F - 2.6$ eV, they suggest a rich parity-inversion picture in 1T-$PtSe_2$, which we discuss more in section 4.5.

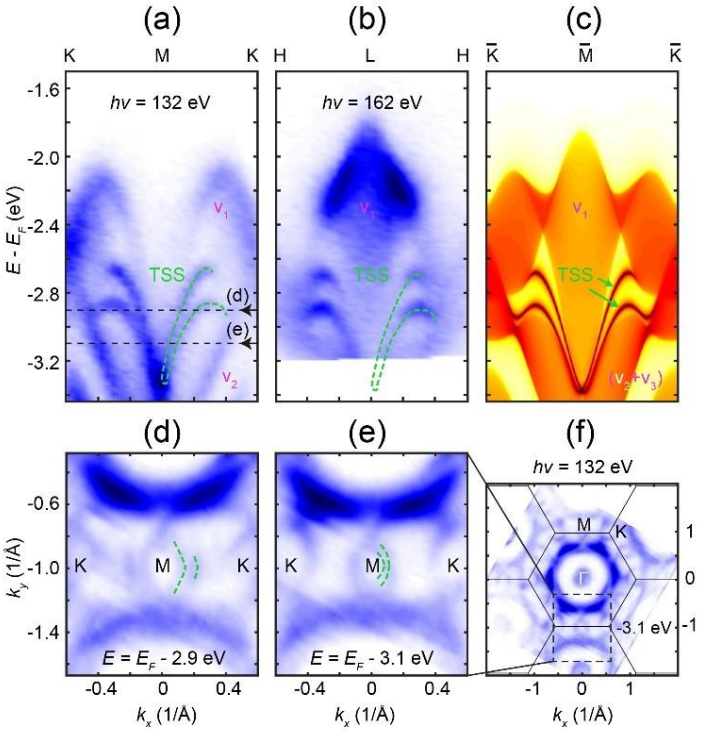


Fig. 4.10 TSS at $\bar{M}$. (a), (b) ARPES data of band dispersions along (a) $K - M - K$ measured at $h\nu = 132$ eV and (b) $H - L - H$ measured at $h\nu = 162$ eV. The flowerlike TSSs marked by dashed green lines, show a nondispersive nature along k_z. (c) Corresponding *ab initio* calculated projected surface intensity along $\bar{K} - \bar{M} - \bar{K}$ in the same energy range as (a) and (b), showing great consistency with ARPES data. The TSSs reside in the inverted band gap between v_1 and $v_2 + v_3$. (d) ARPES energy contours at $E = E_F - 2.9$ eV measured by $h\nu = 132$ eV. (e) Same as (d) but at $E = E_F - 3.1$ eV. The energy levels of (d) and (e) are indicated by the dashed black lines in (a). TSSs are marked by dashed green lines in (d) and (e). (f) Zoomed-out ARPES energy contour of (e).

4.5 Interpretation of Topological Band Structure

To understand the topological nature of this centrosymmetric system, we have calculated the parity eigenvalues of the four VBs v_i $(i = 1,2,3,4)$ at four TRIM (Γ, A, M, L) and found

a rich parity-inversion picture in *1T-PtSe*$_2$ which consistently explains the coexistence of the BDPs and multiple SDPs.

4.5.1 Interpretation of the type-II bulk Dirac point

We find the type-II BDP in *1T-PtSe*$_2$ to be of a topological origin; the BDP can be viewed as a critical point of a topological phase transition between $k_z = 0$ and $k_z = \pi/c$ planes. As VBs v_1 and v_2 are fully gapped at the two planes and they both satisfy the TRS, a Z_2 invariant therefore can be defined for each plane as usual for the QSH states. By using both the parity production [29] and Wilson loop schemes [30], we found that Z_2 takes different values at the two planes (1 for $k_z = 0$ and zero for $k_z = \pi/c$, respectively), revealing their different topological natures. As k_z continously varies between zeros and π/c, there must be a critical value of k_z at which a topological phase transition occurs. As a consequence, the gap between bands v_1 and v_2 closes at this value of k_z, featuring a topological BDP [21].

4.5.2 Interpretation of the TSSs and band inversions

We find rich band and parity inversion in *1T-PtSe*$_2$ which result in the multiple TSSs residing at $\bar{\Gamma}$ and $\bar{M}$ (see Fig. 4.11). The hybridization between states with the same mJ is examined along k_z for $\Gamma - A$ and $M - L$, respectively. In contrast to the band inversions involving only two neighboring bands which is often seen in most TIs, *1T-PtSe*$_2$ presents an intricate band ordering of four VBs. By carefully analyzing the band crossings and their hybridizations, we find a consistent picture that simultaneously explains the robustness of the BDP as well as the appearance of the multiple SDPs. Although like TIs, SOC gaps the forbidden band crossings and causes the formation of TSSs, the inverted band orders

directly result from the crystal field of *1T-PtSe*$_2$ [31]. The joint role of both crystal symmetry and SOC played in this complicated structure requires further investigation and might provide an insight for new classification of topological materials.

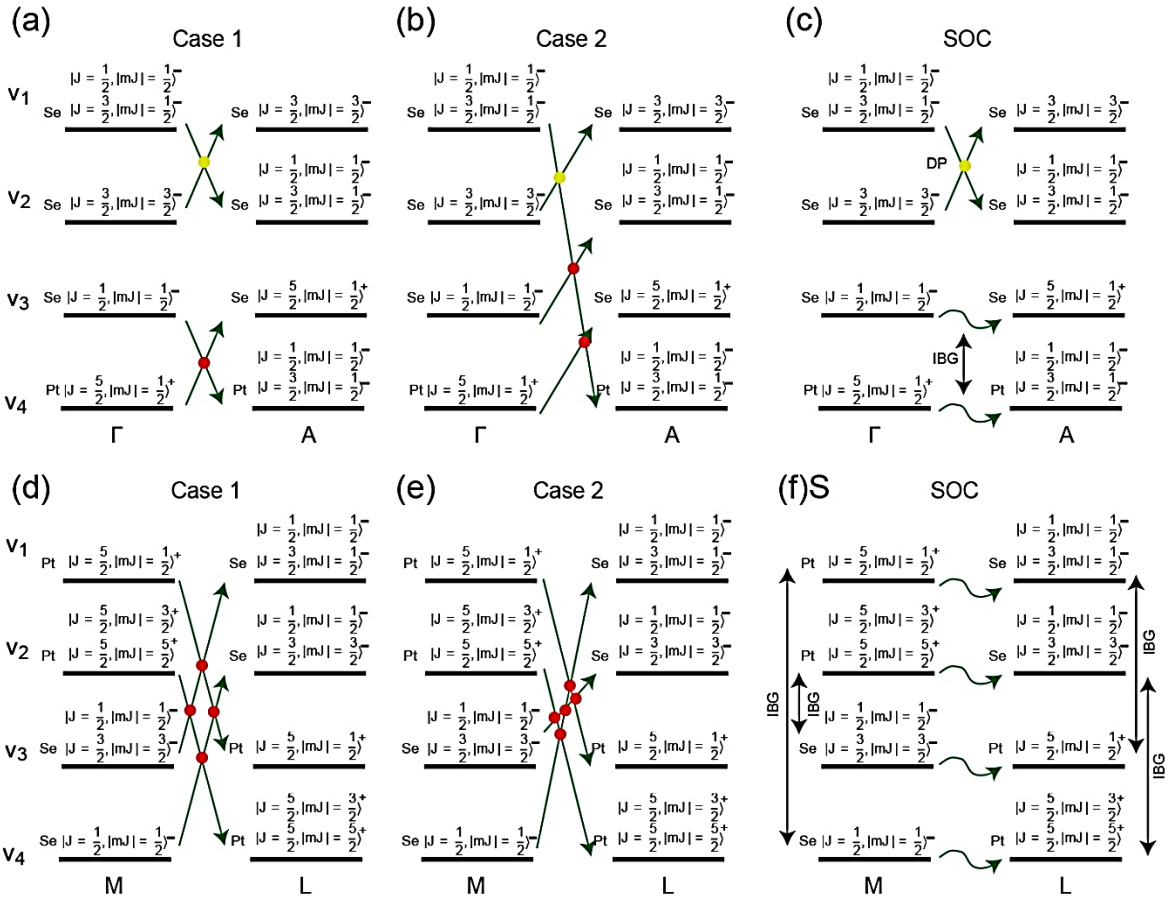


Fig. 4.11 Schematic of bulk band hybridizations and inversion along k_z. (a-c) Bulk band hybridization along $\Gamma - A$. The possible connection between states of same mJ leads to two cases (a) and (b). The crossings indicated by red dots will be gapped out whereas the one indicated by yellow dots remain gapless after SOC is introduced in (c). The inverted band order between v_3 and v_4 give rise to the surface Dirac cone at $\bar{\Gamma}$ at $E = E_F - 2.6$ eV. (d-f) Bulk band hybridization along $M - L$. Both cases (d) and (e) lead to two band inversions either between v_1, v_3 and v_2, v_4, or between v_1, v_4 and v_2, v_3. (f) These two inversions should give rise to two surface Dirac cones at $\bar{M}$. The upper one is experimentally observed at $E = E_F - 3.4$ eV.

Method

Sample Preparation: $PtSe_2$ single crystals were prepared by the flux-growth technique using excess Pt. In a typical synthesis, Pt and Se pieces were mixed according to the composition $Pt_{45}Se_{55}$ and kept in an alumina crucible. The content was sealed inside a quartz tube under vacuum and heated to 1230 ℃ at a rate of 50 ℃/h in a box furnace. The temperature was maintained for 5 h, followed by slow cooling until 1100 ℃ at a rate of 1.5 ℃/h. At this temperature, the excess liquid was decanted off and the furnace was cooled rapidly to room temperature. Shining agglomerated layered single crystals were collected from the bottom of the crucible.

ARPES: ARPES measurements were performed at the beamline I05 high-resolution branch (Diamond Light Source, UK) with a Scienta R4000 analyzer and beamline APE (Elettra synchrotron) with a Scienta DA30 analyzer. The photon-energy ranges for DLS and APE are 20-220 eV and 15-100 eV, respectively. The sample temperature and pressure during measurements are 10 K and $<1.5 \times 10^{-10}$ Torr, respectively. The sample was mounted on the sample holder using epoxy and cleaved *in situ* inside the ultrahigh vacuum.

First-principle calculations: We performed *ab initio* calculation for bulk band structure in the framework of density functional theory (DFT). The exchange-correlation functional was conserved in the Perdew-Burke-Ernzerholf (PBE) method [32]. Employing the Vienna *ab initio* simulation package (VASP) [33], we applied the plane-wave pseudopotential method with a *k*-points grid of $20 \times 20 \times 10$ and a kinetic energy cutoff of 520 eV. For projected surface states and isoenergy surface calculation, we obtained the tight-binding Hamiltonian from the maximally localized Wannier function [34], and the surface Green's function method [35] was employed.

References

[1] Y.L. Chen, J.G. Analytis, J.H. Chu, Z.K. Liu, S.K. Mo, X.L. Qi, H.J. Zhang, D.H. Lu, X. Dai, Z. Fang, S.C. Zhang, I.R. Fisher, Z. Hussain, Z.X. Shen, Experimental Realization of a Three-Dimensional Topological Insulator, Bi_2Te_3, *Science*, **325** (2009) 178.

[2] Z.K. Liu, J. Jiang, B. Zhou, Z.J. Wang, Y. Zhang, H.M. Weng, D. Prabhakaran, S.K. Mo, H. Peng, P. Dudin, T. Kim, M. Hoesch, Z. Fang, X. Dai, Z.X. Shen, D.L. Feng, Z. Hussain, Y.L. Chen, A stable three-dimensional topological Dirac semimetal Cd_3As_2, *Nature Materials*, **13** (2014) 677.

[3] Z.K. Liu, B. Zhou, Y. Zhang, Z.J. Wang, H.M. Weng, D. Prabhakaran, S.K. Mo, Z.X. Shen, Z. Fang, X. Dai, Z. Hussain, Y.L. Chen, Discovery of a Three-dimensional Topological Dirac Semimetal, Na_3Bi, *Science*, **343** (2014) 864.

[4] L.X. Yang, Z.K. Liu, Y. Sun, H. Peng, H.F. Yang, T. Zhang, B. Zhou, Y. Zhang, Y.F. Guo, M. Rahn, D. Prabhakaran, Z. Hussain, S.K. Mo, C. Felser, B. Yan, Y.L. Chen, Weyl semimetal phase in the non-centrosymmetric compound *TaAs*, *Nature Physics*, **11** (2015) 728.

[5] J. Jiang, Z.K. Liu, Y. Sun, H.F. Yang, C.R. Rajamathi, Y.P. Qi, L.X. Yang, C. Chen, H. Peng, C.C. Hwang, S.Z. Sun, S.K. Mo, I. Vobornik, J. Fujii, S.S.P. Parkin, C. Felser, B.H. Yan, Y.L. Chen, Signature of type-II Weyl semimetal phase in $MoTe_2$, *Nature Communications*, **8** (2017) 13973.

[6] Y.L. Chen, Z.K. Liu, J.G. Analytis, J.H. Chu, H.J. Zhang, B.H. Yan, S.K. Mo, R.G. Moore, D.H. Lu, I.R. Fisher, S.C. Zhang, Z. Hussain, Z.X. Shen, Single Dirac Cone Topological Surface State and Unusual Thermoelectric Property of Compounds from a New Topological Insulator Family, *Physical Review Letters*, **105** (2010) 266401.

[7] J.G. Analytis, J.H. Chu, Y.L. Chen, F. Corredor, R.D. McDonald, Z.X. Shen, I.R. Fisher, Bulk Fermi surface coexistence with Dirac surface state in Bi_2Se_3: A comparison of photoemission and Shubnikov-de Haas measurements, *Physical Review B*, **81** (2010) 205407.

[8] A.A. Soluyanov, D. Gresch, Z.J. Wang, Q.S. Wu, M. Troyer, X. Dai, B.A. Bernevig, Type-II Weyl semimetals, *Nature*, **527** (2015) 495.

[9] H.Q. Huang, S.Y. Zhou, W.H. Duan, Type-II Dirac fermions in the $PtSe_2$ class of transition metal dichalcogenides, *Physical Review B*, **94** (2016) 121117.

[10] H.-J. Noh, J. Jeong, E.-J. Cho, K. Kim, B. Min, B.-G. Park, Experimental Realization of Type-II Dirac Fermions in a $PdTe_2$ Superconductor, *Physical Review Letters*, **119** (2017) 016401.

[11] M. Yan, H. Huang, K. Zhang, E. Wang, W. Yao, K. Deng, G. Wan, H. Zhang, M. Arita, H. Yang, Lorentz-violating type-II Dirac fermions in transition metal dichalcogenide $PtTe_2$, *Nature Communications*, **8** (2017) 257.

[12] K. Zhang, M. Yan, H. Zhang, H. Huang, M. Arita, Z. Sun, W. Duan, Y. Wu, S. Zhou, Experimental evidence for type-II Dirac semimetal in $PtSe_2$, *Physical Review B*, **96** (2017) 125102.

[13] K. Ullah, L. Zhu, Z.-D. Meng, S. Ye, S. Sarkar, W.-C. Oh, Synthesis and characterization of novel $PtSe_2$/graphene nanocomposites and its visible light driven catalytic properties, *Journal of Materials Science*, **49** (2014) 4139.

[14] K. Ullah, S. Ye, Z. Lei, K.Y. Cho, W.C. Oh, Synergistic effect of $PtSe_2$ and graphene sheets supported by TiO_2 as cocatalysts synthesized via microwave techniques for improved photocatalytic activity, *Catalysis Science & Technology*, **5** (2015) 184.

[15] H.L.L. Zhuang, R.G. Hennig, Computational Search for Single-Layer Transition-Metal Dichalcogenide Photocatalysts, *Journal of Physical Chemistry C*, **117** (2013) 20440.

[16] X.Y. Chia, A. Adriano, P. Lazar, Z. Sofer, J. Luxa, M. Pumera, Layered Platinum Dichalcogenides (PtS_2, $PtSe_2$, and $PtTe_2$) Electrocatalysis: Monotonic Dependence on the Chalcogen Size, *Advanced Functional Materials*, **26** (2016) 4306.

[17] Y. Zhao, J. Qiao, Z. Yu, P. Yu, K. Xu, S.P. Lau, W. Zhou, Z. Liu, X. Wang, W. Ji, High-Electron-Mobility and Air-Stable 2D Layered $PtSe_2$ FETs, *Advanced Materials*, (2016) 1604230.

[18] W. Yao, E. Wang, H. Huang, K. Deng, M. Yan, K. Zhang, K. Miyamoto, T. Okuda, L. Li, Y. Wang, Direct observation of spin-layer locking by local Rashba effect in monolayer semiconducting $PtSe_2$ film, *Nature Communications*, **8** (2017) 14216.

[19] C. Tsai, K.R. Chan, J.K. Norskov, F. Abild-Pedersen, Theoretical insights into the hydrogen evolution activity of layered transition metal dichalcogenides, *Surface Science*, **640** (2015) 133.

[20] D. Voiry, J. Yang, M. Chhowalla, Recent Strategies for Improving the Catalytic Activity of 2D TMD Nanosheets Toward the Hydrogen Evolution Reaction, *Advanced Materials*, **28** (2016) 6197.

[21] B.J. Yang, N. Nagaosa, Classification of stable three-dimensional Dirac semimetals with nontrivial topology, *Nature Communications*, **5** (2014) 4898.

[22] Q.D. Gibson, L.M. Schoop, L. Muechler, L.S. Xie, M. Hirschberger, N.P. Ong, R. Car, R.J. Cava, Three-dimensional Dirac semimetals: Design principles and predictions of new materials, *Physical Review B*, **91** (2015) 205128.

[23] K. Deng, G.L. Wan, P. Deng, K.N. Zhang, S.J. Ding, E.Y. Wang, M.Z. Yan, H.Q. Huang, H.Y. Zhang, Z.L. Xu, J. Denlinger, A. Fedorov, H.T. Yang, W.H. Duan, H. Yao, Y. Wu, S.S. Fan, H.J. Zhang, X. Chen, S.Y. Zhou, Experimental observation of topological Fermi arcs in type-II Weyl semimetal $MoTe_2$, *Nature Physics*, **12** (2016) 1105.

[24] Y. Wu, N.H. Jo, M. Ochi, L. Huang, D.X. Mou, S.L. Bud'ko, P.C. Canfield, N. Trivedi, R. Arita, A. Kaminski, Temperature-Induced Lifshitz Transition in WTe_2, *Physical Review Letters*, **115** (2015) 166602.

[25] K. Zhang, G.E. Volovik, Lifshitz Transitions via the Type-II Dirac and Type-II Weyl Points, *Jetp Letters*, **105** (2017) 519.

[26] H.J. Zhang, C.X. Liu, X.L. Qi, X. Dai, Z. Fang, S.C. Zhang, Topological insulators in Bi_2Se_3, Bi_2Te_3 and Sb_2Te_3 with a single Dirac cone on the surface, *Nature Physics*, **5** (2009) 438.

[27] Z.K. Liu, L.X. Yang, S.C. Wu, C. Shekhar, J. Jiang, H.F. Yang, Y. Zhang, S.K. Mo, Z. Hussain, B. Yan, C. Felser, Y.L. Chen, Observation of unusual topological surface states in half-Heusler compounds *LnPtBi* (*Ln = Lu, Y*), *Nature Communications*, **7** (2016) 12924.

[28] P. Zhang, P. Richard, T. Qian, Y.M. Xu, X. Dai, H. Ding, A precise method for visualizing dispersive features in image plots, *Review of Scientific Instruments*, **82** (2011) 043712.

[29] L. Fu, C.L. Kane, Topological insulators with inversion symmetry, *Physical Review B*, **76** (2007) 045302.

[30] A. Alexandradinata, X. Dai, B.A. Bernevig, Wilson-loop characterization of inversion-symmetric topological insulators, *Physical Review B*, **89** (2014) 155114.

[31] M.S. Bahramy, O.J. Clark, B.J. Yang, J. Feng, L. Bawden, J.M. Riley, I. Markovic, F. Mazzola, V. Sunko, D. Biswas, S.P. Cooil, M. Jorge, J.W. Wells, M. Leandersson, T. Balasubramanian, J. Fujii, I. Vobornik, J.E. Rault, T.K. Kim, M. Hoesch, K. Okawa, M. Asakawa, T. Sasagawa, T. Eknapakul, W. Meevasana, P.D.C. King, Ubiquitous formation of bulk Dirac cones and topological surface states from a single orbital manifold in transition-metal dichalcogenides, *Nature Materials*, **17** (2018) 21.

[32] J.P. Perdew, K. Burke, M. Ernzerholf, Generalized Gradient Approximation Made Simple, *Physical Review Letter*, **77** (1996) 3865.

[33] G. Kresse, J. Furthmuller, Efficient iteractive schemes for *ab initio* total-energy calculations using a plane-wave basis set, *Physical Review B*, **54** (1996) 11169.

[34] G. Wannier, W. Kohn, G. Weinreich, O. Madelung, Solids, elementary theory for advanced students introduction to solid state theory, *Physical Review*, **52** (1937) 191.

[35] M.P.L. Sancho, J.M.L. Sancho, J. Rubio, Highly convergent schemes for the calculation of bulk and surface Green-functions, *Journal of Physics F: Metal Physics*, **15** (1985) 851.

Chapter 5

ARPES Study on the Mixture Phases of WS_2

Group VI transition metal dichalcogenides (TMDs) usually crystallize in the semiconducting *2H* phases, such as *2H-*MoS_2 and *2H-*WSe_2. They are becoming important 2D semiconducting materials with desirable properties [1-5]. Group VI TMD can also crystallize in a less common distorted *T'* structure, such as T_d*-*$MoTe_2$ and *2M-*WS_2. Moreover, first principle calculation [6] on the monolayer *1T'-*MX_2 systems indicates that this structural distortion causes an intrinsic band inversion which results in a topologically nontrivial quantum spin Hall (QSH) insulator phase. The large-gap QSH insulator state of monolayer *1T'-*WTe_2 is later verified by ARPES, STM and transport studies. For the bulk single crystals, ARPES study have confirmed the topological Weyl semimetal (TWSM) phase in T_d*-*$MoTe_2$. Based on all these experimental results, the topological nontrivial band structures are ubiquitous in the distorted *T'* structured group VI TMDs.

However, the studies are mainly focused on the *T'* structured group VI tellurides. Although the *T'* phase of group VI sulphides and selenides are also reported by unique growing methods [7-9], we lack ARPES study on the band structure. This is probably due to a less thermally stable *T'* phase of group VI sulphides and selenides. It is still challenging to grow high-quality pure phase of *T'* phase of group VI sulphides and selenides. Therefore, ARPES technique with submicron beam spot shows its advantage to spatially resolve the mixture phases of the samples.

Very recently, *2M*-WS_2 has been reported to exhibit a superconducting transition temperature T_c of 8.8 *K* which is highest among all pristine TMDs. Furthermore, similar as other group VI TMDs with distorted *T'* structure, *ab initio* calculation shows it has a TI state characterized by a nonzero Z_2 number and a single massless DP on the surface. The coexistence of superconductivity and nontrivial topological properties makes *2M*-WS_2 a strong candidate for topological superconductor (TSC) [10].

In this chapter, using micro-ARPES and high-resolution ARPES, we spatially distinguish different phases of WS_2 and systematically study the band structure of *2M*-phase, which is predicted to be a promising TSC candidate. The comparison between the ARPES result and *ab initio* calculation is also presented. Although we cannot confirm the existence of the topological surface state (TSS), the ARPES data show some signatures which might favour the theoretical prediction.

5.1 Spatially Resolved *2H/2M* phases

5.1.1 Core level

The environment of tungsten atom in *2H* and *2M* phases of WS_2 are different, as shown in Figs. 5.1(a) and (b). In *2H* phase, it is trigonal prismatically surrounded by *S* atoms, whereas in *2M* phase, it is octahedrally coordinated (see also in section 2.1). The difference in the chemical environment can lead to a shift of the double peaks ($4f_{5/2,7/2}$) of *W* core level. Fig. 5.1(c) shows a typical *W 4f* core level spectroscopy measurement on the WS_2 sample with mixture phases. *2H* phase has higher core level binding energy compared to *2M* phase. By comparing the relative intensity of corresponding core level peaks, we can spatially map the *2M* concentration of the sample, as shown in Fig. 5.1(d). In the same area, we also measure

the density state near the Fermi level as shown in Fig. 5.1(e). One can clearly see that, in general, the *2M* dominated area shows higher intensity near E_F. This observation is consistent with *ab initio* calculation showing metallic *2M* phase (see in section 5.2.1) [10] and semiconducting *2H* phase [11]. The core-level spectra of three typical points representing areas dominated by *2M* phase (*P1*), with mixture *2H* and *2M* phases (*P2*) and dominated by *2H* phase (*P3*) are presented in Fig. 5.1(f). Since even in the *2M*(*2H*) dominated area *P1*(*P3*) one can still observe the intensity from the other phase by the "shoulder" feature, the pure phase domain must have a submicron size as the beam spot is about 0.8×0.8 μm^2.

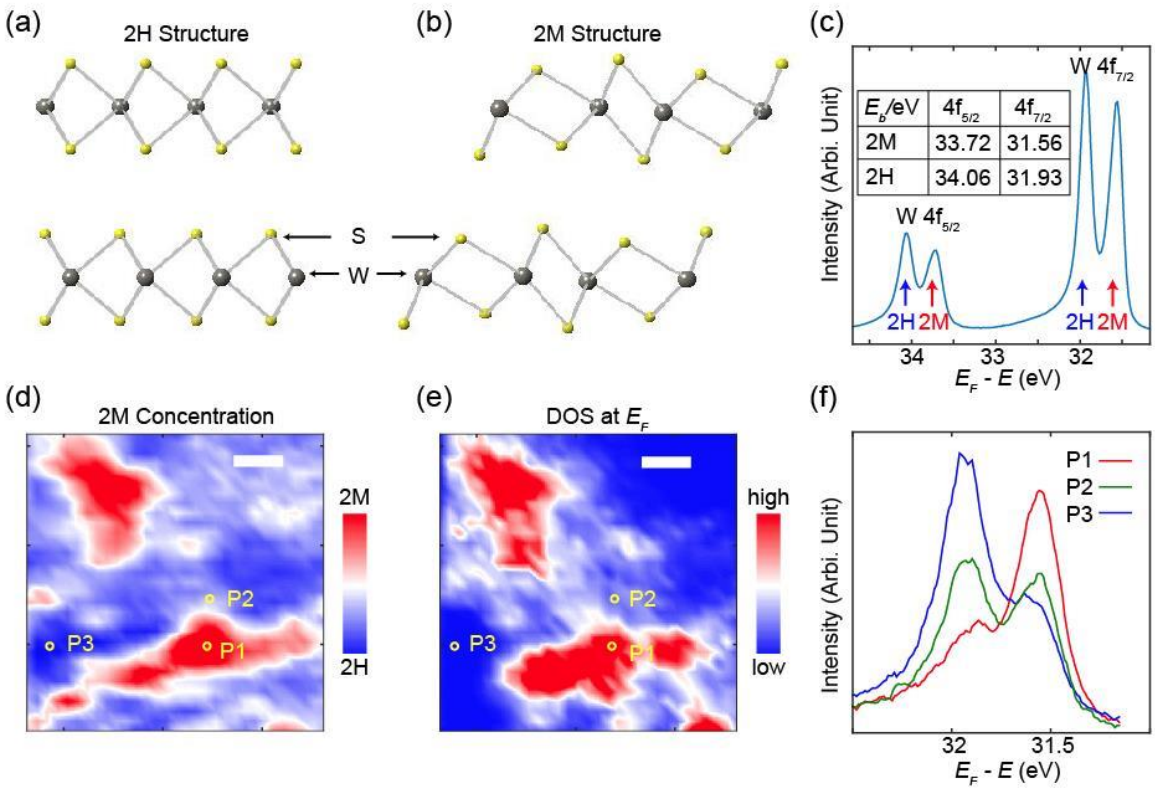


Fig. 5.1 Spatially resolved *2H/2M* phases. (a), (b) Illustration of crystal structure of *2H*- (a) and *2M*- (b) WS_2. (c) Integrated *W 4f* core level spectrum in a typical sample area with a size of 50×50 μm^2 showing two sets of doublets from *2H* and *2M* phases, respectively. (d) Spatial mapping of *2M* concentration in the sample area with a size of 30×30 μm^2. (e) Spatial mapping of density of states (DOS) near E_F in the same area of (d). The scale bars in (d) and (e) are 5 μm. (f) Three selected *W 4f* core level spectra at *P1*, *P2* and *P3*, as indicated in (d) and (e).

5.1.2 Fermi surface and symmetry of *2M/2H* phases

As shown in Fig. 5.2, broad Fermi surface (FS) mapping is carried out at the *2M*-dominated *P1* and *2H*-dominated *P3* point respectively using a photon energy of 74 eV. One can see that the periodicity and symmetry of the Fermi surfaces of *2M* [Fig. 5.2(b)] and *2H*

[Fig. 5.2(d)] match well with the corresponding BZs as indicated in Fig. 5.1(a) and Fig. 5.1(c), respectively.

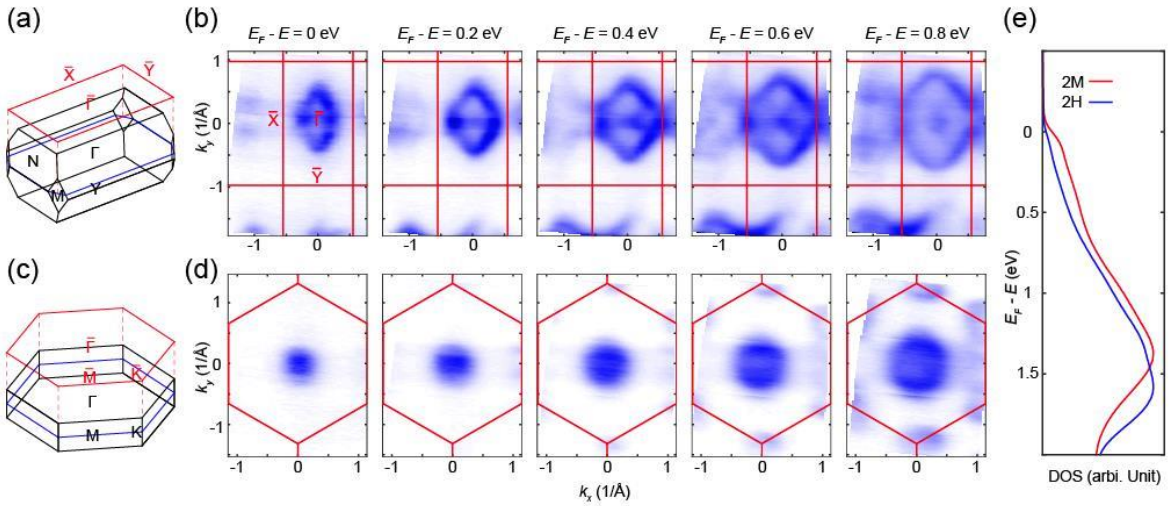


Fig. 5.2 Fermi surface and symmetry of *2H/2M* phases. (a) Schematic of bulk and (100) surface Brillouin zone (BZ) of *2M*-WS_2, indicated by black and red lines, respectively. (b) Energy contours of Fermi surface of the *2M*-dominated point. (c) Schematic of bulk and (001) surface BZ of *2H*-WS_2, indicated by black and red lines, respectively. (d) Energy contours of Fermi surface of the *2H*-dominated point. (e) The integrated DOS of the *2M*- (red curve) and *2H*- (blue curve) dominated points.

The *2M*-dominated FS shows two-fold symmetry. A one-dimensional (1D) chain-like feature is observed along $\bar{\Gamma} - \bar{X}$ direction with a large hole-pocket centred at $\bar{\Gamma}$. In contrast, the *2H*-dominated FS shows clear six-fold symmetry at high binding energy ($E_b > 0.6$ eV) which is consistent with previous studies [11]. The valence top is at $\bar{\Gamma}$ and the double-walled triangular hole-pockets centred at $\bar{K}$ can also be observed at high binding energy. The integrated DOS curves for two measured points are presented in Fig. 5.2(e). The *2M*-dominated point shows higher DOS than *2H*-dominated point which is consistent with the

argument above in section 5.1.1. The finite DOS near E_F of the *2H*-dominated point might due to a small contribution from the minority *2M*-phase.

5.1.3 Domain alignment of *2M* and *2H* phases

The Fermi surface (FS) of *2H/2M* mixture point is measured using photon energy of 95 eV, as shown in Fig. 5.3(a). One can see that, in the low binding energy range ($E_b \leq$ 0.4 eV), it exhibits the *2M* phase characteristic 1D chain feature, however, in the high binding energy range ($E_b \geq 1$ eV), it shows clear six-fold symmetry from the *2H* phase. Since *2H*-WS_2 is semiconducting, the *2M*-phase contribute the major feature near E_F.

Another observation is that, in the reciprocal phase, the $\bar{\Gamma} - \bar{X}$ ($\bar{\Gamma} - \bar{Y}$) direction of *2M*-phase is well aligned with $\bar{\Gamma} - \bar{M}$ ($\bar{\Gamma} - \bar{K}$) direction of *2H*-phase. The alignment in the reciprocal space strongly indicate an atomic alignment in the real space. Two possible domain configuration which matches the FS alignment is presented in Figs. 5.3(b) and (c). As the mixture phase of WS_2 is a result of metastable single crystalline *2M* phase gradually turning into the *2H*-phase, it is natural to expect they have atomic sharp domain boundaries.

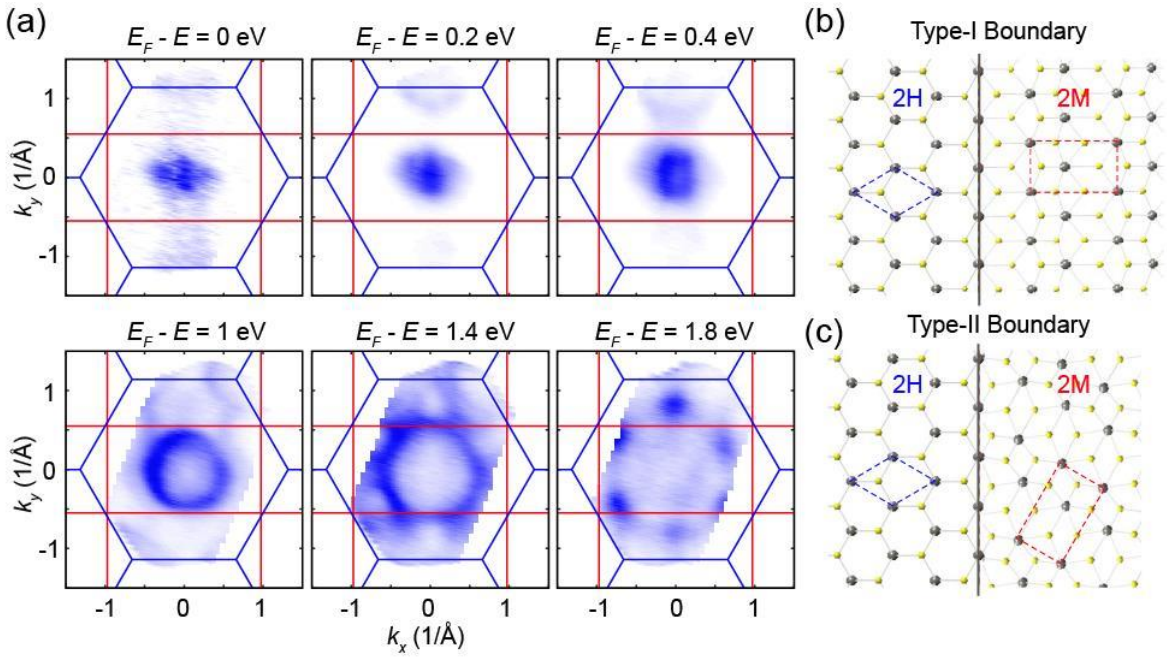


Fig. 5.3 Domain alignment of *2H* and *2M* phases. (a) Energy contours of *2H/2M* mixture phases. In the low binding energy range (upper panel), the FS shows the *2M* characteristic 1D chain feature with two-fold symmetry. In the high binding energy range (lower panel), the FS shows six-fold symmetry from *2H* phase. The photon energy used in the measurement is 95 eV. The surface BZ of *2H* and *2M* phases are indicated by blue and red lines, respectively. (b), (c) Top views of two possible types of domain alignment configuration of *2H* and *2M* phases.

The well-aligned *2H* and *2M* phases share similarities with the studies on the few-layer $MoTe_2$ [12, 13] which exhibits desirable electronic properties with extremely low contact barrier. Our ARPES results also imply the application potential in the similar WS_2 system. High quality atomic coherent semiconductor-superconductor heterojunction can be realized by controllable micro-patterning of *2H/2M* phase (e.g., by laser irradiation) in WS_2, which

may provide an important platform for various exotic phenomena including the mysterious Majorana fermions as well as applications in highly efficient electronics.

5.2 Band Structure of *2M-WS_2*

5.2.1 *Ab initio* calculation

The *ab initio* calculated electronic structure of *2M-WS_2* without and with spin-orbit coupling (SOC) is shown in Figs. 5.4(a) and (b), respectively. It shows a semi-metallic picture without a full band gap at the Fermi level, which is consistent with the experimental observation as presented in section 5.1.1. The band inversion happens near Γ between the ***p*** orbital of *S* atom and ***d*** orbital of *W* atom, which show great similarity with monolayer *1T'-MoS_2* [2, 6]. The band structure is complicated with multiple valence near E_F with nonnegligible k_z dispersion. There are hole-like band near Γ and electron-like band along $\Gamma - N$ direction. On the contrary, band near *Y* is electron-like with hole-like state along $Y - N$ and $Y - M$ direction.

SOC opens the gap between the inverted band near E_F, as shown in Fig. 5(b). Although *2M-WS_2* is semi-metallic, it is possible to define the topology for its electronic structure through the curved Fermi level as indicated by the green dotted line in Fig. 5(b). Since *2M-WS_2* is centrosymmetric, the Z_2 number can be calculated by the parity product at time-reversal-invariant momenta (TRIM) which proves to be a strong TI state with Z_2 (1;000) originated from the band inversion near Γ.

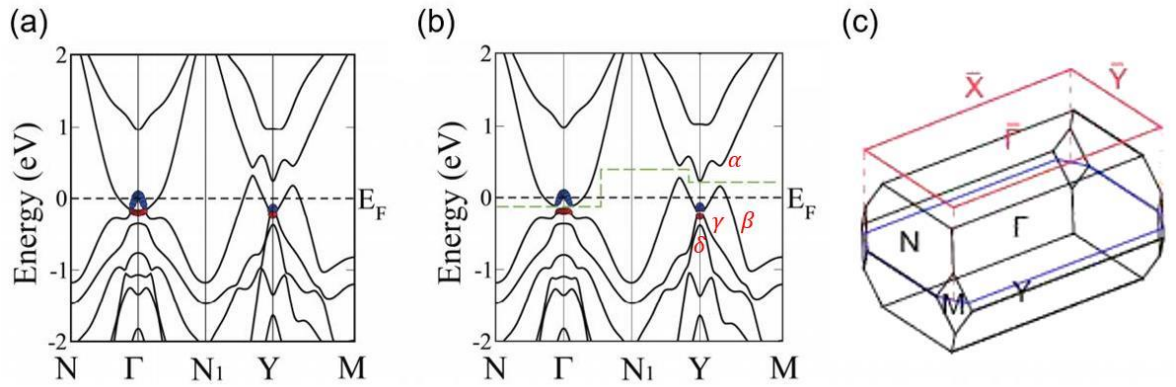


Fig. 5.4 *Ab initio* calculated electronic structure of *2M-WS*$_2$. (a) and (b), Band structure without and with the SOC. The blue closed circles present the projection of ***p*** orbital of *S* atom, and the red closed circles present the projection of ***d*** orbital of *W* atom, indicating the band inversion near Γ. The green dashed line in (b) is the defined curved Fermi level to calculate the Z_2 number. (c) Schematic of the bulk and (100) surface BZ of *2M-WS*$_2$. Fig. 5.4(a) and (b) are adapted from Ref. [10].

5.2.2 Fermi surface

Fermi surface (FS) near $\bar{\Gamma}$ is measured using 74 eV and 95 eV in the energy window of 0.2 eV below Fermi level, as shown in Fig. 5.5. One can clearly see that the Fermi surface is highly photon energy dependent. At $h\nu = 74$ eV, the hole-pocket along $\bar{\Gamma} - \bar{Y}$ is with strong spectral weight. In contrast, the measurement using $h\nu = 95$ eV has strong spectral intensity for the small eye-like hole- pockets along $\bar{\Gamma} - \bar{X}$ and the 1D chain-like feature on either side of $\bar{\Gamma} - \bar{X}$. However, due to limited energy and momentum resolution of micro-ARPES, the eye-like feature is not well resolved. The comparison between the combined experimental results with the calculation shows general agreement.

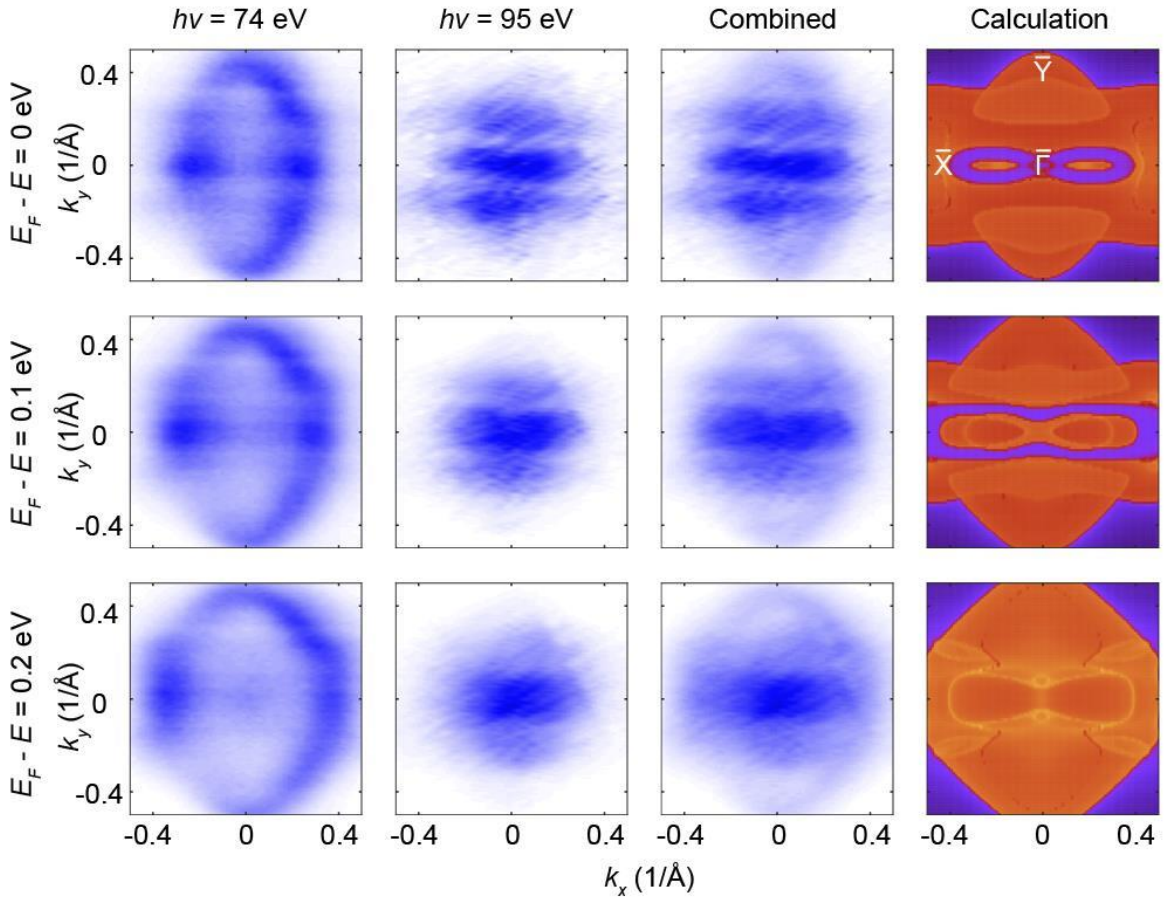


Fig. 5.5 Fermi surface of *2M-WS_2* near $\bar{\Gamma}$. ARPES measurement using photon energies of 74 eV and 95 eV are presented in column 1 and column 2. The combined experimental data and *ab initio* calculation are presented in column 3 and column 4. The *ab initio* calculations are adapted from Ref. [10].

5.2.3 Band dispersion

ARPES measured band dispersion along $\bar{\Gamma} - \bar{X}$ and $\bar{\Gamma} - \bar{Y}$ as well as the corresponding *ab initio* calculations are presented Fig. 5.6. In the energy range of 1 eV below the Fermi level, there are 4 VBs in the $k_z = 0$ plane and 3 VBs in the $k_z = \pi$ plane, as indicated in the column 7 and column 8 of Fig. 5.6. We label them as α, β, γ and δ bands. Since the electronic structure has strong k_z-dependence, the measurement at $h\nu = 74$ eV and $h\nu =$

95 eV might cut through two arbitrary k_z. From the comparison between the ARPES measured dispersion with the calculation, we are able to identify each band (α, β, γ and δ) as marked in the column 5 and column 6 of Fig. 5.6. The data measured using $h\nu = 74$ eV might be closer to $k_z = \pi$ plane, whereas the data measured using $h\nu = 95$ eV share some similarities with the calculation for $k_z = 0$ plane.

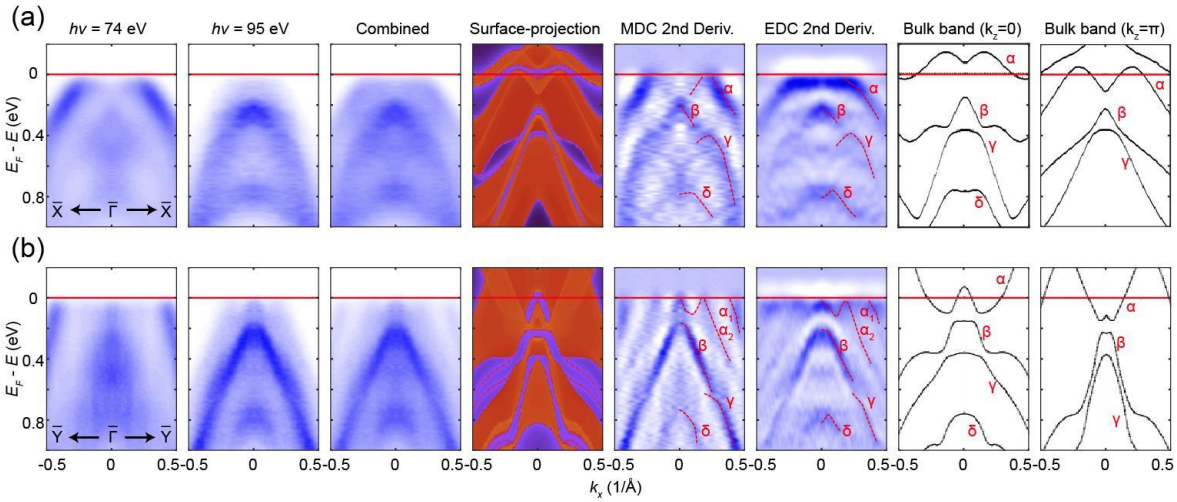


Fig. 5.6 Band dispersion of *2M-WS*$_2$. The upper and lower panel show the band dispersion along $\bar{X} - \bar{\Gamma} - \bar{X}$ and $\bar{Y} - \bar{\Gamma} - \bar{Y}$, respectively. Column 1-8 compare the measurement using photon energies of 74 eV (column 1), 95 eV (column 2), combined ARPES data (column 3), calculated (100) surface projected band structure (column 4), second derivative plot along momentum-distribution-curve (MDC) direction of the combined ARPES data (column 5), second derivative plot along energy-distribution-curve (EDC) direction of the combined ARPES data (column 6), calculated bulk band for $k_z = 0$ plane (column 7) and $k_z = \pi$ plane (column 8), respectively. The *ab initio* calculations are adapted from Ref. [10].

However, unfortunately, it is difficult to identify the surface states between α and β bulk band continuum, and between β and γ bulk bad continuum from the experimental data. To

confirm the existence of these surface state, we should (1) improve the sample quality of the pure phase of *2M-WS_2* single crystals; (2) improve the energy and momentum resolution using lower photon energy.

5.3 Signatures of Topological Band Structure

5.3.1 Potassium dosing

By potassium dosing on the surface of *2M-WS_2*, we can increase the carrier density at the Fermi level hence reach the CB. The band dispersion along $\bar{Y} - \bar{\Gamma} - \bar{Y}$ direction of the pristine and potassium dosed sample is compared in Figs. 5.7(a) and (b). From Fig. 5.7(b), one can observe the electron-like band near the Fermi level, which is in general agreement with the *ab initio* surface-projected calculation [see Fig. 5.7(c)]. Therefore, the observed band structure is consistent with the general band inversion picture as illustrated in Fig. 5.7(d) although the TSS in the inverted local band gap between the CB and the VB is yet to resolved due to the sample quality and limited resolution.

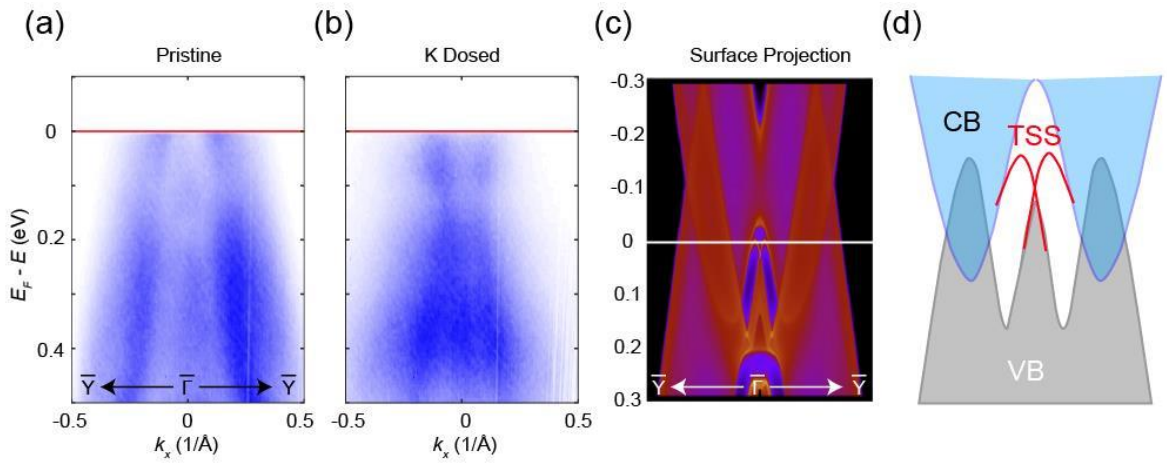


Fig. 5.7 Potassium dosing of *2M-WS*$_2$. (a), (b) ARPES measured band dispersion along $\bar{Y} - \bar{\Gamma} - \bar{Y}$ of the pristine sample (a) and the potassium dosed sample (b) (dosing time 330 *s*, current 6.5 *A*). (c) *Ab initio* calculated (100) surface-projected band structure. (d) Schematics of the topological surface state (TSS) in the inverted bulk band gap between the conduction band (CB) and the valence band (VB). The *ab initio* calculation is adapted from Ref. [10].

5.3.2 Zoomed-in FS mapping near $\bar{\Gamma}$

To resolve the more details of the band structure near $\bar{\Gamma}$, we carry out fine mapping using a photon energy of 27 eV, as presented in Figs. 5.8(a)-(e). By comparison with the calculation as shown in Figs. 5.8(f)-(j), we are able to resolve the two eye-like hole-pockets along $\bar{X} - \bar{\Gamma} - \bar{X}$ direction. However, the expected massless surface Dirac cone is still unable to resolved as it is energetically too close to the bulk continuum which is beyond the energy resolution (≈ 30 meV) of the micro-ARPES.

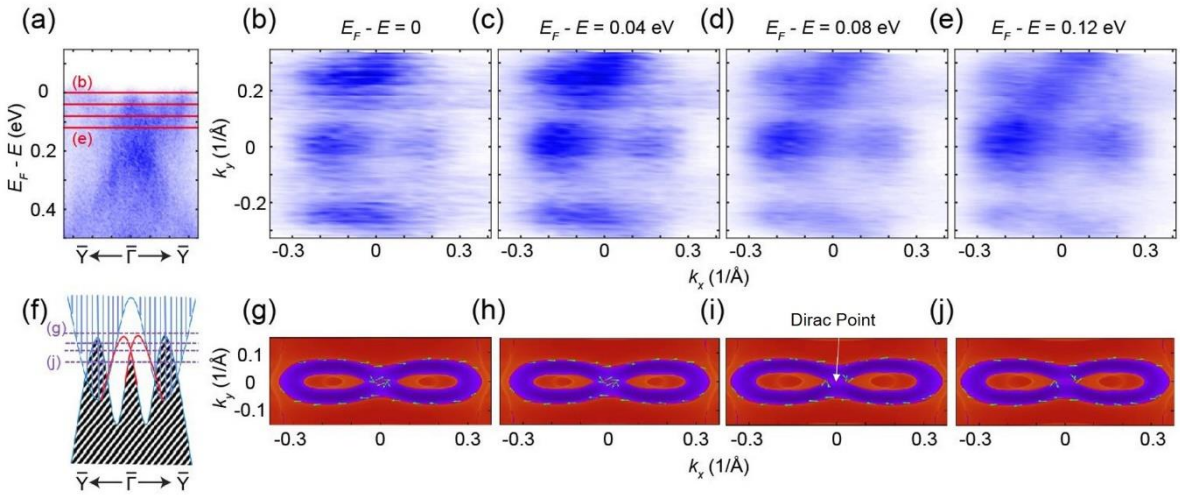


Fig. 5.8 Zoomed-in FS mapping near $\bar{\Gamma}$. (a) ARPES measured band dispersion along $\bar{Y} - \bar{\Gamma} - \bar{Y}$ direction. (b)-(e) Energy contours of FS near $\bar{\Gamma}$ at binding energies indicated by the red lines in (a). The photon energy used in the measurement is 27 eV. (f) Schematic of band structure. (g)-(j) *Ab initio* calculated (100) surface-projected energy contours at binding energies indicated by the purple dashed lines in (f). The *ab initio* calculations are adapted from Ref. [10].

5.3.3 Signature of the topological surface state at $\bar{\Gamma}$

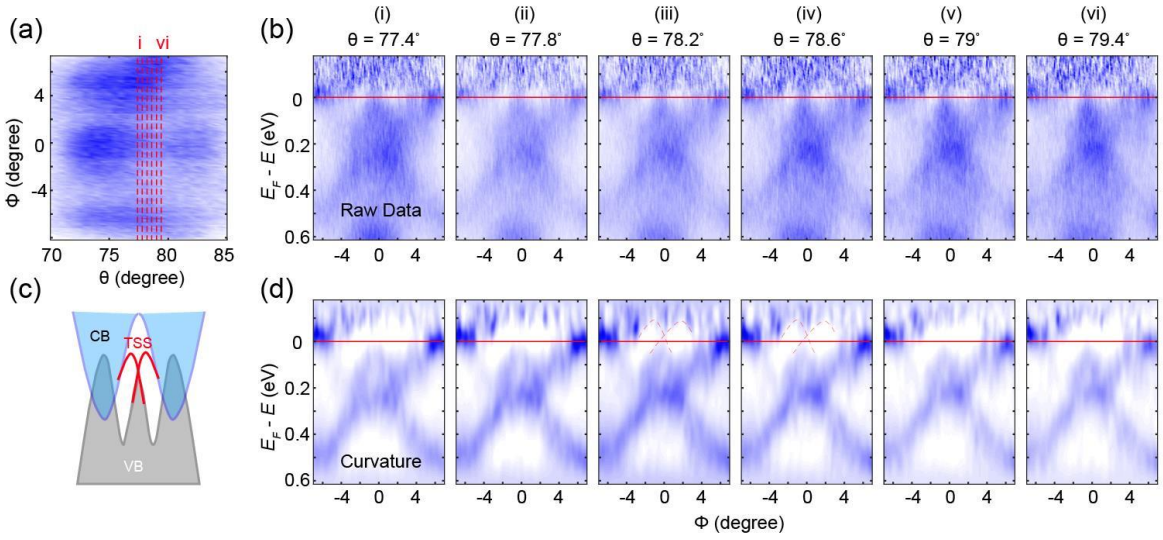


Fig. 5.9 Signature of the topological surface state $\bar{\Gamma}$. (a) Raw data of FS mapping near $\bar{\Gamma}$ in the angle space. (b) A series of fine cuts (raw data) near $\bar{\Gamma}$ at different polar angle Φ, as indicated by the dashed red lines in (a). (c) Schematic of the nontrivial topological band structure. The raw data is normalized along MDC direction to enhance the spectral intensity near the Fermi level. (d) Curvature plot of (b).

A series of fine cuts near $\bar{\Gamma}$ is collected using the photon energy of 27 eV, as shown in Fig. 5.9(b). To enhance the spectral weight near the Fermi level, the ARPES data is normalized along MDC direction. Using the same parameters for different cuts, we apply the curvature method (see section 1.2.3) to enhance the feature of the spectrum, as shown in Fig. 5.9(d). One can see that the CB and VB is connected by a "X" feature in the cuts measured at Φ = 78.2° and Φ = 78.6°. In other cuts, the CB and VB are separated by a gap with a size of about 70 meV. The observed "X" feature might be a signature for the expected topological surface state at $\bar{\Gamma}$.

5.4 Discussion and Conclusion

This chapter provides a preliminary ARPES study on the novel *2M*-phase of WS_2. Using micro-ARPES, we can spatially distinguish the trivial semiconducting *2H* phase and the nontrivial semi-metallic *2M* -phase by the shifting of *W 4f* core level peaks. The FS mapping of the mixture phase area confirms the coherent alignment of *2H* and *2M* domains. This indicates that WS_2 has the potential to become a material to fabricate high-quality semiconductor-superconductor heterojunction. The ARPES measured band structure is in general consistent with the *ab initio* calculation. However, the evidence that support the existence of the topological surface state is still weak.

From a perspective of possible application for the next generation highly efficient electronics, the domain structure of *2M/2H* requires investigation by other experiment technique, such as STM and TEM. On the other hand, to confirm the long-searching TSC phase, the sample quality of pure *2M*-WS_2 need to be improved. High-resolution ARPES investigation on the high-quality *2M*-WS_2 single crystal might provide a stronger evidence for the Dirac TSS. We can also expect a superconducting gap opening in the nontrivial topological surface state below $T_c \approx 8.8$ K.

Note Added: During finalizing this thesis, another STM study on $2M - WS_2$ reported probable Majorana bound states in magnetic vortices [14], which further indicate the its non-trivial topology.

Method

Sample Preparation: $2M - WS_2$ single crystals were prepared by deintercalation of interlayer potassium cations from $K_{0.7}WS_2$ crystals. For the synthesis of $K_{0.7}WS_2$, K_2S_2 (prepared via liquid ammonia), W (99.9%, Alfa Aesar) and S (99.9%, Alfa Aesar) were mixed by the stoichiometric ratios and ground in an argon-filled glovebox. The mixtures were pressed into a pellet and sealed in the evacuated quartz tube. The tube was heated at 850 °C for 2000 min and slowly cooled to 550 °C at a rate of 0.1 °C/min.

The synthesized $K_{0.7}WS_2$ was oxidized chemically by an excess of 0.01 mol/L $K_2Cr_2O_7$ in aqueous H_2SO_4 at room temperature for 1 hour. Finally, the $2M - WS_2$ crystals were obtained after washing in distilled water for several times and drying in the vacuum oven at room temperature [10].

ARPES: Measurements were performed at beamline I05 nano branch (Diamond Light Source, UK) equipped with an DA30 electron analyzer using $h\nu = 95$ eV and Spectromicroscopy (Elettra Synchrotron, Italy) using $h\nu = 74$ eV and 27 eV. The sample was mounted on the sample holder with Torr Seal covered with conducting graphite. The mounting excludes any heating procedure. The sample is cleaved *in situ* under ultrahigh vacuum. The sample temperature and pressure during measurements are 40 K and $<1.5 \times 10^{-10}$ Torr, respectively.

First-principles calculations: The first-principles calculations were carried out in the framework of the generalized gradient approximation (GGA) functional of the density functional theory through employing the Vienna *ab initio* simulation package (VASP) with projector augmented wave pseudopotentials [15]. The experimental lattice constants are taken, and inner positions are obtained through full relaxation with a total energy tolerance

10^{-5} eV. The SOC effect is self-consistently included. Modified Becke-Johnson (mBJ) functional is employed for the double check and the electronic structure and topological nature remain unchanged [10].

References

[1] H.F. Yang, A.J. Liang, C. Chen, C.F. Zhang, N.B.M. Schroeter, Y.L. Chen, Visualizing electronic structures of quantum materials by angle-resolved photoemission spectroscopy, *Nature Reviews Materials*, **3** (2018) 341.

[2] S. Manzeli, D. Ovchinnikov, D. Pasquier, O.V. Yazyev, A. Kis, 2D transition metal dichalcogenides, *Nature Reviews Materials*, **2** (2017) 17033.

[3] M. Chhowalla, H.S. Shin, G. Eda, L.J. Li, K.P. Loh, H. Zhang, The chemistry of two-dimensional layered transition metal dichalcogenide nanosheets, *Nature Chemistry*, **5** (2013) 263.

[4] Y. Zhang, T.R. Chang, B. Zhou, Y.T. Cui, H. Yan, Z.K. Liu, F. Schmitt, J. Lee, R. Moore, Y.L. Chen, H. Lin, H.T. Jeng, S.K. Mo, Z. Hussain, A. Bansil, Z.X. Shen, Direct observation of the transition from indirect to direct bandgap in atomically thin epitaxial $MoSe_2$, *Nature Nanotechnology*, **9** (2014) 111.

[5] Y. Zhang, M.M. Ugeda, C.H. Jin, S.F. Shi, A.J. Bradley, A. Martin-Recio, H. Ryu, J. Kim, S.J. Tang, Y. Kim, B. Zhou, C. Hwang, Y.L. Chen, F. Wang, M.F. Crommie, Z. Hussain, Z.X. Shen, S.K. Mo, Electronic Structure, Surface Doping, and Optical Response in Epitaxial WSe_2 Thin Films, *Nano Letters*, **16** (2016) 2485.

[6] X.F. Qian, J.W. Liu, L. Fu, J. Li, Quantum spin Hall effect in two-dimensional transition metal dichalcogenides, *Science*, **346** (2014) 1344.

[7] R. Kappera, D. Voiry, S.E. Yalcin, B. Branch, G. Gupta, A.D. Mohite, M. Chhowalla, Phase-engineered low-resistance contacts for ultrathin MoS_2 transistors, *Nature Materials*, **13** (2014) 1128.

[8] M. Acerce, D. Voiry, M. Chhowalla, Metallic 1T phase MoS_2 nanosheets as supercapacitor electrode materials, *Nature Nanotechnology*, **10** (2015) 313.

[9] Y.C. Lin, D.O. Dumcencon, Y.S. Huang, K. Suenaga, Atomic mechanism of the semiconducting-to-metallic phase transition in single-layered MoS_2, *Nature Nanotechnology*, **9** (2014) 391.

[10] Y. Fang, J. Pan, D. Zhang, D. Wang, H.T. Hirose, T. Terashima, S. Uji, Y. Yuan, W. Li, Z. Tian, J. Xue, Y. Ma, W. Zhao, Q. Xue, G. Mu, H. Zhang, F. Huang, Discovery of superconductivity in *2M* WS_2 with possible topological surface states, *Advanced Materials*, (2019) 1901942.

[11] D.W. Latzke, W.T. Zhang, A. Suslu, T.R. Chang, H. Lin, H.T. Jeng, S. Tongay, J.Q. Wu, A. Bansil, A. Lanzara, Electronic structure, spin-orbit coupling, and interlayer interaction in bulk MoS_2 and WS_2, *Physical Review B*, **91** (2015) 235202.

[12] J.H. Sung, H. Heo, S. Si, Y.H. Kim, H.R. Noh, K. Song, J. Kim, C.S. Lee, S.Y. Seo, D.H. Kim, H.K. Kim, H.W. Yeom, T.H. Kim, S.Y. Choi, J.S. Kim, M.H. Jo, Coplanar semiconductor-metal circuitry defined on few-layer $MoTe_2$ via polymorphic heteroepitaxy, *Nature Nanotechnology*, **12** (2017) 1064.

[13] S. Cho, S. Kim, J.H. Kim, J. Zhao, J. Seok, D.H. Keum, J. Baik, D.H. Choe, K.J. Chang, K. Suenaga, S.W. Kim, Y.H. Lee, H. Yang, Phase patterning for ohmic homojunction contact in $MoTe_2$, *Science*, **349** (2015) 625.

[14] Y. Yuan, J. Pan, X. Wang, Y. Fang, C. Song, L. Wang, K. He, X. Ma, H. Zhang, F. Huang, W. Li, Q.K. Xue, Evidence of anisotropic Majorana bound states in 2M-WS_2, *Nature Physics*, **1** (2019).

[15] G. Kresse, D. Joubert, From ultrasoft pseudopotentials to the projector augmented-wave method, *Physical Review B*, **59** (1999) 1758

Chapter 6

Summary and Future Works

6.1 Summary

This thesis describes the ARPES study on the electronic structures of three selected TMDs. Each of the materials reported here represents one group of TMDs with exotic properties. Our results have expanded current understanding on the electronic structures of different phases of TMDs.

In chapter 1, we deliver a general introduction on the principle of ARPES, data analysis technique that we use throughout the thesis and the ARPES facility where we collect the data in this thesis. This chapter provides the necessary background knowledge for the readers who are not in the field of PES and equips them with basic understanding of ARPES data presented in this thesis.

In chapter 2, an overview of TMD is presented. Crystal structure, electronic structure and exotic properties of the large family of TMDs are classified and summarized. This chapter provides the current understanding of the topic that we choose to investigate in this thesis.

Chapter 3 to chapter 5 describe the experimental results on three selected metallic TMDs: *2H-*$TaSe_2$ (chapter 3), *1T-*$PtSe_2$ (chapter 4) and *2M-*WS_2 (chapter 5).

In chapter 3, the ARPES investigation focuses on the band structure reconstruction in the low-temperature 3×3 CDW phase in comparison with the high-temperature normal phase. Quantitatively, we have resolved the CDW band gap size distribution in the momentum-

energy space, which has been controversial for decades. The interpretation of the result leads to an electron-phonon mediated Peierls picture in the quasi-2D TMD system in contrast with the weak-coupling Peierls picture in the 1D system.

In chapter 4, *1T-$PtSe_2$*, a type-II Dirac semimetal candidate, has been systematically studied by ARPES. The measured electronic structure in the full 3D BZ confirms the existence of the strongly tilted conic dispersion along k_z direction. In addition to the type-II bulk Dirac point, we have discovered topological surface states around TRIM $\bar{\Gamma}$ and $\bar{M}$, which indicate an intricate parity inversion topology of the band structure.

In chapter 5, using micro-ARPES, we have managed to spatially distinguish the novel *2M* phase of WS_2, which has been a promising TSC candidate, from the trivial semiconducting *2H* phase. The experimental observation is in general agreement with the first-principle calculation and some signatures are found that might originate from the expected TSS. However, more future investigations on high-quality pure *2M* phase sample are necessary for the confirmation of the topological superconducting phase.

As a natural extension of my DPhil studies, two proposals are presented in section 6.2 for my future work in the postdoctoral research.

6.2 Future works

6.2.1 Artificial 2D twistronics and gating-devices

2D materials have attracted intensity research interests due to the exquisite physical properties emerged in such simple, pure and controllable systems. Typical 2D materials, such as graphene and TMDs have strong covalent in-plane bonds which keep the stability,

while the relatively weak interlayer van der Waals force makes them easy to be mechanically exfoliated and then artificially stacked together, just like building with Lego blocks. Recently, multiple studies indicate that the electronic structure can be tuned by the stacking geometry. Exotic states can emerge under certain types of material and twist angle.

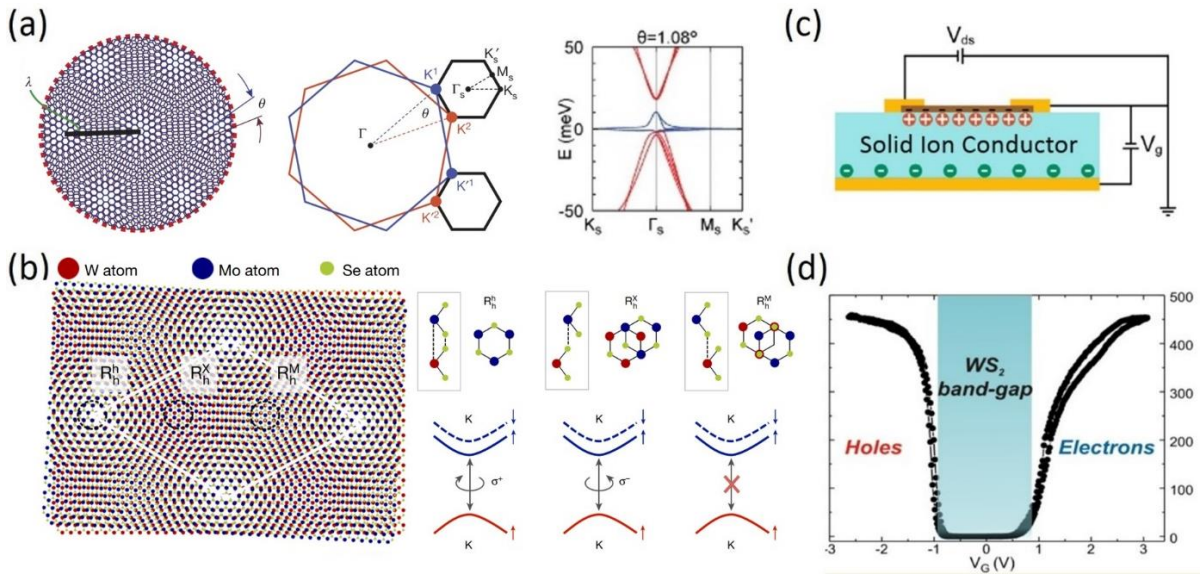


Fig. 6.1 Artificial twistronics and gating-devices. (a) Moiré-pattern and strongly correlated electronic structure of magic-angle bilayer graphene. Adapted from Ref. [1]. (b) Moiré-superlattice of $MoSe_2/WSe_2$ and its electronic properties. Adapted from Ref. [2]. (c) The geometry of typical gating-devices using a solid ion conductor. Adapted from Ref. [3]. (d) Transport characteristics of a typical gating-device. Adapted from Ref. [4].

Most notably, strong correlation behaviour has been observed in the magic-angle bilayer graphene superlattice. It results in an unexpected Mott state and with adequate electrostatic doping, the system can be driven into the superconducting state [1, 5]. Motivated by this work, signatures of moiré-trapped valley excitons in $MoSe_2/WSe_2$ heterobilayers have been reported [2, 6, 7]. Since 2D material is a huge family and the physics behind these reported

exotic phenomena is unclear yet, the twistronic is a promising unexplored area for nano/micro-ARPES study.

Moreover, another advantage of nano/micro-ARPES is that it has the potential to be equipped with a back-gating technique which has been commonly used in transport measurement. As mentioned above, tuning the carrier concentration by electrostatic doping may trigger a quantum phase transition. More generally, it is meaningful for the ARPES technique to directly visualize the unoccupied states in solids without introducing alkali metals or exciting the system by ultrafast laser pulse.

In conclusion, nano/micro-ARPES study on artificial 2D twistronics and gated-devices is a challenging but promising field. It would require close collaboration from research groups which have expertise in nano-fabrication, transport measurement and ARPES technique.

6.2.2 Phase-separated materials

One of the most direct advantages of nano/micro-ARPES is its sub-micron spatial resolution ability which makes it a powerful tool to study phase-separated materials, such as multi-$\boldsymbol{q}$ CDW materials and magnetic materials. Although CDW and magnetic systems have been thoroughly investigated for many years [8, 9], the electronic structure detected by regular ARPES can be regarded as an average result over a large number of domains. With the help of nano/micro-ARPES, one can spatially resolve each domain and study the correlation between the electronic structure and order parameters.

Very recent studies have pointed out the close connections of chirality and topology between lattice and electronic structures [10, 11]. Also, it has been reported that, along with simple stripe-like or irregularly shaped domains, intriguing vortex-type topological domain

configurations can exist in a variety of 2D systems, including TMDs [12], as shown in Fig. 6.2(a)-(c). Furthermore, exotic physical properties can emerge at the boundaries between different domains. As a remarkable example, the discovery of highly conductive magnetic domain walls in a magnetic insulator $Nd_2Ir_2O_7$ has attracted high research interest [13], as shown in Fig. 6.2(d).

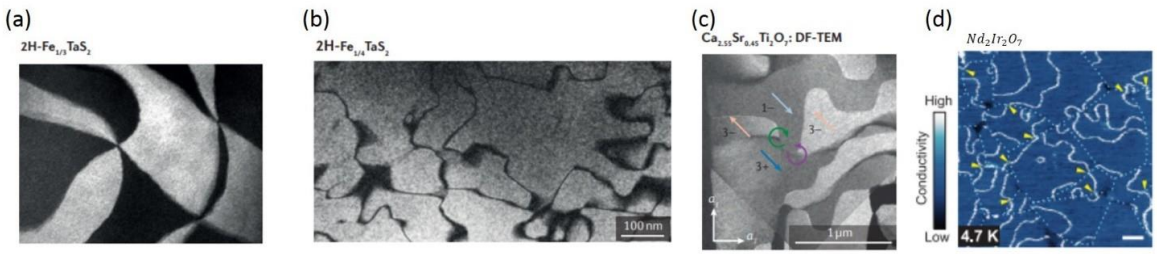


Fig. 6.2 Chiral domain configuration in *2H-*$Fe_{1/3}TaS_2$ (a), ***2H-*$Fe_{1/4}TaS_2$** (b) **and** $Ca_{2.55}Sr_{0.45}Ti_2O_7$ (c), adapted from Ref. [12]. (d) Highly-conductive magnetic domain walls in a magnetic insulator $Nd_2Ir_2O_7$, adapted from Ref. [13].

References

[1] Y. Cao, V. Fatemi, A. Demir, S. Fang, S.L. Tomarken, J.Y. Luo, J.D. Sanchez-Yamagishi, K. Watanabe, T. Taniguchi, E. Kaxiras, R.C. Ashoori, P. Jarillo-Herrero, Correlated insulator behaviour at half-filling in magic-angle graphene superlattices, *Nature*, **556** (2018) 80.

[2] K. Tran, G. Moody, F.C. Wu, X.B. Lu, J. Choi, K. Kim, A. Rai, D.A. Sanchez, J.M. Quan, A. Singh, J. Embley, A. Zepeda, M. Campbell, T. Autry, T. Taniguchi, K. Watanabe, N.S. Lu, S.K. Banerjee, K.L. Silverman, S. Kim, E. Tutuc, L. Yang, A.H. MacDonald, X.Q. Li, Evidence for moire excitons in van der Waals heterostructures, *Nature*, **567** (2019) 71.

[3] C.L. Wu, H.T. Yuan, Y.B. Li, Y.J. Gong, H.Y. Hwang, Y. Cui, Gate-Induced Metal-Insulator Transition in MoS_2 by Solid Superionic Conductor LaF_3, *Nano Letters*, **18** (2018) 2387.

[4] D. Braga, I.G. Lezama, H. Berger, A.F. Morpurgo, Quantitative Determination of the Band Gap of WS_2 with Ambipolar Ionic Liquid-Gated Transistors, *Nano Letters*, **12** (2012) 5218.

[5] Y. Cao, V. Fatemi, S. Fang, K. Watanabe, T. Taniguchi, E. Kaxiras, P. Jarillo-Herrero, Unconventional superconductivity in magic-angle graphene superlattices, *Nature*, **556** (2018) 43.

[6] K.L. Seyler, P. Rivera, H.Y. Yu, N.P. Wilson, E.L. Ray, D.G. Mandrus, J.Q. Yan, W. Yao, X.D. Xu, Signatures of moire-trapped valley excitons in $MoSe_2/WSe_2$ heterobilayers, *Nature*, **567** (2019) 66.

[7] C.H. Jin, E.C. Regan, A.M. Yan, M.I.B. Utama, D.Q. Wang, S.H. Zhao, Y. Qin, S.J. Yang, Z.R. Zheng, S.Y. Shi, K. Watanabe, T. Taniguchi, S. Tongay, A. Zettl, F. Wang, Observation of moire excitons in WSe_2/WS_2 heterostructure superlattices, *Nature*, **567** (2019) 76.

[8] K. Rossnagel, On the origin of charge-density waves in select layered transition-metal dichalcogenides, *Journal of Physics: Condensed Matter*, **23** (2011) 213001.

[9] P. Mavropoulos, I. Galanakis, A review of the electronic and magnetic properties of tetrahedrally bonded half-metallic ferromagnets, *Journal of Physics-Condensed Matter*, **19** (2007) 315221.

[10] G.Q. Chang, B.J. Wieder, F. Schindler, D.S. Sanchez, I. Belopolski, S.M. Huang, B. Singh, D. Wu, T.R. Chang, T. Neupert, S.Y. Xu, H. Lin, M.Z. Hasan, Topological quantum properties of chiral crystals, *Nature Materials*, **17** (2018) 978.

[11] N.B. Schröter, D. Pei, M.G. Vergniory, Y. Sun, K. Manna, F. de Juan, J.A. Krieger, V. Süss, M. Schmidt, P. Dudin, Chiral topological semimetal with multifold band crossings and long Fermi arcs, *Nature Physics* **1** (2019).

[12] F.T. Huang, S.W. Cheong, Aperiodic topological order in the domain configurations of functional materials, *Nature Reviews Materials*, **2** (2017) 17004.

[13] E.Y. Ma, Y.T. Cui, K. Ueda, S.J. Tang, K. Chen, N. Tamura, P.M. Wu, J. Fujioka, Y. Tokura, Z.X. Shen, Mobile metallic domain walls in an all-in-all-out magnetic insulator, *Science*, **350** (2015) 538.

Appendix A

Nonsymmorphic Symmetry Protected Dirac Nodal Lines in Space Group *P*6$_3$/*mmc*

A.1 Spinless case

Within space group *P*6$_3$/*mmc* (No. 194), the nonsymmorphic symmetry operation that protect the Dirac nodal line is the two-fold screw symmetry along *z*. Let us prove that in a crystal preserving the time-reversal-symmetry *T*, inversion symmetry *I*, and the two-fold screw axis along *z*, S_z: $(x, y, z, t) \rightarrow (-x, -y, z + \frac{1}{2}, t)$, the energy bands at the $k_z = \pi/c$ plane will be twofold degenerated if the spin effect is excluded. By using these three symmetries, one can compose two compound symmetries, $C = IT$ and $S = IS_z$. In the real space, *C* and *S* act as

$$\begin{aligned} C&: (x, y, z, t) \rightarrow (-x, -y, -z, -t), \\ S&: (x, y, z, t) \rightarrow \left(x, y, -z, -\frac{1}{2}, t\right). \end{aligned} \tag{A1}$$

In momentum space, one easily finds that all the $\boldsymbol{k}$ points are invariant points under the action of *C*. On the other hand, *S* translates (k_x, k_y, k_z) to (k_x, k_y, k_z), which means $k_z = 0$ and $k_z = \pi/c$ are the two invariant planes of *S*. Applying *S* twice, the coordinates in the real space return back and one finds $S^2 = 1$, which means the eigenvalues of *S* are ± 1 and one

can use them to label the Bloch states $|\psi(\boldsymbol{k})\rangle$ of the system's Hamiltonian by $S|\psi^{\pm}(\boldsymbol{k})\rangle = \pm|\psi^{\pm}(\boldsymbol{k})\rangle$.

We find that, under the action of *C*, each eigenstate $|\psi^{\pm}(\boldsymbol{k})\rangle$ is switched to degenerate state of an opposite *S* label. Before showing this, we first prove that *C* and *S* take an anticommutation relation at $k_z = \pi/c$. By using Eq. (A1), one obtains

$$\begin{aligned} SC&: (x, y, z, t) \to \left(-x, -y, z - \frac{1}{2}, -t\right), \\ CS&: (x, y, z, t) \to \left(-x, -y, z + \frac{1}{2}, -t\right), \end{aligned} \tag{A2}$$

from which one finds in $\boldsymbol{k}$-space

$$CS = \boldsymbol{T_c} SC = e^{ik_z c}, \tag{A3}$$

with $\boldsymbol{T_c}$ being the translation along *z*-axis by one primary vector $\boldsymbol{c}$. Therefore, the anti-commutator of *C* and *S* becomes zeros, $\{C, S\} = 0$, at $k_z = \pi/c$. With this anticommutation relation, one can prove that *C* relates the eigenstates to their degenerate partner of opposite *S* label as follows:

$$SC|\psi^{\pm}(\boldsymbol{k})\rangle = e^{-i\frac{\pi}{c}c} CS|\psi^{\pm}(\boldsymbol{k})\rangle = \mp|\psi^{\pm}(\boldsymbol{k})\rangle. \tag{A4}$$

Then, on the $k_z = \pi/c$ plane, one proves that each band is twofold degenerate. We should stress here that, for the case of no spin, actually the inversion *T* is not necessary for the degeneracy at $k_z = \pi/c$. We can use an alternative compound symmetry $\Theta = TS_z$ to protect the degeneracy. It is easy to check that it takes $\Theta^2 = -1$ at the $k_z = \pi/c$ plane, which ensures a Kramer degeneracy with the two related states labelled by eigenvalues $\pm i$ of Θ. However, in the following spinful case, Θ is not enough to protect the nodal lines. For the purpose of consistency with the spinful case below, we use the same compound symmetries IS_z and IT in the spinless case.

A.2 The effect of spin-orbit coupling

Including the spin degree of freedom and the effect of SOC generally splits the fourfold degeneracy (counting both spin and orbit degree of freedom) at $k_z = \pi/c$. In this spinful case, S_Z also acts on the spin space, S_z: $(s_x, s_y, s_z) \rightarrow (-s_x, -s_y, s_z)$. The square of S_z then rotate the spins by 2π, contributing a minus sign for the spin-$\frac{1}{2}$ system. Therefore the square of $S = IS_z$ becomes $S^2 = -1$, and *S* now has eigenvalues $\pm i$, which again can be used to label the eigenstates of the Bloch Hamiltonian, $S|\psi^{\pm}(\boldsymbol{k})\rangle = \pm i|\psi^{\pm}(\boldsymbol{k})\rangle$. Unlike the spinless case, the action of $C = IT$ on the eigenstate $|\psi^{\pm}(\boldsymbol{k})\rangle$ only switches it to a partner state of the same *S*-label, even though the anticommutation relation of *C* and *S* is retained. This point is easily checked as

$$SC\left|\psi^{\pm}(\boldsymbol{k})\right\rangle = e^{-ik_z c}CS\left|\psi^{\pm}(\boldsymbol{k})\right\rangle = -C(\pm i|\psi^{\pm}(\boldsymbol{k})\rangle) = \pm iC|\psi^{\pm}(\boldsymbol{k})\rangle. \qquad \text{(A5)}$$

Equation (A4) is used in Eq. (A5), and the last equality in Eq. (A5) is obtained based on the fact that the time-reversal operator $T = is_y K$ contained in *C* conjugates i to $-i$.

As *C* only relates the eigenstate to its partner with the same *S* label, we only obtain two Kramer pairs that cannot be related by symmetry *S* and *C* only. To explain the fourfold degenerate nodal lines of *2H-TaSe*$_2$, we need other symmetries. We find it is the mirror symmetry M_x: $(x, y, z) \rightarrow (-x, y, z)$ that provides the needed protection for these nodal lines. The implication is that the high symmetry path $k_x = 0$ at $k_z = \pi/c$ is just the intersection line of the invariant plane $k_x = 0$ of M_x and the invariant plane $k_z = \pi/c$ of *S*. On this invariant line, action of M_x will transform the eigenstate $|\psi^{\pm}(\boldsymbol{k})\rangle$ to a partner of an opposite *S* label, which then relates the two Kramer pairs and ensures a fourfold degenerate nodal line. Before clarifying this point, we first prove that M_x anticommutes with *S*. It is

easily checked that, in the real space, action of SM_x and M_xS on the coordinate leads to the same result. The anticommutation relation of M_x and S comes from their action on the spin space. In spin space, S reflects s_x and s_y but keeps s_z invariant, from which one can express its action by $e^{i\pi/2\hat{s}_z} = i\hat{s}_z$. Similarly, the action of M_z on the spin is expressed by $e^{i\pi/2\hat{s}_x} = i\hat{s}_x$. It is the action of M_x and S on the spin space that ensures the anticommutation relation, $\{S, M_x\} = 0$. By applying M_x on the eigenstate $|\psi^{\pm}(\boldsymbol{k})\rangle$, one then finds

$$SM_x|\psi^{\pm}(\boldsymbol{k})\rangle = -M_xS|\psi^{\pm}(\boldsymbol{k})\rangle = -M_x(\pm i|\psi^{\pm}(\boldsymbol{k})\rangle) = \mp iM_x|\psi^{\pm}(\boldsymbol{k})\rangle. \quad \text{(A6)}$$

Equations (A5) and (A6) finally finish the proof that at $k_z = 0$ on the $k_z = \pi/c$ plane ($A - L$ direction) there must be a four-fold degenerate nodal line guaranteed by symmetries $S = IS_z$, $C = IT$, and M_x. The nodal lines at $k_x = \pm\sqrt{3}k_y$ on $k_z = \pi/c$ then result from the C_{3z} rotation.

The symmetry argument in this section is adapted from Ref. [1].

Appendix B

Fermi Surface Folding in *2H-TaSe*$_2$

The main idea of Fermi surface (FS) folding [2-5] is to reconstruct the band structure under a new symmetry via shifting the original normal phase dispersion by some certain nesting vectors. In this section, we use 3×3 CDW ordering (which is the case for *2H-TaSe*$_2$) as an example. As the unit cell in real space becomes nine times the size of the one in the normal phase, the new Brillouin zone (mini-BZ) thus shrinks to one-ninth of normal phase counterpart. Thus, electronic band structure in momentum space should follow this new translational symmetry.

Fig. B1 illustrates details of the folding approach. First-order nesting vector, also labelled as $\boldsymbol{q}_{CDW}$, is defined by the new reciprocal vector $\boldsymbol{q_1} = \frac{2}{3}\Gamma M$ as marked by the red arrow in Fig. B1(b) connecting nearest neighbouring mini-BZ centres γ. Similarly, the second-order nesting vector, $\boldsymbol{q_2} = \Gamma K$, is defined by an addition of two first-order vectors with 60° rotation as marked by the green arrow in Fig. B1(b) connecting second nearest neighbouring γ. Under the CDW perturbation superpotential, replicas (FBs) of the main bands (MBs) are formed. First-order FBs are reconstructed by shifting the MBs by $\boldsymbol{q_1}$ [see Figs. B1a(i-iii)] while second-order by $\boldsymbol{q_2}$ [see Figs. B1a(iv-vi)]. First- and second-order FBs and MBs constitute the whole pictures of band structure in CDW phase [see Fig. B1a(vii)].

To avoid misunderstanding, two points need attention for FS folding model described above. First, this approach should be regarded as an Umklapp bands formation under a virtual displacement (infinitesimal distortion) of atoms thus hybridizations and interactions among bands are not included. Second, spectral weight distribution is not discussed here.

Since CDW superpotential is rather weak compared to the original lattice potential, MBs still enjoy the major spectral intensity whereas the FBs are very faint. In this work, we only apply FS folding as a first-order estimation for experimental band structure in CDW phase and an indicator for certain CDW ordering.

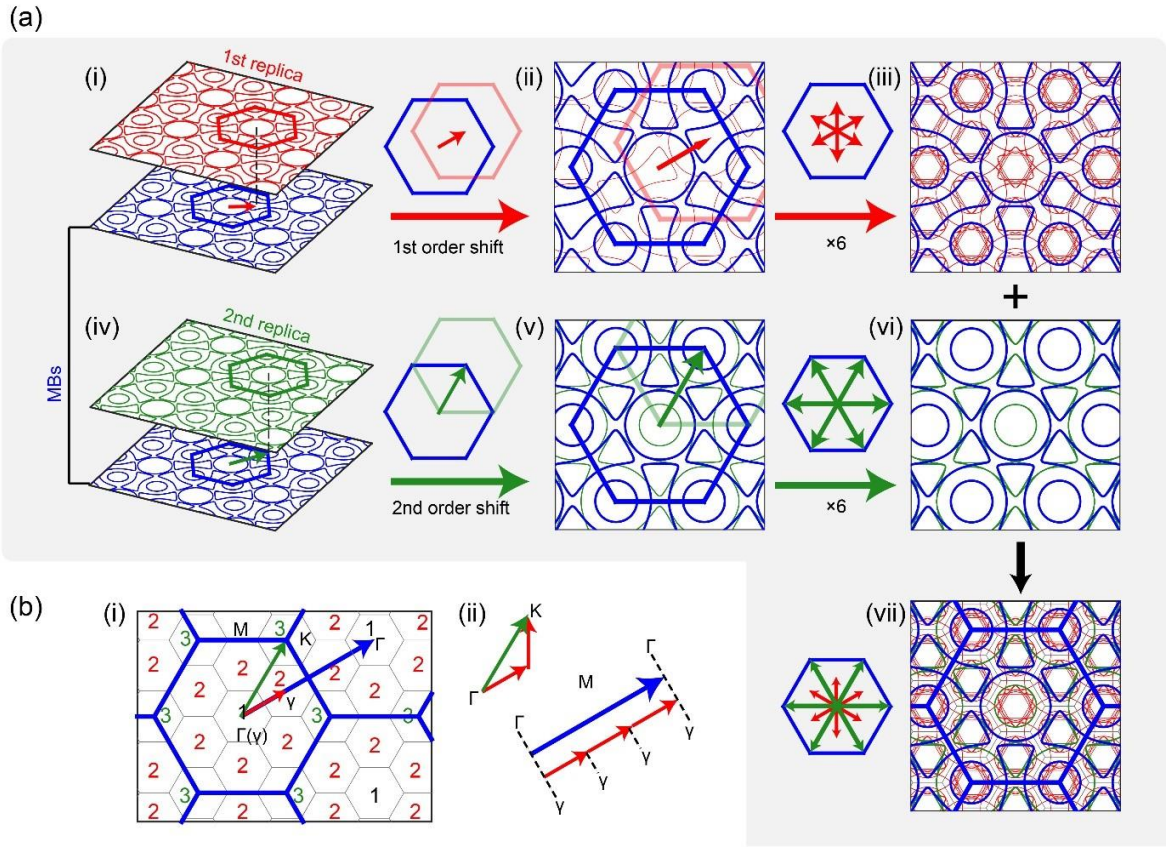


Fig. B1 3×3 Fermi surface (FS) folding. (a) FS folding flow diagram, 1st order folded bands (FBs) are generated by shifting the MBs by 1st nesting vectors $\boldsymbol{q_1} = \frac{2}{3}\Gamma M$ marked by the red arrows [this also applies to (b)]; (iv-vi) 2nd order FBs are generated by shifting the MBs by 2nd nesting vectors $\boldsymbol{q_2} = \boldsymbol{q_1} + \boldsymbol{q_1'} = \Gamma K$ marked by the green arrows [this also applies to (b)]; (vii) The combination of 1st and 2nd FBs. (b) Relationship between mini-BZ and nesting vectors. Inequivalent mini-BZ *1*, *2* and *3* under the influence of MBs are marked (see main text section 3.3.2).

The comparison between experimental and TB model based on FS folding is shown in Fig. B2. From ARPES FS contours, one can see that, in the CDW phase, folded features near E_F such as the triangular pockets are formed. The validity of the FS folding model is addressed as all experimentally observed FBs have their counterparts in the TB model, although some predicted FBs are invisible in the ARPES spectrum due to the matrix element effect. Because of the strong broadening effect at high binding energy, folded features are constrained to an energy window of about 200 meV below E_F. We also notice that CDW gaps are created where FBs meet MBs. This observation favours the MB-FB hybridization interpretation. However, as mentioned above, CDW gaps are not included in this model since it is based on an infinitesimal lattice distortion.

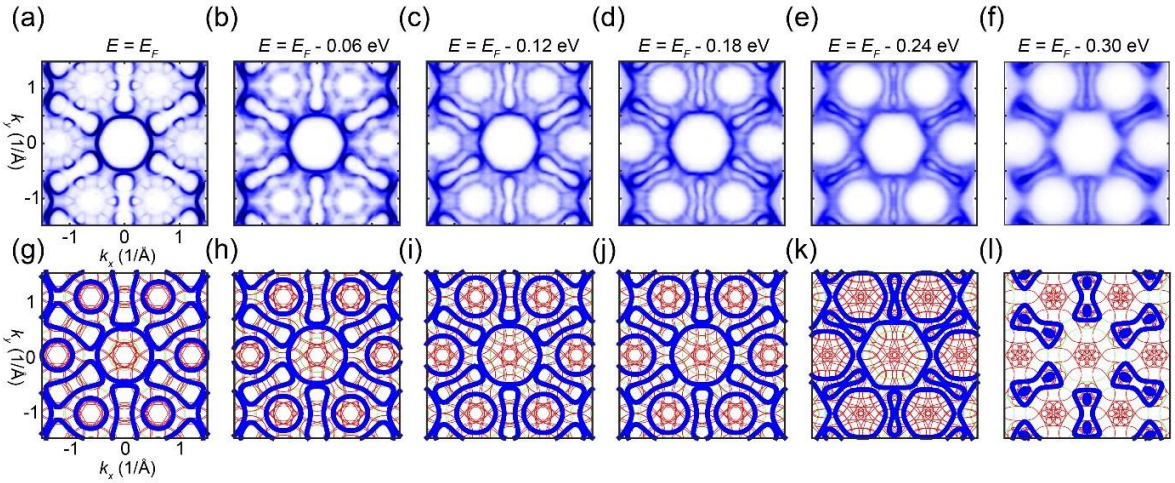


Fig. B2 Comparison between experimental FS contours (a)-(f) **and tight-binding model based on FS folding** (g)-(l) **at different binding energies from E_F to $E_F - 0.3$ eV.** In the lower row, the MBs, 1st and 2nd FBs are marked by thick blue, thin red and thin green lines, respectively.

Appendix C

k_z-effect in *2H-TaSe*$_2$

As shown in Fig. C(a), in an energy window of 150 meV below E_F, the band structure is very two-dimensional with a very weak k_z-dependence, although one can still identify the periodic band features along k_z direction. Therefore, it is quite safe to say that *2H-TaSe*$_2$ is a quasi-2D system at E_F.

Figs. C(b) and (c) compare two ARPES maps measured under 80 eV and 50 eV photon energy in CDW phase. The Fermi energy contours are very similar except for different spectral weight distribution. Based on the weak k_z-dependence of electronic structure near E_F and independent Fermi surface topology of the incident photon energy, we can rule out the possibility of the three-dimensionality for the additional fine structure near $\bar{\Gamma}$ under 50 eV photon energy. Thus, we attribute the enhancement of CDW band spectral weight to matrix element effect [also see Fig. 3.6 and Fig. 3.7 in the main text].

Although we have demonstrated that it is reasonable to treat the electronic structure near E_F as a 2D system, the small mismatch of band bottom at $\bar{\Gamma}$ between the experiment and the calculation as shown in Figs. 3.7(c) and (d) in the main text is probably due to the k_z effect of band structure in high binding energy. Based on its clear 2D nature, and for a better readability and consistency of the thesis, we develop our TB calculation on a 2D model which simulates the experimental result measured at 80 eV photon energy [see details in section 3.2.1 in the main text]. In Figs. C(d) and (e), we show that there is a clear undulation of the binding energy of the band bottom at $\bar{M}$. Therefore, we deduce that the mismatch between experiment and calculation in Figs. 3.7(c) and (d) has the same origin as the

electronic structure measured at 50 eV and 80 eV photon energy at different k_z. The k_z-dependent electronic band structure is qualitatively consistent with previous theoretical study [3].

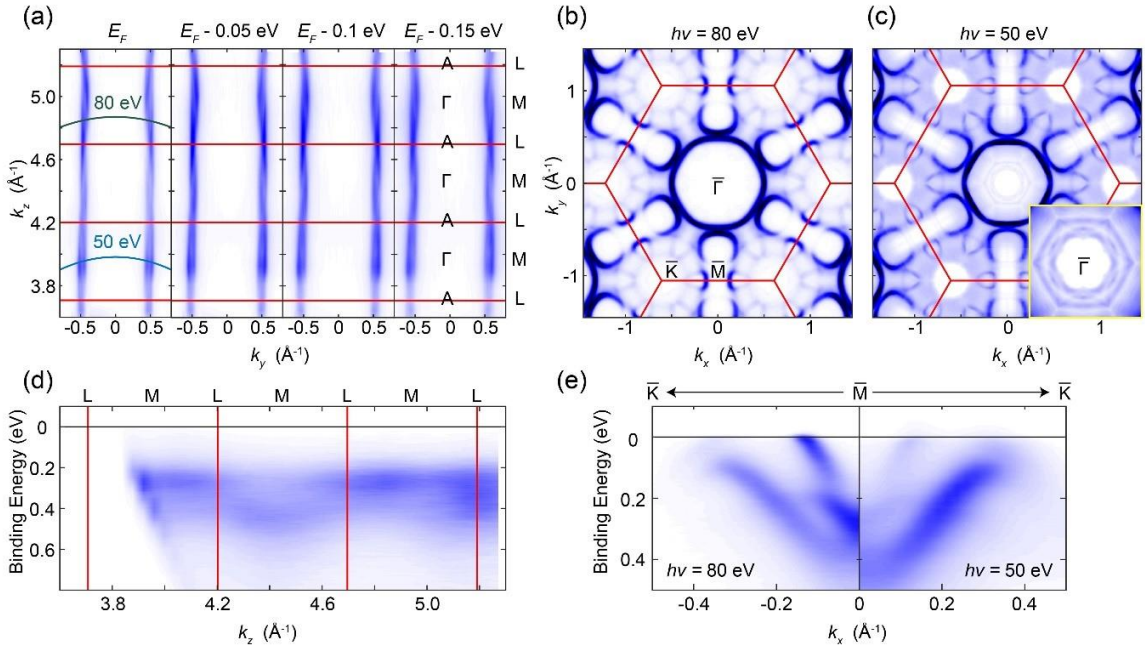


Fig. C k_z-dependent electronic structure. (a) ARPES energy contours in $k_y - k_z$ plane in the normal phase. (b) ARPES energy contour at E_F measured at $h\nu = 80$ eV in CDW phase. (c) ARPES energy contour at E_F at $h\nu = 50$ eV in CDW phase. The inset shows the zoomed-in plot around $\bar{\Gamma}$. (d) k_z-dependent ARPES band dispersion along $M - L$ direction. (e) Comparison of ARPES band dispersion along $\bar{K} - \bar{M} - \bar{K}$ measured at $h\nu = 80$ eV (left) and $h\nu = 50$ eV (right).

Appendix D

Validity of Maximum Intensity Projection

Fig. D shows the validity of maximum intensity projection (MIP) method by presenting consistent gap size measured by the conventional method and MIP approach in the momentum area of “dog-bone” electron-pocket as an example. Figs. D(b)-(d) show ARPES measurements cutting cross the CDW gaps. By comparison with normal phase data, the band forming the “dog-bone” electron pocket is gapped into segments in CDW phase. In contrast, Figs. D(f) and (g) show ARPES measurements cutting along the CDW gaps. The MIP approach not only helps precisely locate the momentum position of the CDW gaps, but also gives consistent gap values with ones measured by the conventional method by visualizing both upper and lower bands at the CDW gaps.

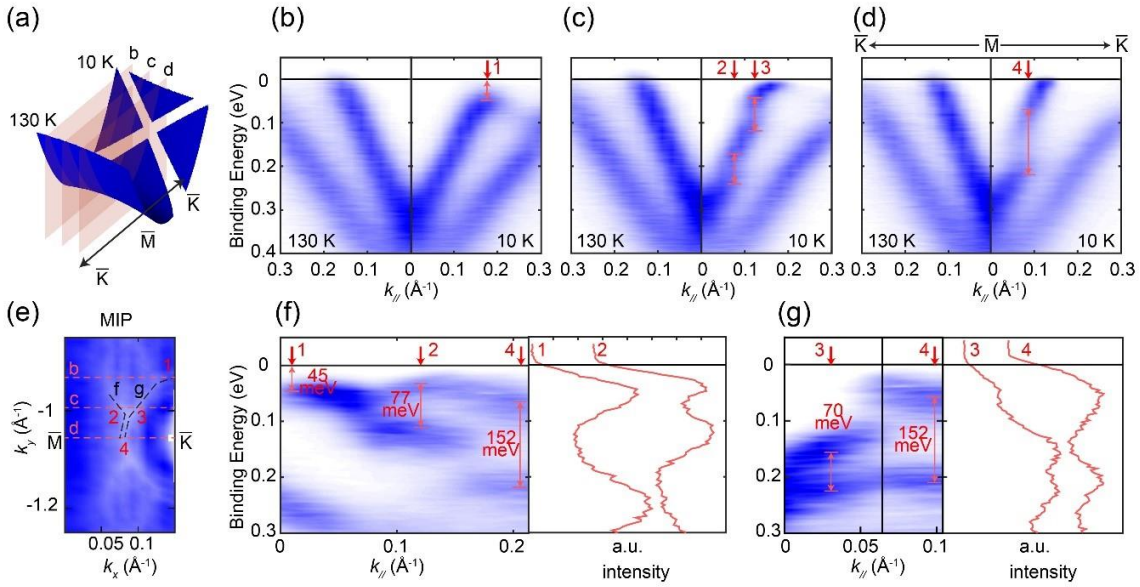


Fig. D. Consistent gap size measured by conventional method and MIP. (a) 3D TB model of "dog-bone" electron-pocket. The magenta slices along $\bar{K} - \bar{M} - \bar{K}$ indicates the momentum position of three ARPES cuts. (b)-(d) Three ARPES cuts measured in normal (left) and CDW (right) phase. Momentum cutting directions are indicated in (a). The CDW gaps are marked by red double-headed arrows. (e) MIP of ARPES data in the momentum area of "dog-bone" electron-pocket. Magenta and black dashed lines indicate the momentum direction for ARPES cuts (b)-(d) and (f), (g), respectively. (f), (g) ARPES cuts along momentum direction indicated in (e). Energy distribution curve (EDC) plots at momenta of interest (1)-(f) are presented in the right panel.

Appendix E

Orbital Resolved Bulk Band Structure of *1T-PtSe*$_2$

Fig. E(b) illustrates the atomic orbital components of the bulk states of *1T-PtSe*$_2$. One can observe that the VB near E_F mainly comes from *Se* ***p*** orbitals. For example, the major orbital contribution for the top four VBs at Γ are *Se* $\boldsymbol{p_z}$, *Se* $\boldsymbol{p_{x,y}}$, *Se* $\boldsymbol{p_{x,y}}$ and *Pt* ***d***, respectively.

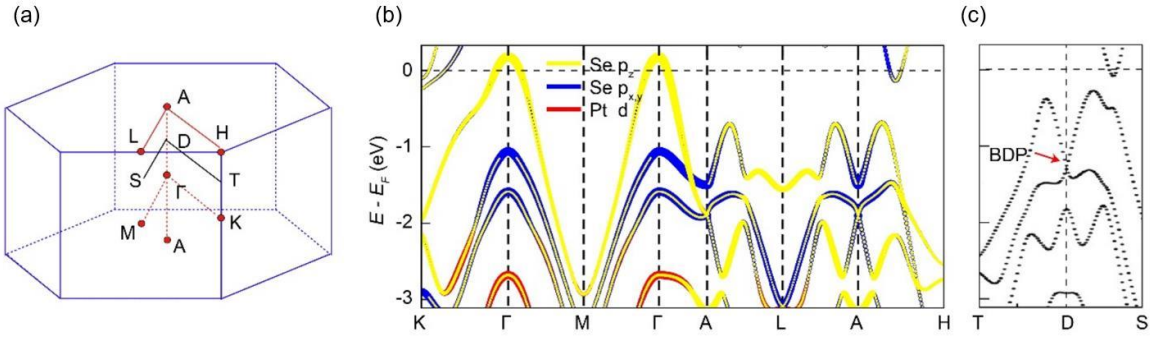


Fig. E *Ab initio* calculation of bulk band structure of *1T-PtSe*$_2$. (a) 3D illustration of the Brillouin zone of *1T-PtSe*$_2$. High symmetry points are indicated. $S - D - T$ plane define the equal k_z plane for the bulk Dirac point as shown in (c). (b) Atomic orbital resolved bulk band structure of *1T-PtSe*$_2$. (c) Calculation along $T - D - S$ direction showing the bulk Dirac point.

References of Appendix

[1] Q.F. Liang, J. Zhou, R. Yu, Z. Wang, H.M. Weng, Node-surface and node-line fermions from nonsymmorphic lattice symmetries, *Physical Review B*, **93** (2016) 085427.

[2] K. Rossnagel, E. Rotenberg, H. Koh, N. Smith, L. Kipp, Fermi surface, charge-density-wave gap, and kinks in $2H{-}TaSe_2$, *Physical Review B*, **72** (2005) 121103.

[3] K. Rossnagel, N. Smith, Spin-orbit splitting, Fermi surface topology, and charge-density-wave gapping in $2H{-}TaSe_2$, *Physical Review B*, **76** (2007) 073102.

[4] S. Borisenko, A. Kordyuk, A. Yaresko, V. Zabolotnyy, D. Inosov, R. Schuster, B. Büchner, R. Weber, R. Follath, L. Patthey, Pseudogap and charge density waves in two dimensions, *Physical Review Letters*, **100** (2008) 196402.

[5] M. Johannes, I. Mazin, Fermi surface nesting and the origin of charge density waves in metals, *Physical Review B*, **77** (2008) 165135.